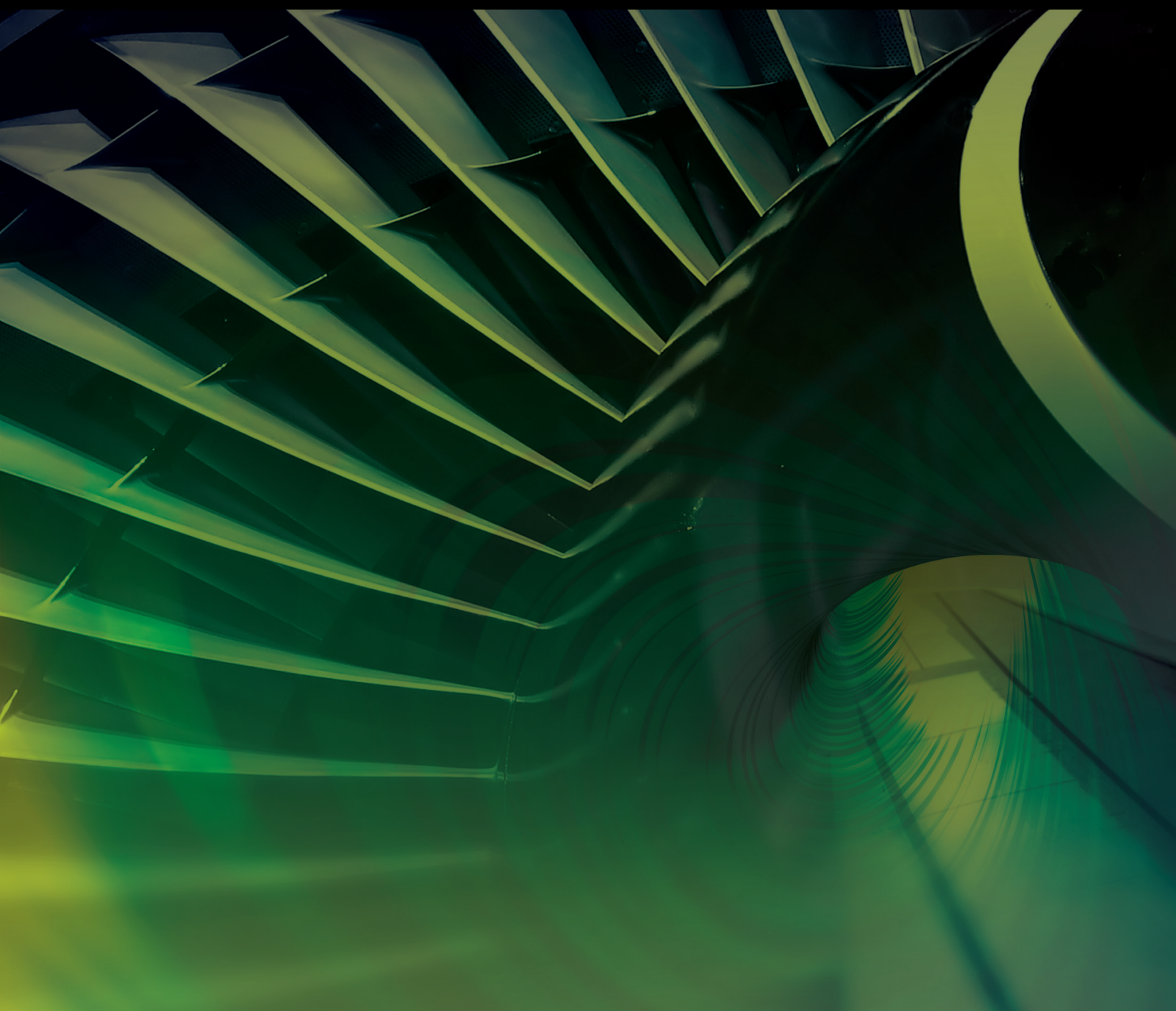# Smart and Adaptive Structures for Aeronautical Applications

Lead Guest Editor: Rosario Pecora
Guest Editors: Antonio Concilio and Ignazio Dimino

Smart and Adaptive Structures for Aeronautical Applications

Smart and Adaptive Structures for Aeronautical Applications

Lead Guest Editor: Rosario Pecora
Guest Editors: Antonio Concilio and Ignazio Dimino

Contents

Research Article

Advanced Design of a Full-Scale Active Morphing Droop Nose

Alessandro De Gaspari ⓘ, **Vittorio Cavalieri** ⓘ, **and Sergio Ricci** ⓘ

Department of Aerospace Science and Technology, Politecnico di Milano, 20156 Milano, Italy

Correspondence should be addressed to Alessandro De Gaspari; alessandro.degaspari@polimi.it

This paper describes the design of a morphing droop nose conceived to increase the performance in high-lift conditions of a twin-prop regional aircraft, while ensuring the natural flow laminarity of the wing. Starting from the results obtained in a previous phase, mainly concerned with the performance augmentation, a detailed structural design is conducted. The main aim is the achievement of a feasible solution based on the use of conventional materials, such as aluminium alloy for the internal structure and glass-fibre for the skin. A finite element model of the complete device is generated for the three-dimensional shape quality evaluation and for the skin structural verification. Stress analyses on high-fidelity models of the single adaptive ribs are also performed. At the same time, various design aspects are evaluated, such as installation and inspection issues, actuation power, and weight considerations. All these requirements contribute to the definition of an advanced and complete solution for the device, up to the realization of a detailed CAD model. Final verification on the virtual prototype assesses the functionality of the device when attached to the wing-box. Moreover, the bird impact safety of the leading edge is demonstrated according to the certification rules.

1. Introduction

In the framework of Clean Sky 2 REG–IADP AIRGREEN 2 (AG2) project, many morphing concepts are analysed to be applied to a next-generation twin-prop regional transport aircraft. One of the developed devices is a morphing Droop Nose whose aim is to achieve the requested high-lift performance during take-off and landing and, at the same time, to preserve the optimal Natural Laminar Flow (NLF) wing shape in cruise.

The adoption of the morphing leading-edge device can ensure the desired high-lift performance, along with enhanced efficiency with respect to the baseline configuration, also considering that usually regional aircraft do not employ conventional slats.

From the aerodynamic perspective, the design objective is the definition of the optimal drop law and shape for the achievement of the required performance. The major challenge is the design of a structure able to guarantee the expected target shape, while satisfying the certification rules. Indeed, the design of morphing structures is a tough

challenge due to the contemporary presence of conflicting requirements [1], such as a sufficient flexibility required to accomplish the shape change coupled with the typical load-bearing capability. The approach here proposed for the design of this kind of morphing device is based on an internal compliant structure connected to a flexible composite material skin.

In the last ten years, PoliMi has been involved in several projects, through which the authors have acquired an important background in the design techniques for morphing structures application [2–4]. The developed design procedure is mainly based on a multilevel multidisciplinary optimization loop [5]. At the first stage, an aerodynamic optimization with structural constraints is performed for the definition of the optimal target shape according to the requirements. Later, a multiobjective optimization analysis is used to find an internal structure based on the distributed compliance concept [6]; the stiffness is efficiently distributed so that, once actuated, the deformation of the structure produces the target aerodynamic shape. After that, additional optimization tools are used, and further considerations are

included in the design process to increase the level of detail of the final solution.

The results of the design process for the considered droop nose device were preliminarily presented in [7]. In this paper, the virtual prototype is finalized, including several technological aspects, with the aim of increasing the Technology Readiness Level (TRL) of the proposed morphing device. From the structural perspective, a special effort is devoted to the selection of the skin material in order to achieve a smooth morphing surface. Regarding the internal structure, it must be found a feasible solution able to withstand the external loads without significant deformation and within the strength limits of the adopted material. The last point is especially critical since the large requested deployment of the device causes high stresses in the structure, as already seen in previous works; hence, particular attention must be given to the satisfaction of the stress limits. Actuation time and power must be analysed to check if they agree with the initial requirements. In addition, the selected actuators must be compatible with the available space. Weight evaluation is also essential, in order to estimate if overall the complete device made of structure, actuation, and connections can guarantee the expected augmented performances that have been computed by the initial aerodynamic analyses. The proposed device must satisfy some other requirements related to its assembly on the aircraft and the possibility to carry out scheduled inspection easily. Moreover, due to the flexibility of the leading-edge skin, the structure itself is not able to pass bird impact test; hence, an appropriate support structure is required; also in this case, the conceived solution must fit in the available space. Final verification includes the analysis of the mutual interaction between the wing-box deformation and the droop nose deployment.

This paper is organized as follows. Section 2 describes the requirements for the droop nose device and its layout, the adopted design procedure and the resulting configuration. Section 3 addresses the refined structural design of the device, while Section 4 reports the stress verification. Section 5 illustrates various features of the selected technology solution, such as the type of actuation, its installation and the required power, but also weight considerations, assembly and inspection issues. Then, Section 6 discusses the verification in terms of droop nose/wing-box interaction and bird impact protection. Finally, Section 7 draws the conclusions of the entire work.

2. Morphing Droop Nose

The considered leading-edge morphing device is designed to be installed on 90 passengers, twin prop Regional Aircraft, that is one of the reference aircraft for the Regional-IADP platform, in the framework of the Clean Sky 2 AIRGREEN project. Table 1 reports the main characteristics of the reference aircraft.

According to the wing layout, the morphing Leading Edge is composed by an inboard region, which extends from the wing root to the nacelle, and an outboard region, which continues after the nacelle up to the wing tip. The chordwise extension of the device is defined by considering the front spar position at the 16% of the local chord.

TABLE 1: Reference aircraft characteristics.

Maximum take-off weight	32560 kg
Maximum zero fuel weight	31200 kg
Cruise Mach at 20000 ft	0.52
Landing Mach at sea level	0.197
Mean aerodynamic chord	2.565 m
Reference wing area	32.384 m^2
Reference wing span	14.827 m

2.1. Initial Design Requirements. The main objective of the morphing droop nose is to delay the wing stall in take-off and landing conditions, enhancing the maximum lift coefficient. At the same time, the skin surface must remain smooth in order to preserve flow laminarity, moreover steps and gaps are not allowed. Regarding the maximum lift coefficient, the requested increase is of 2.4% in take-off condition and of 1.7% in landing condition with respect to the reference configuration. These values must be obtained by the combined use of the addressed leading-edge device and the trailing-edge morphing flap developed at University of Naples [8, 9].

Regarding the actuation system, electro-mechanic actuation (EMA) must be installed to execute the deployment of the device. Moreover, the actuation time from the undeformed position to the maximum deflection must be less than 20 s. Both the structure design and the actuation selection should follow the requirement of minimum weight.

The two main components of the droop nose device are a continuous deformable skin connected to 20 equally spaced compliant ribs, which constitute the internal structure conceived to produce the shape change. The connection is realized through some stiffeners that extend along the entire span, which are needed to make the skin deformation uniform in the spanwise direction. Thanks to the distributed compliance concept, the internal structure can convert the displacement of one of its points, defined as input point, into the controlled displacement of the attachment points on the skin, defined as active output points. The rib input point is connected to the end of a kinematic chain, which is moved by the rotation of the drive shaft of the actuators. The actuator is then used to achieve the morphing configuration but also to keep the leading-edge fixed in the initial configuration. In both cases, the corresponding aerodynamic loads are applied to the external surface.

The complete wing of the regional aircraft equipped with the morphing droop nose is depicted in Figure 1.

2.2. Preliminary Design. The definition of the optimal external shape is performed according to an aero-structural optimization loop [10]. The objective function of the shape optimization process aims at maximizing the droop deflection along the wingspan and, at the same time, reducing the drag coefficient. The considered flight condition is the landing configuration at 10 deg. Three identified parametric sections are used for the introduction of the morphing shape changes. Regarding the constraints, a linear deflection law in spanwise direction for the outboard region is imposed. Moreover, there are two structural constraints: the first one
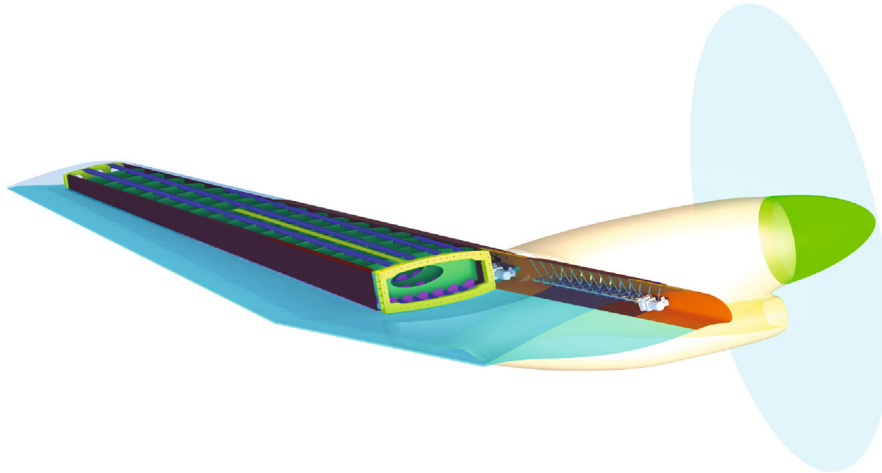
FIGURE 1: Twin prop regional aircraft equipped with the morphing droop nose.
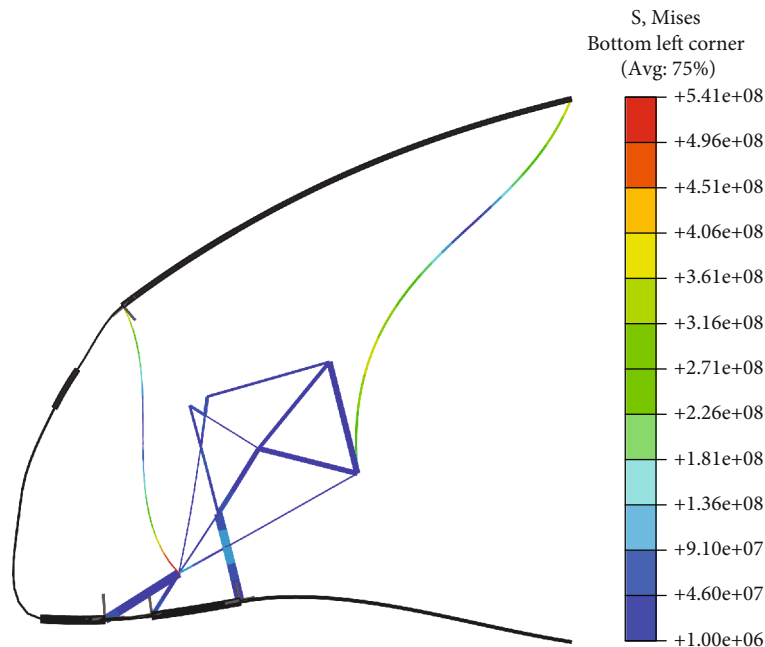
FIGURE 2: Topology solution for the internal structure.

is related to the skin strain, which is evaluated by geometric considerations based on the curvature change, the second one is related to the wing-box implicit constraint [10]. In particular, the allowable skin axial strain is zero, according to the constant cross-section length (CCL) concept [5], while normal strain due to bending must be limited below 1%, which corresponds to a skin maximum curvature change of 20 1/m.

The aerodynamic analyses are performed by the MSES solver, which is a fully coupled, implicit code, based on integral boundary layer (IBL) interaction [11]. The droop nose deflection is combined with the extension of a conventional trailing edge flap, which position is due to the combination of rotation and translation, and it is set to around 30 deg.

The morphing leading-edge shape obtained from shape optimization is characterized by a constant droop deflection $\delta LE = 16.2°$ for the inboard region, while the linear deflection law for the outboard region goes from the abovementioned value up to $\delta LE = 10.2°$ at the first section of the aileron, and then gradually vanishes. The target shape obtained for the inboard region is visible in Figure 1.

Detailed three-dimensional RANS computations for the 3D wing are performed using the Onera elsA software [12] in fully turbulent mode, assessing the enhanced aerodynamic efficiency and a significant delay of stall onset by using the morphing devices. Take-off and landing flight conditions have been analysed, and a comparison of the aircraft performances has been carried out between the configurations with and without the morphing droop nose. This device leads to a constant decrease in the drag coefficient on the entire range of lift coefficient. In take-off configuration, the effect of the droop nose on the lift curve shows a stall angle increase of 2.5°. In landing configuration, the use of the morphing droop
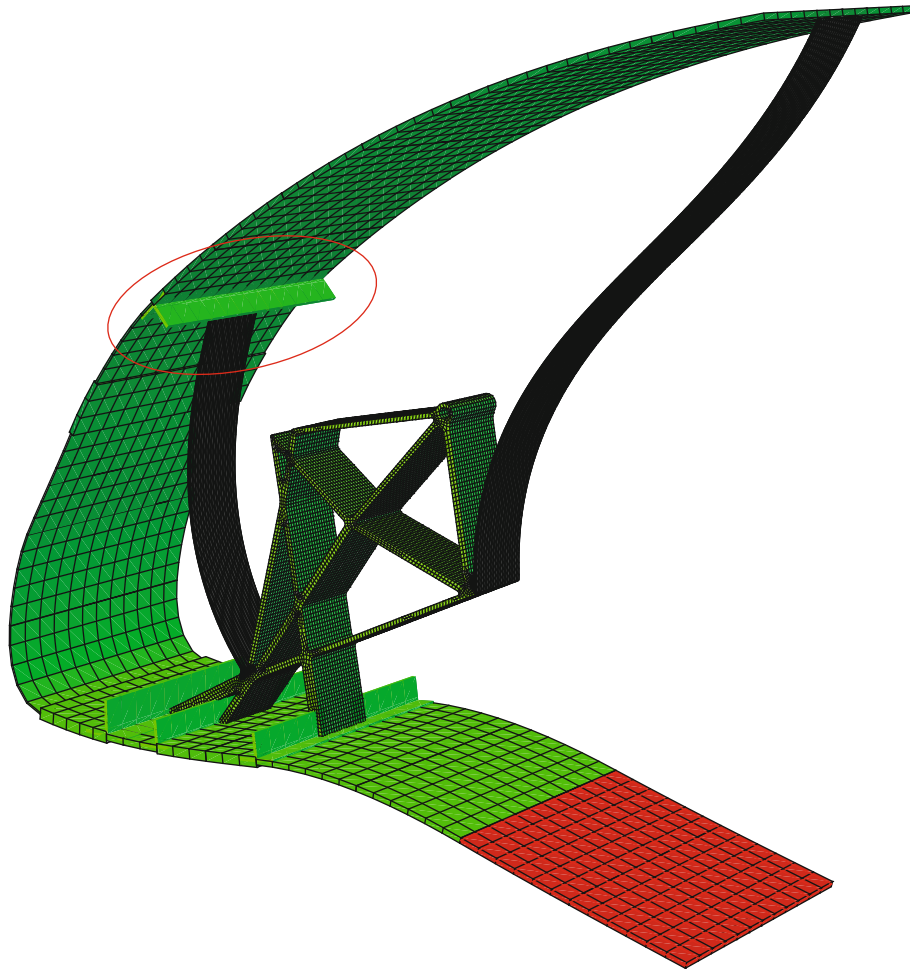
FIGURE 3: Finite element model of a wing section of the droop nose with the inspection panel and the new hinged connection to the top skin.
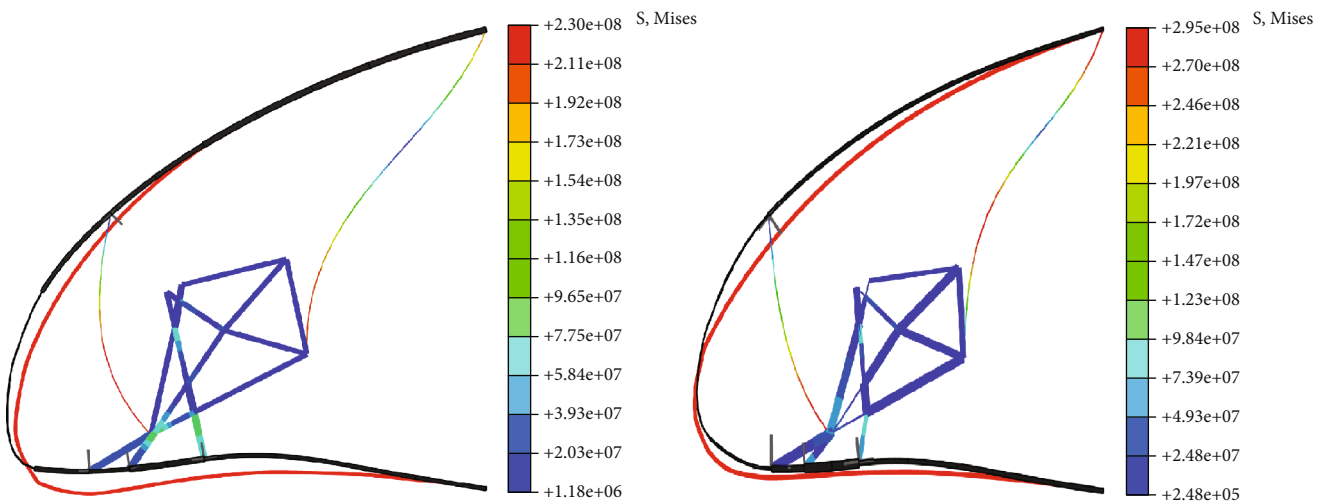
FIGURE 4: Inner rib (left) and outer rib (right) optimal solutions. Comparison between the optimal deformed shape and the target shape. Stress in the ribs.

nose increases the stall angle of about 5°. The droop nose is necessary for landing conditions to guarantee a maximum lift coefficient that satisfies the AG2-NLF aircraft performance [13].

After the definition of the optimal aerodynamic shape according to the requirements, a dedicated optimization process is adopted for the design of the optimal internal

TABLE 2: Aluminium alloy mechanical properties.

Parameter	Value
Young modulus	72000 MPa
Poisson's coefficient	0.33
Yield strength	470 MPa
Ultimate strength	540 MPa

TABLE 3: Glass-fibre reinforced polymer mechanical properties.

Parameter	Value
E_{11}	45700 MPa
E_{22}	13500 MPa
ν_{12}	0.27
G_{12}	5400 MPa
G_{13}	5400 MPa
G_{23}	2000 MPa
Longitudinal tensile strength	1999 MPa
Transverse tensile strength	62.0 MPa
Longitudinal compressive strength	-965 MPa
Transverse compressive strength	-155 MPa
In-plane shear strength	93.1 MPa

TABLE 4: Thickness distribution for the skin structural layer.

Region ID	Number of plies	Total thickness (mm)
1	14	2.8
2	26	5.2
3	16	3.2
4	6	1.2
5	2	0.4
6	2	0.4
7	6	1.2
8	4	0.8
9	12	2.4
10	12	2.4

FIGURE 5: Skin partition and region identifiers.

FIGURE 6: Complete finite element model of the droop nose.

compliant structure that enables, once actuated, to achieve the optimal target previously defined. This design stage is based on a multiobjective genetic algorithm coupled with a load-path representation and an in-house finite volume beam model solver [2, 5]. This multiobjective approach, incorporated into an elitist nondominated sorting genetic algorithm (NSGA–II) [14], is suitable to deal with the conflicting requirements of external shape change and load-carrying capability. Indeed, different objective functions are considered and simultaneously minimized by the algorithm, namely: (i) the least-square error between the achieved morphing shape and the target one; (ii) the strain energy in the conventional structural configuration; (iii) the stress in the compliant ribs of the morphing configuration. The analyses for the computation of the least-square error and the stress take into account the aerodynamic loads related to the morphing configuration (landing condition). The aerodynamic loads of the conventional configuration (cruise condition) are applied in the computation of the strain energy. The minimization of this function guarantees that the nose is as stiff as possible under loads; this is a structural requirement for every aerodynamic control surface.

At the end of the optimization process, the optimum solution is selected on the resulting Pareto front.

As already explained, the internal structure consists of 20 equally spaced ribs, but the described optimization works on a single rib, considering a two-dimensional model made of beam elements for the rib and the skin. The skin is clamped in correspondence of the front spar, and the actuation force is applied at the input point of the rib when the device is actuated, while this point is locked when the device is kept fixed. The result of the optimization for the root rib is the topology solution that represents the starting point of the whole struc-

tural design process [7]. Figure 2 shows the topology solution in the morphing configuration of the device.

This topology solution found during the preliminary design shows some critical points. First, the internal structure conceived to morph the shape of the skin is subject to very high stresses up to 541 MPa, which are not compatible with the strength of conventional aluminium alloys typically adopted in the aeronautical field. The appearance of such
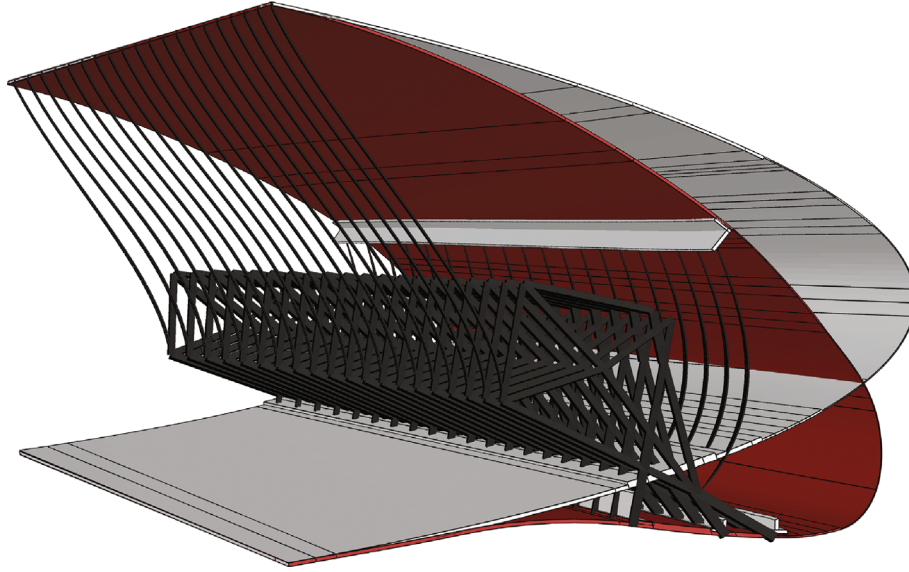
Figure 7: Three-dimensional deformed shape of the deployed droop nose.

high level of stress is due to the need to reach the requested deployment angle with the limited local chord extension of the leading-edge device. Another issue is related to the necessity to have an inspection panel for accessibility purpose, in order to lead the maintenance of the actuators. Both these aspects are treated in the subsequent detailed design of the internal structure.

Another important matter regards the spanwise extension of the droop nose. Indeed, since the outboard region is tapered, it needs proper attention to guarantee a uniform deflection behaviour along the span. The adopted approach starts from the obtained solution and makes use of the optimization analysis described in the next section.

3. Design of the Internal Structure

Regarding the problem of high stresses, the adopted strategy is to turn the fully compliant solution into a hybrid one, including the presence of a hinge in place of the upper clamped connection between the ribs and the skin. The second issue is solved by adding an inspection panel on the lower skin, adjacent to the front spar. Figure 3 shows the finite element model of a droop nose section, where both the upper hinged connection and the inspection panel are visible.

Both these two modifications are included in the subsequent design process, conducted by means of other optimization analyses. A refined process is contextually performed, aimed at obtaining an improved solution that satisfies all the additional requirements, while ensuring the agreement with the same target shape found in the first design phase.

The detailed structural design phase starts from the topology solution shown in Figure 2. Medium-fidelity models, as already depicted in Figure 3, are adopted, coupling beam elements for the rib and shell elements for the skin, thus overcoming the lower fidelity modelling of the previous stage. Nonlinear finite element analyses are performed with Abaqus software [15]. The structure under analysis is a lim-

ited spanwise portion of the skin connected to a single rib. The spanwise extension of the considered model is the length of the rib pitch, selected equal to 260 mm for the 3D device. The main modification with respect to the model used in the synthesis of the compliant structure is the inclusion of the connecting hinge between one of the rib paths and the skin. By using this alteration, it has been preliminary seen the possibility to put down the stress level.

At this stage, also, the presence of the inspection panel is considered. Its existence is modelled by clamping the opening region and excluding the panel from the structural analysis. After that, a suitable support structure has to be designed to guarantee the fixing of the panel in closed position; the executive details will be shown in the phase of CAD modelling.

A dedicated optimization analysis is conducted to ensure the satisfaction of the performance requirement represented by the optimal morphing shape change, along with the structural feasibility of the solution. For this purpose, it is selected a size optimization that acts modifying the thickness distribution of the skin and the in-plane width of the load paths which constitute the internal rib. The objective of the analysis is the minimization of the least-square error (LSE) between the achieved deformed shape and the target shape. A constraint on the maximum stress ensures the structural feasibility in the morphing configuration, while a constraint on the maximum strain energy in a critical condition for the conventional configuration guarantees the withstanding of the external loads without appreciable deformation. If the stress level in the structure is too high, there is the possibility to use the minimization of the stress as an objective function, while constraining the LSE below an upper threshold. Therefore, in the size optimization tool, it is possible to exchange objective and constraint functions. The sequential use of these complementary strategies enables further improvement in the refinement of the optimal solution, from both the shape quality and the structural feasibility perspectives.
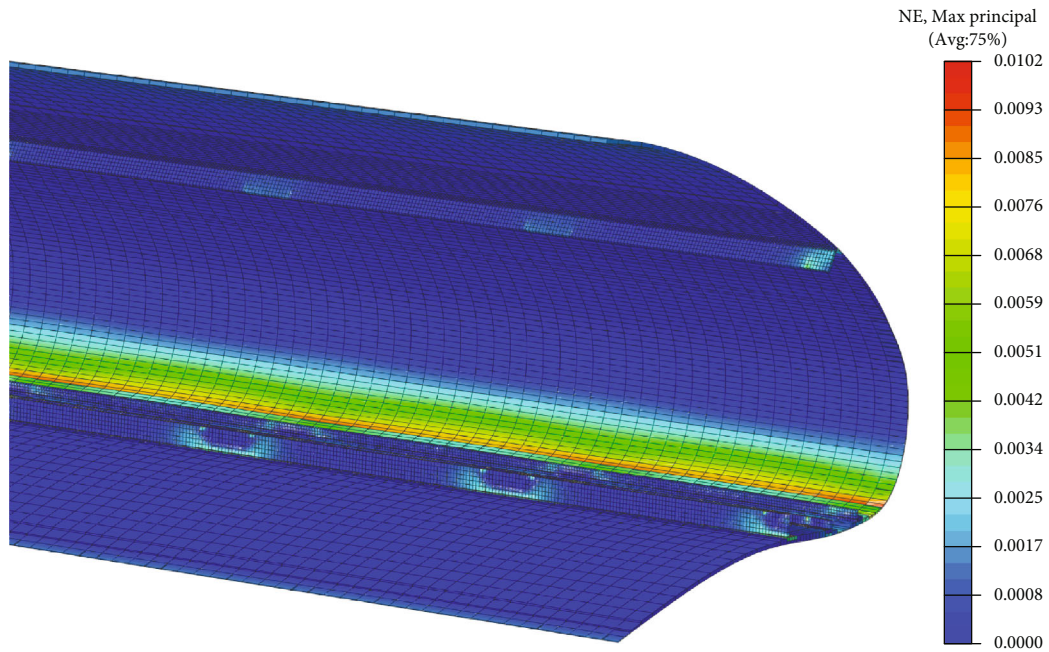
FIGURE 8: Maximum principal strain distribution in the skin.
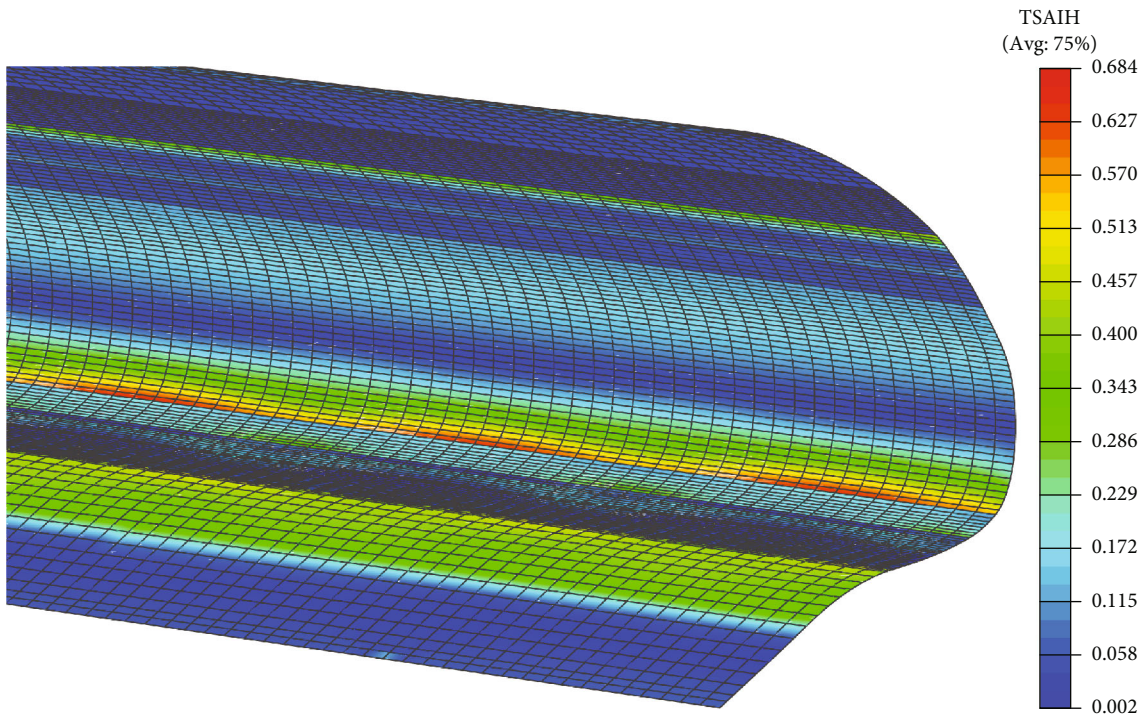
FIGURE 9: Strain verification for the skin: failure index distribution based on the Tsai-Hill theory.

3.1. Size Optimization Results. The size optimization procedure described before is initially applied to the compliant rib located at the wing root station. The same method is then applied to the compliant rib placed at the end of the outboard morphing region, starting from the previous solution. This approach allows to properly deal with the geometric tapering of the wing as well as the three-dimensional target shape based on a decreasing deflection law along the wingspan.

The results obtained in the two cases will be then interpolated to set the cross-sectional properties of all the intermediate ribs for the complete three-dimensional model.

Figure 4 compares the optimal deformed shape and the target shape for the two cases, also showing the stress inside the ribs. Regarding the inner rib at the wing root, the obtained solution is characterized by an LSE equal to 8.7 mm, while the LSE value for the outer rib solution is
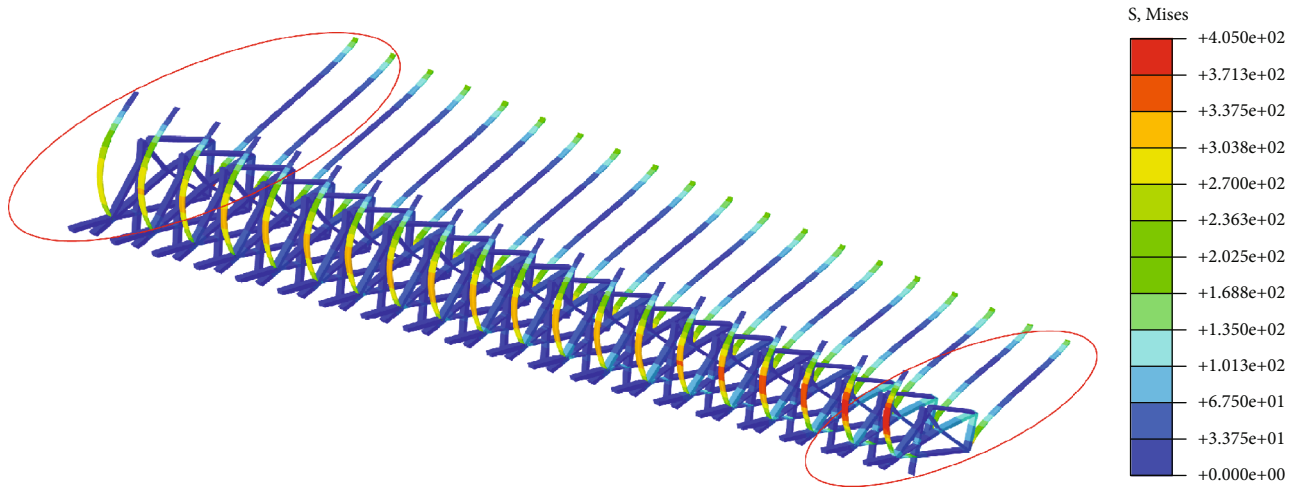
FIGURE 10: Stress distribution in the compliant ribs for the complete model.
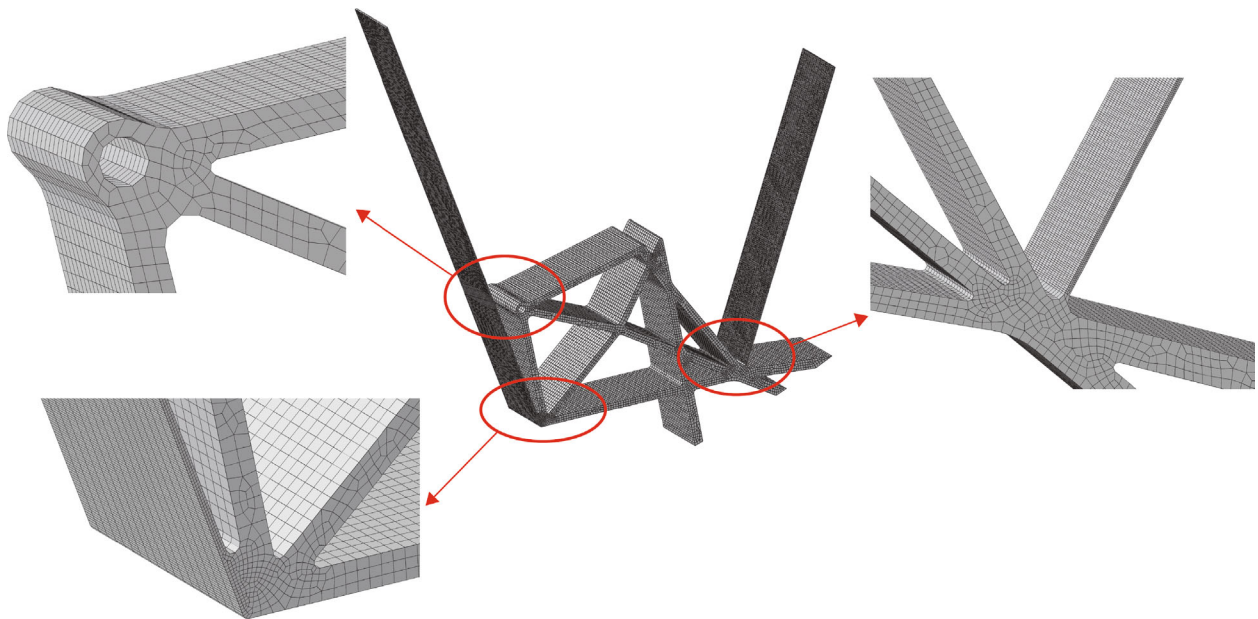
FIGURE 11: Detailed finite element model of a rib.

6.4 mm. The results in terms of stress reveal that stress reduction has been achieved, thanks to the adoption of the hinged connection and using the described optimization procedure, while considering at the same time the accessibility requirement related to the removable panel. On the other hand, from the shape quality perspective, the results show a worsening of the LSE values with respect to results obtained by the genetic algorithm, mainly corresponding to a lower deflection angle with respect to the desired target, but not due to a not smoothed shape.

Another work is focusing on an alternative solution for the internal structure, by the adoption of superelastic Nitinol, which is not a typical aeronautical material, but it can improve the achieved deformed shape thanks to the high recoverable strain the material is able to exhibit. This kind of material has already been applied to the design of morph-

ing devices in [16]. However, since one of the requirements of the addressed project is the use of conventional materials, in this work aluminium alloy material is selected, with the properties reported in Table 2, and the addition of a hinged connection allows to reduce maximum stress, though not enabling better shape results. However, since the theoretical aerodynamic performance increase is higher than the request, it is possible to accept a lower deployment of the device. Anyway, the achieved deformed shape must be evaluated on the full-span model of the device, as already done in [7].

3.2. Complete Finite Element Model. Once the optimal compliant inner and outer ribs are obtained by the size optimization analysis, the sizing of all the other ribs is derived by linear interpolation of the available extreme solutions. Such ribs are modelled again using beam elements. Regarding the

(a)

(b)
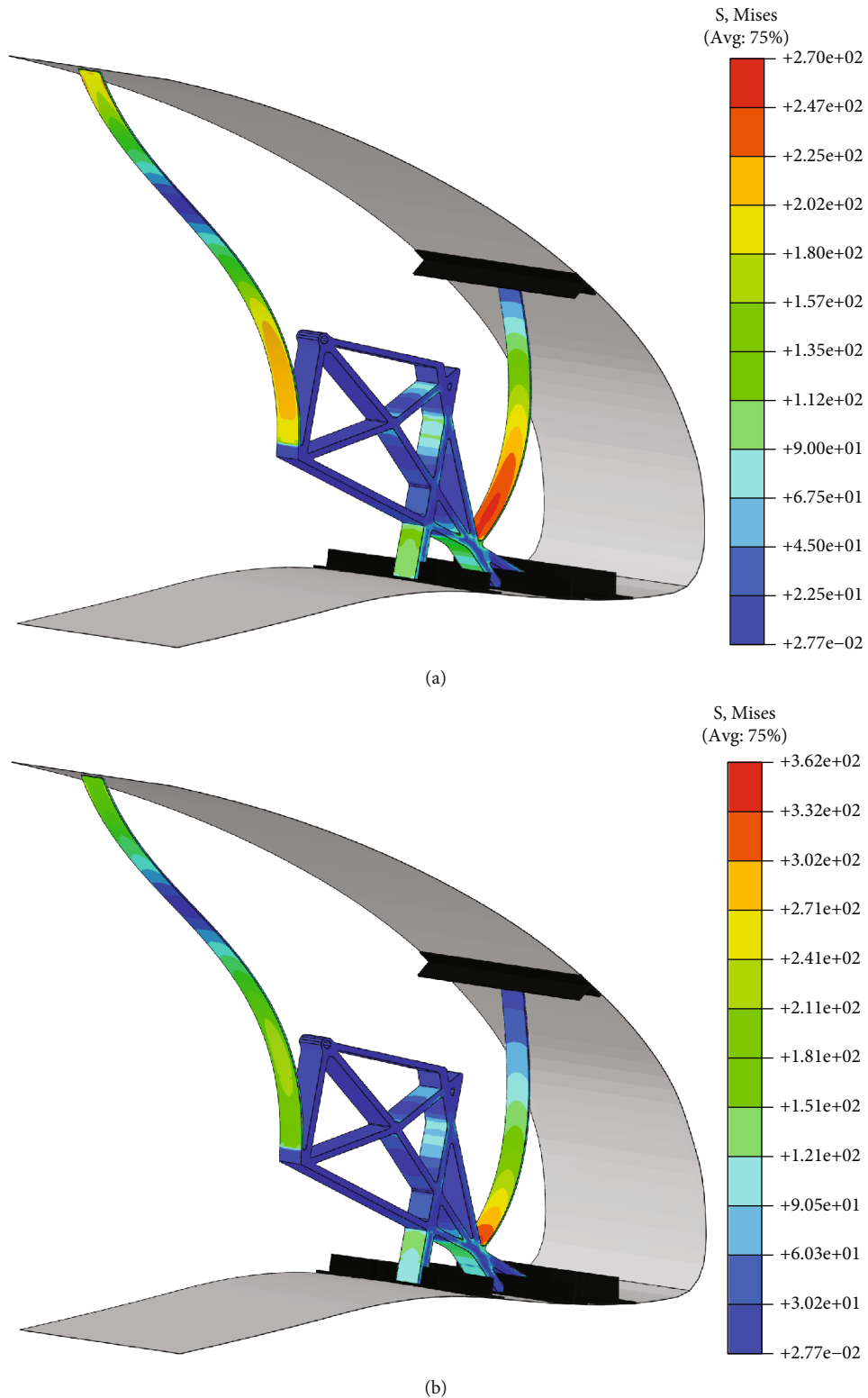
FIGURE 12: Stress in the root rib. (a) Limit loads. (b) Ultimate loads.

skin, it is composed by two layers: an antierosion layer made by titanium, whose thickness is equal to 0.10 mm, and a skin structural layer made by glass-fibre reinforced polymer, whose thickness distribution is determined within the described optimization analysis. Table 3 reports the material properties of the glass laminas. The thickness of each ply is 0.20 mm, and the stacking sequence of the laminate is $[0/90]_N$, where N is determined so that the total thickness of
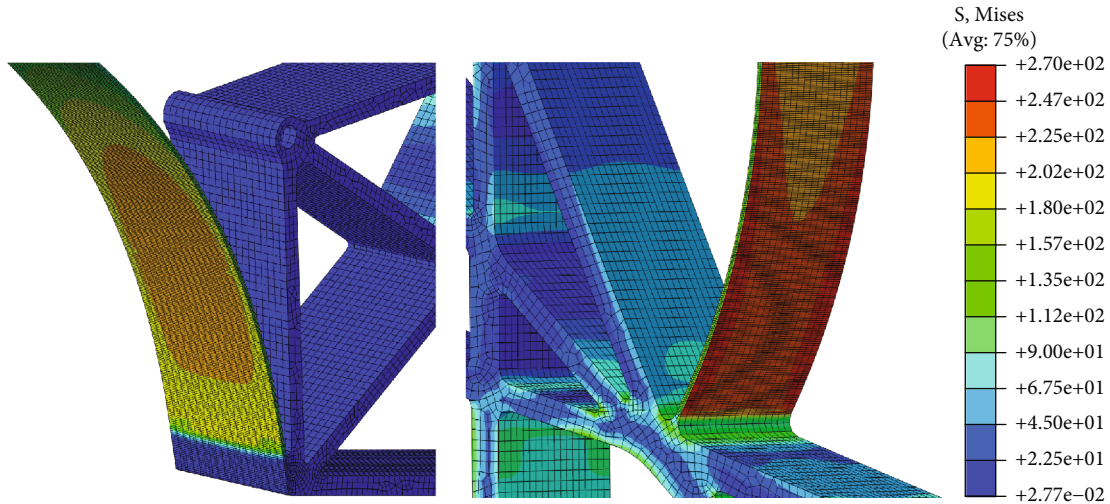
FIGURE 13: Root rib: detail of the most stressed regions under limit loads.

each skin region corresponds to the result of the optimization analysis, that is shown in Table 4, with reference to the region identifiers depicted in Figure 5.

The stiffeners, which are used for the connection between ribs and skin, are made of glass-fibre composite material and are supposed to be laminated together with the skin, as better explained later. Both the skin and the stiffeners are modelled using 4-node shell elements. In the complete FEM model realized in Abaqus, each rib is connected to the stringers, that are tied to the skin by means of kinematic coupling. The actuation system that introduces the morphing shape variation acting on the internal compliant structure is modelled with rigid links, and the kinematic chain is arranged through multiple point constraints (MPC). The complete model is represented in Figure 6. Overall, the model consists in 73822 elements: 67600 linear 4-nodes shells used for the skin (46306) and the stringers (21294) and 6222 linear 2-nodes beams used for the internal compliant ribs. As far as the skin is concerned, the element typical size in the high curvature region of the nose is about 5.00 mm, whereas, in the other regions, where the curvature variation is less significant, it is equal to 15.00 mm.

Static implicit nonlinear multistep analyses are performed in Abaqus, using a standard Newton solver and assuming a value of 10^{-3} as relative tolerance for convergence. The three-dimensional deformed shape achieved when the device is actuated is reported in Figure 7. It can be seen the undeformed skin region corresponding to the removable panel. The shape quality evaluation is globally successful, and the external surface remains smooth enough.

The strain distribution in the skin is shown in Figure 8. The maximum strain value of $10200\,\mu\varepsilon$ is compatible with the maximum curvature change of 1/20 m. From the same figure, it is possible to notice the strain concentration on the stringers, in correspondence with the attachment points of the ribs. Figure 9 reports the failure index distribution according to the Tsai-Hill criterion. The maximum index is 0.68; hence, the verification of the skin is successful.

Finally, the stress distribution inside the 20 compliant ribs is reported in Figure 10. The stress values are higher than the corresponding ones obtained at the end of size optimization. Further investigation is required, and it must be conducted by using more detailed finite element models. Anyway, the results from the complete model show increasing stress values from the root to the tip. For this reason, the next section focuses on the detailed verification of the ribs at the extremities.

4. Structural Verification

Starting from the optimal solutions obtained from size optimization, corresponding detailed finite element models of the extreme ribs are realized using three-dimensional solid elements. One of these models is shown in Figure 11, where the high refinement of the mesh is highlighted.

The nonlinear analyses performed on these models report high-stress concentrations with respect to the beam element models. By using a dedicated shape optimization, this issue can be overcome. Indeed, the adopted shape optimization acts on the contour surface of the internal structure redistributing the stress and decreasing the maximum peak. Final verification for the ribs, both under limit and ultimate loads, are conducted. The stress distribution in the root rib for the two cases is reported in Figure 12.

These analyses reveal acceptable safety margins, considering 470 MPa as yield strength and 540 MPa as ultimate strength. The detail of the most stressed regions in the limit loads case is shown in Figure 13.

Considering the stress values obtained by the high-fidelity analyses performed on the root rib, a safety margin SM = 0.74 for the limit loads and a safety margin SM = 0.49 for the ultimate loads are obtained.

The corresponding analyses for the rib at the tip are reported in Figure 14.

Also in this case, safety margins confirm structural feasibility. The detail of the most stressed regions in the limit loads case is shown in Figure 15.

(a)

(b)
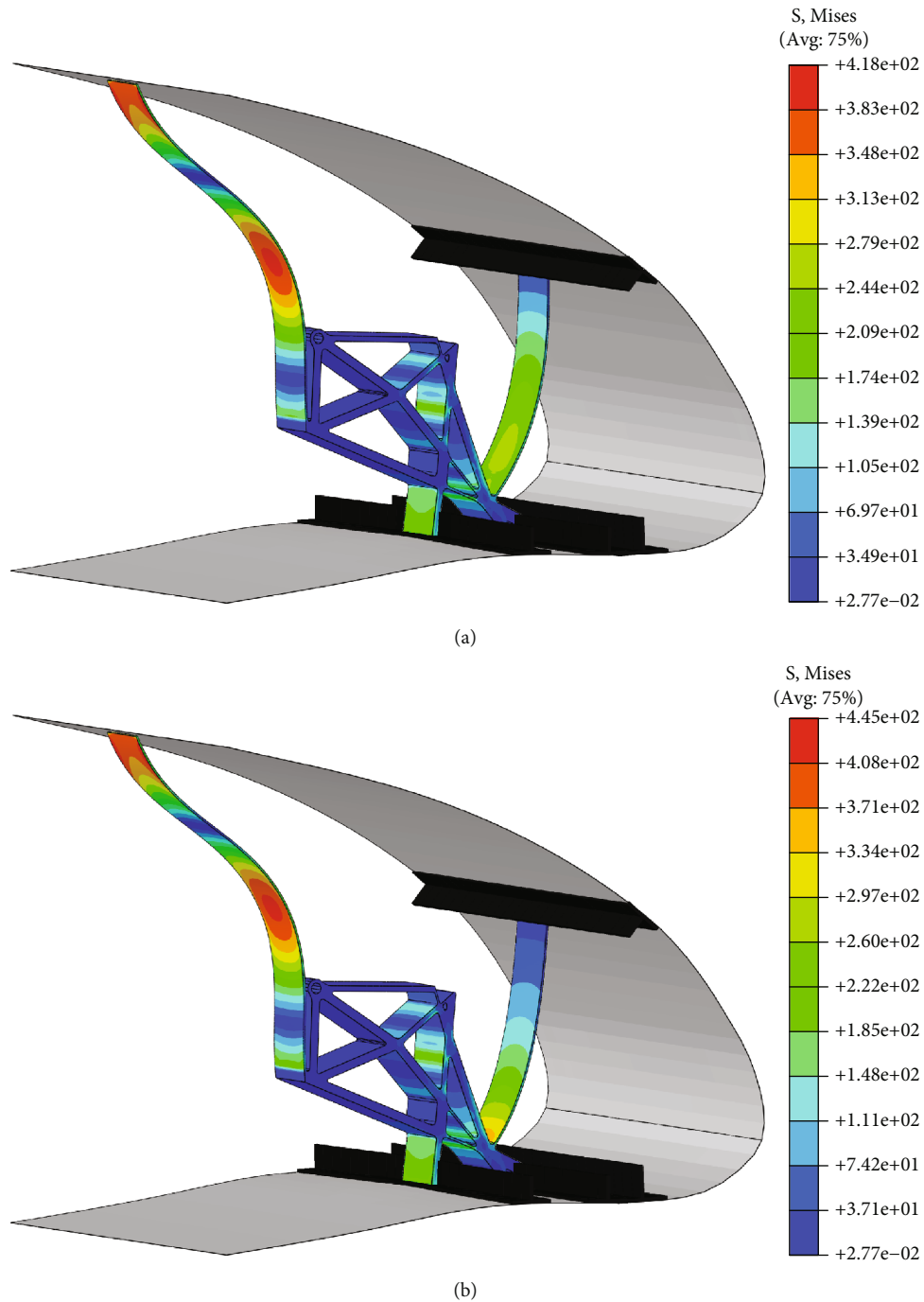
FIGURE 14: Stress in the tip rib. (a) Limit loads. (b) Ultimate loads.

Considering the stress values obtained by the high-fidelity analyses performed on the tip rib, a safety margin SM = 0.12 for the limit loads and a safety margin SM = 0.21 for the ultimate loads are obtained. Table 5 summarizes the safety margins in the different cases.

The described nonlinear analyses, conducted on solid element models, are more reliable than those on the corresponding beam element models. Therefore, the presented results demonstrate the structural feasibility of the proposed solution.

5. Technology Solution

Starting from the obtained solutions, corresponding CAD models for the ribs are realized. The distance from two consecutive ribs, namely the rib pitch, is equal to 260 mm. The geometry of each rib is determined by its spanwise position and the 3D shape of the wing. Regarding the in-plane thickness, the values obtained from size optimization are linearly interpolated along the span. Starting from the aerodynamic shape a 3D CAD model of the skin is also realized. The
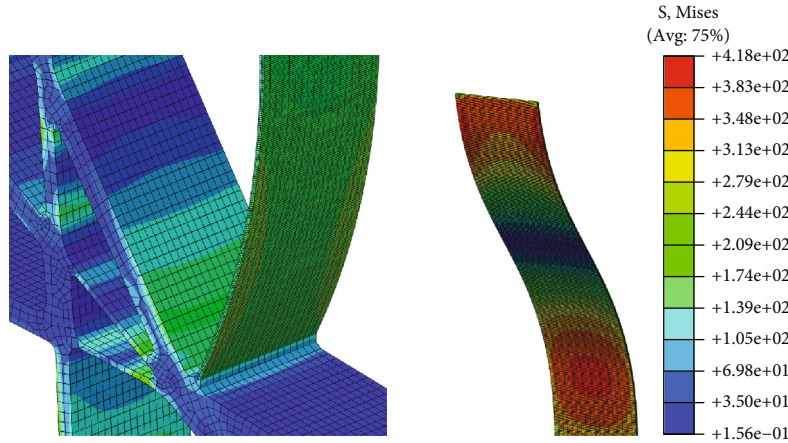
FIGURE 15: Tip rib: detail of the most stressed regions under limit loads.

TABLE 5: Safety margins for the structural verification of the ribs.

	Root rib	Tip rib
Limit loads	0.74	0.12
Ultimate loads	0.49	0.21

morphing skin is made of glass-fibre composite material, and its connection to the compliant ribs is made through the stringers. The manufacturing of the skin is intended to be performed in two halves, split at the stringer, and brought together using two curing stages. Regarding the stringers, GFRP L-shaped is used. The full integration of the stringers into the internal layers of the skin is assumed. This solution is aimed at minimizing the local stiffness in the chord direction, providing a more localized actuation of the skin. The result is the reduction of the skin local waviness. The internal ribs made of aluminium are glued to the lower stringers and are hinged to the upper stringer.

The proposed connection scheme between ribs, stringers, and skin is represented in Figure 16. In particular, the hinged connection in the upper part can be distinguished.

As already explained in the structural design section, the presence of an inspection panel is conceived on the bottom surface of the skin in order to provide access inside the droop nose as well as to be able to disassemble the device from the remainder of the structure.

In the design phase conducted by means of finite element analysis, the presence of the panel is simply introduced as a clamp constraint to model the region that is intended to remain fixed, and that does not follow the deployment of the device. Now, in the detailed CAD modelling phase, a practical solution for the realization of the panel is proposed, along with the support structure that keeps it closed in operative conditions. The inspection panel extends along the entire span of the droop nose, with a maximum chordwise length of 150 mm. Figure 17 shows a detailed view of the support structure. It consists of small rigid ribs connected to an additional stringer, which is used as bottom connection for the morphing skin and for inspection panel installation. Definitively, the skin of the morphing device is connected

to the upper spar cap and to the stringer used for the inspection panel installation.

Regarding the actuation system for introducing the morphing shape variation, it consists of a kinematic chain driven by the rotation of a shaft. The relative dimension of cams and rods, and also the position of the shaft vary from the root wing section to the tip one. As shown in Figure 18, the design of the kinematic chain is performed in a parametric way, based on CAD capabilities. Indeed, rotating the shaft of 70 deg, the stroke required by the input actuation point of each compliant rib along the wingspan is achieved.

The shaft shall be able to reach every rotation angle up to the maximum one, and it shall be braked in the reached position. Therefore, thanks to the brake of the actuators, it is possible to stop the morphing device in each position, in particular the initial one and the maximum deflected one. The driveshaft is cut in two parts, and the load is distributed between them. The torque overrotation curves for the two parts are reported in Figure 19. The evaluation of the required torque considers both the stiffness of the compliant structure and the applied aerodynamic loads.

In order to meet the torque requirements, the selected actuators are two rotary actuators, installed in the fuselage and partially inside the nacelle, and one linear actuator, inside the wing-box, for the outer wing. Regarding the specifications of the rotary actuators, the motor peak torque is 11.5 Nm, there is a gearbox whose torque ratio is 60; hence, with an efficiency of 95%, it is possible to obtain a torque of 655 Nm, which is compatible with the request. The total weight of the actuators is 24 kg. The time needed to complete the total rotation is about 20 s, which is in accordance with the actuation time requirement. The detailed view of the actuators installation, compatible with the available space, is shown in Figure 20.

The connection of the actuation system to the front spar is reported in Figure 21, which also represents the first assembly step for the complete installation of the droop nose on the wing-box structure.

As better explained in the final verification section, a bird strike protection system made of some splitters is needed for such kind of morphing leading-edge device in order to satisfy
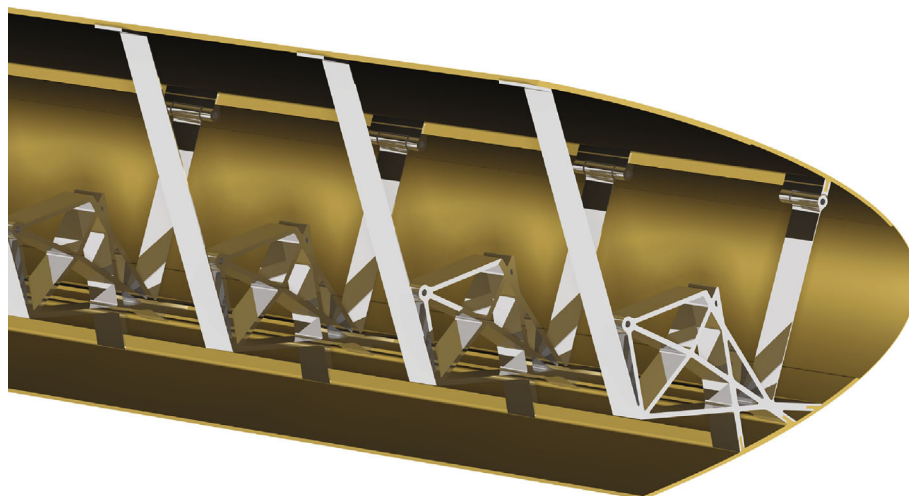
FIGURE 16: Detail of the assembly between the rib and the skin.
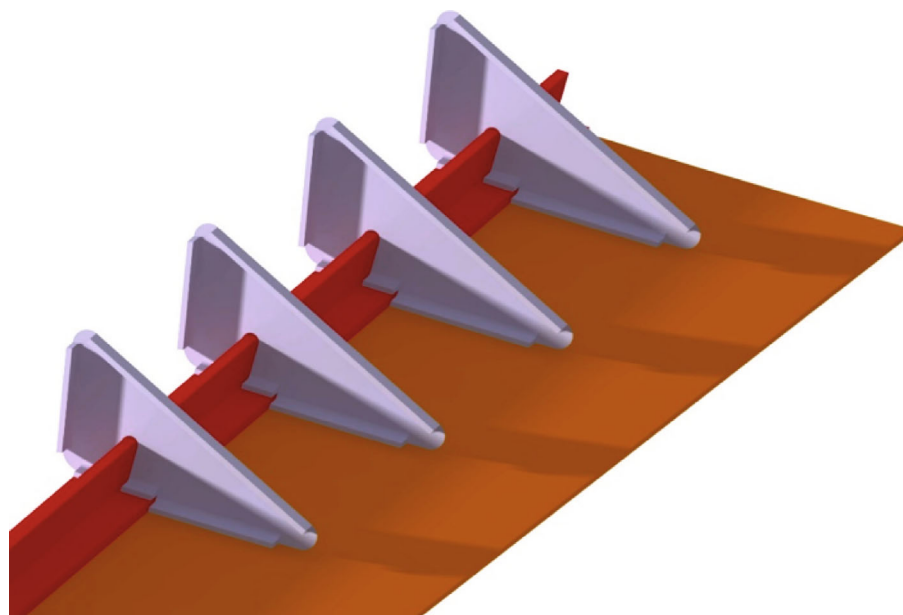
FIGURE 17: Support structure for the removable inspection panel.

the related certification requirements. The designed splitters are located between each pair of consecutive compliant ribs; hence, they are perfectly integrated inside the device. The second assembly step, shown in Figure 22, is the mounting of the splitters that are connected to the upper and lower spar caps. The rigid ribs for supporting the inspection panel are fixed to these splitters.

During the third step, the morphing droop nose is mounted on the wing-box connecting the skin to the upper and lower spar caps, while the compliant ribs are joined to the rods of the actuation system, working through the inspection panel. The bottom accessibility can be observed in Figure 23.

Finally, the inspection panel is mounted, and the complete wing is closed. The whole wing, made of the develop droop nose device attached to the wing-box, is depicted in Figure 24.

At the end of the modelling, some weight considerations are drawn. The weight per unit length of the morphing droop nose is 11 kg/m for the inboard region and 9.2 kg/m for the outboard region. This estimation considers the skin and the internal structure, but not the actuators. The obtained result in terms of the total weight is comparable with the typical values of leading-edge structures for aircraft of the same category, which feature values of 13 kg/m and 6.5 kg/m, with and without slat, respectively. Table 6 summarizes the maximum required torque, the weight of the actuators, and the weight per unit length of the morphing droop nose.

6. Virtual Prototype Tests

Advanced finite element simulations are performed to evaluate the interactions between the morphing droop nose and
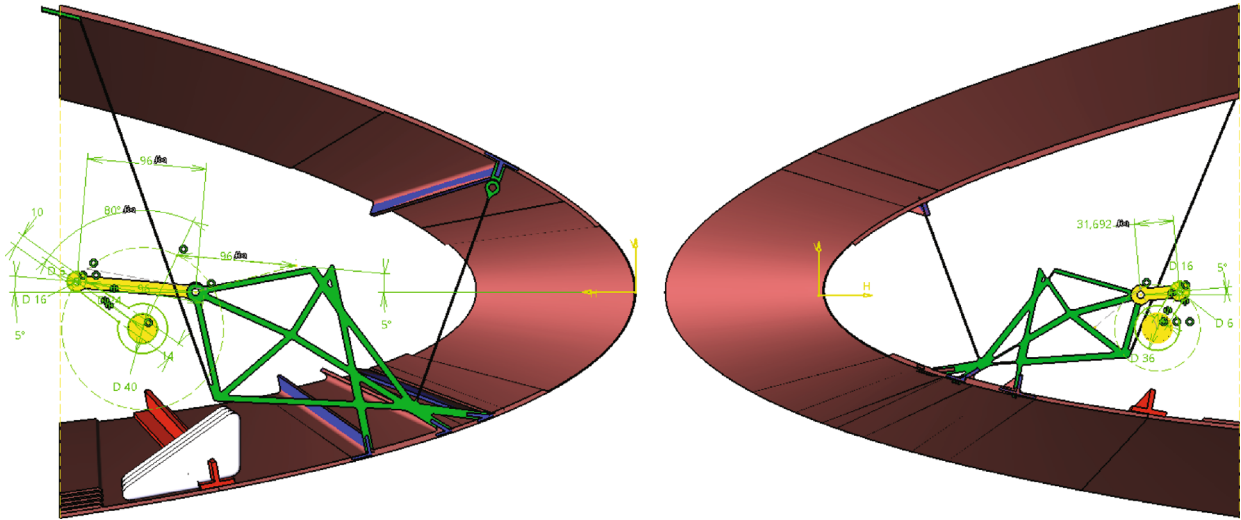
FIGURE 18: Parametric CAD model of the kinematic chain for the actuation system. Root section (left) and tip section (right).
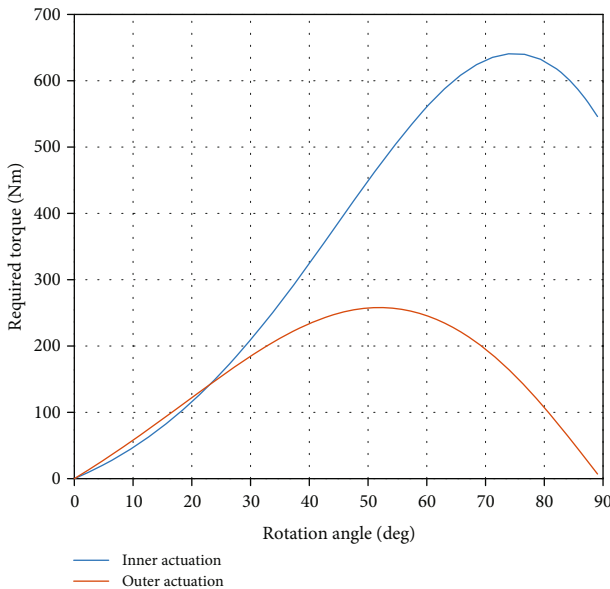
FIGURE 19: Required torque to achieve the requested shaft rotation.

the structural wing-box in terms of both deformability and bird strike safety requirement. This kind of analysis, on the adopted high-fidelity numerical models, is virtual prototype tests able to reproduce the corresponding experimental tests that represent the next step of the droop nose technology development.

6.1. Droop Nose/Wing-Box Interaction. A verification of the mutual interaction between the morphing droop nose device and the structural wing-box is performed. This verification is needed to evaluate the internal loads exchanged at the front spar, as well as to ensure that no undesired behaviour arises. The detailed complete model of the droop nose is attached to a representative flexible wing-box. Since a detailed FEM model of the TP90 wing-box is not available, a simplified model according the monocoque scheme

has been designed, reproducing the stiffness distribution of the original wing-box.

The root section of the wing-box is clamped to the ground. The droop nose is tied to the wing-box in correspondence of the front spar, both on the upper and the lower surface of the skin. The front spar supports also the shaft, which is connected to the input points of the ribs through the kinematic chain. By applying the rotation of the shaft, the droop nose is deployed to its maximum deflection and the corresponding aerodynamic loads are applied on its external surface. Then, a vertical displacement is imposed at the tip of the wing to simulate the static deflection of the wing under aerodynamic loads. The results of this analysis, which are reported in Figure 25, show that the deformation of the wing minimally affects the behaviour of the morphing device; hence, it can still exhibit the designed functionality; in particular, it can be seen that the maximum strain increment is negligible, from $10000\,\mu\varepsilon$ to $10200\,\mu\varepsilon$.

Moreover, on the one hand, the droop nose deformation does not impact on the wing deformability; on the other hand, the wing deformation does not alter at all the cross-sectional shapes of the droop nose after the maximum morphing deflection is achieved.

6.2. Bird Strike Safety Assessment. A bird impact analysis of the final structural design is carried out to evaluate the crashworthiness capabilities of the morphing leading-edge following the regulations dictated in CS-25.631 [17]. Several numerical techniques are presented in literature to address bird impact simulation. The Lagrangian one is chosen in this work, because it offers accurate contact pressure time histories with sustainable computational efforts [18]. All the simulations are performed by means of Abaqus/Explicit code with a penalty contact formulation in order to simulate the complex interactions of the impacting body with the skin and the internal components of the investigated structure.

After a characterization of the impacting body, a numerical model used to simulate the response of the morphing leading-edge has been directly derived from the structural
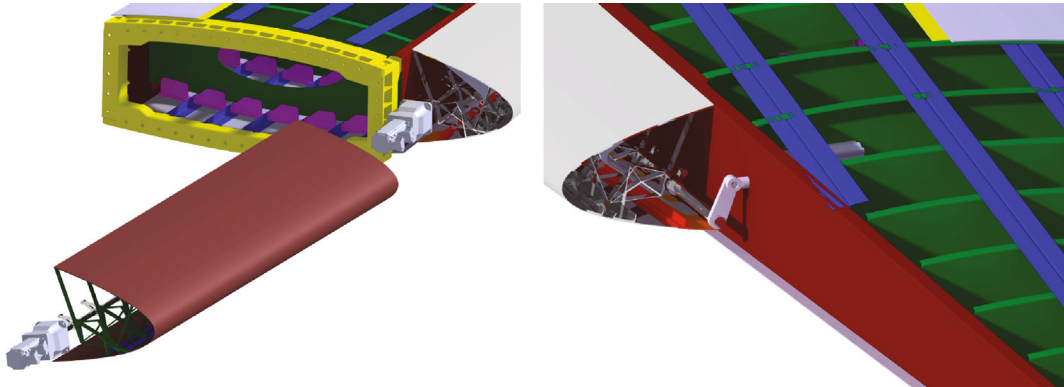
FIGURE 20: Installation studies for the actuators: rotary actuators (left) and linear actuator (right).
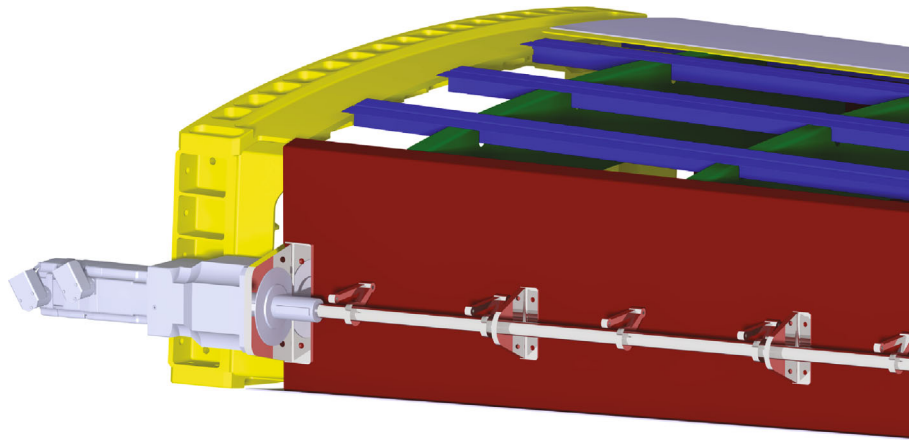
FIGURE 21: Connection of the actuation system to the front spar.
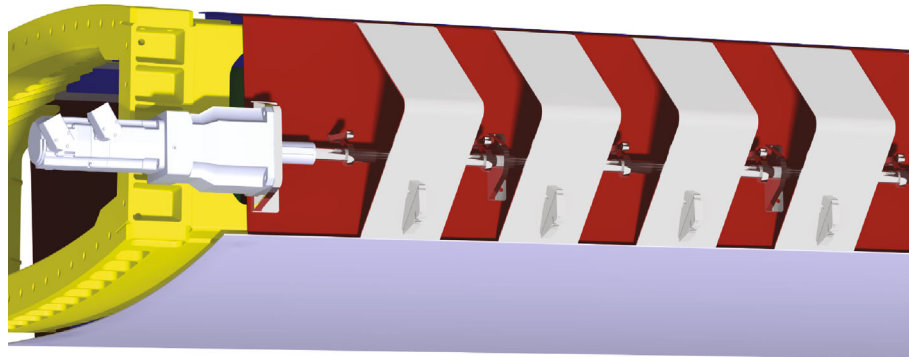
FIGURE 22: Assembly of the splitters on the front spar.

model previously described. Since each internal component provides an additional contribution to the crashworthiness capabilities of the structure, the entire internal mechanism has been modelled. In addition to the adaptive ribs, the actuation shaft and the deployment mechanism are also considered. A nonhomogeneous mesh, with a refinement in the central contact area, is adopted in order to maximize the accuracy without excessively affecting the computational time.

The results described here are related to the impact simulation of a bird with a mass of 1.82 kg (4 lb) and initial velocity of 142.46 m/s. The assumed velocity (relative to the bird along the aircraft flight path) is computed considering the most critical between V_C at sea-level and 0.85 V_C at 2438 m (8000 ft), according to CS-25.631 regulation. For the studied aircraft:

(i) At 2438 m, $V_C = 154.3203$ m/s (Mach = 0.4665) and 0.85 $V_C = 131.1722$ m/s

(ii) At 0 m, $V_C = 142.46$ m/s

Hence, the second one velocity is selected for the simulations.
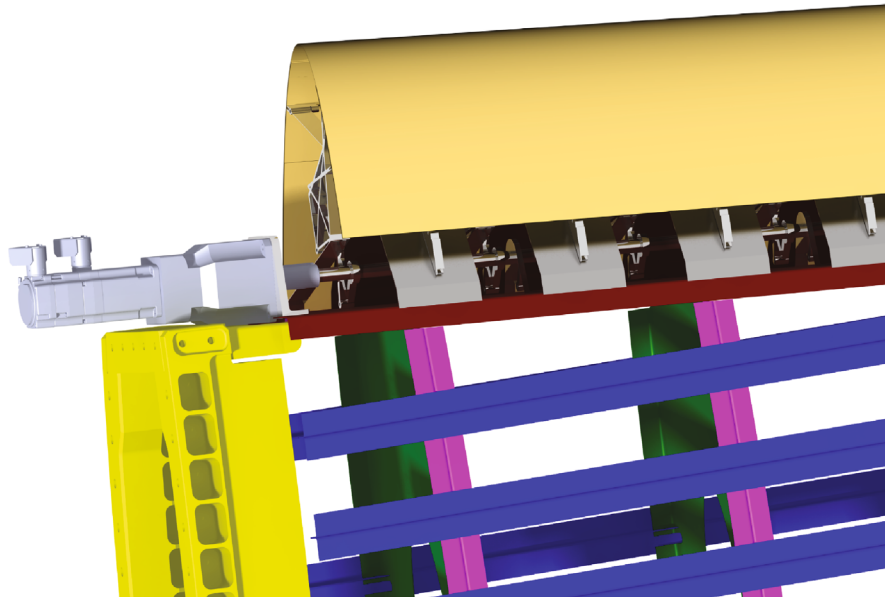
FIGURE 23: Assembly of the morphing droop nose and bottom accessibility.
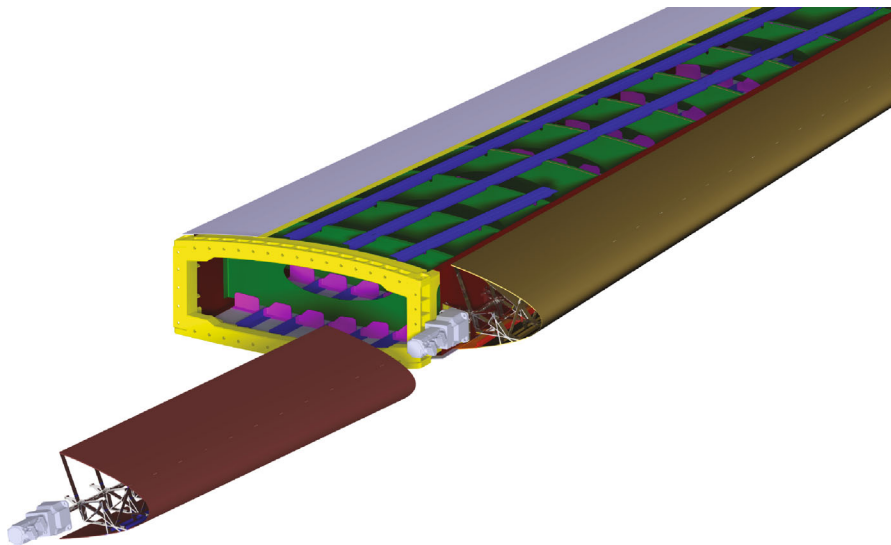
FIGURE 24: CAD model of the wing-box with the droop nose.

TABLE 6: Actuation and weight results summary.

Item	Value	Notes
Maximum torque	655 Nm	Computed with aerodynamic loads
Actuators weight	24 kg	Two rotary actuators, one linear actuator
Droop nose weight per length	11 kg/m (inboard)	Kinematic chain and compliant skin included;
	9.2 kg/m (outboard)	actuators and sensor system not included

The conducted bird impact study proves that the leading-edge morphing structure is characterized by a poor impact response, due to the fact that the skin is very thin and there is also a limited number of supports and stringers, particularly in the regions where a significant morphing shape change is applied. Therefore, it is required for the airworthi-ness certification the implementation of mitigation measures acting to protect the spar from accidental contacts. Several solutions, such as internal hybrid protection systems that absorb, split, and deviate the impacting body [19], should be considered. To this aim, some splitters are conceived to contribute to the absorption of the impact energy. They are
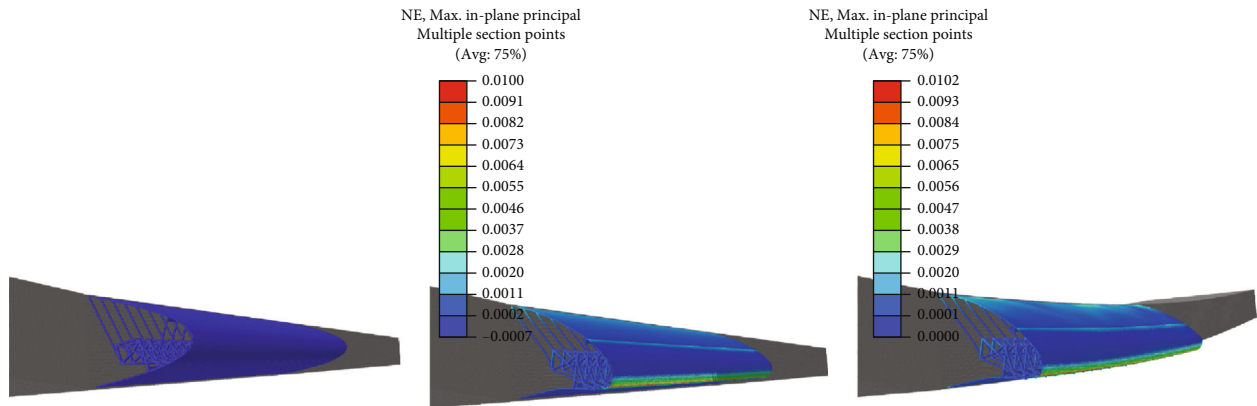
FIGURE 25: Assessment of the interaction between droop nose device and wing-box.
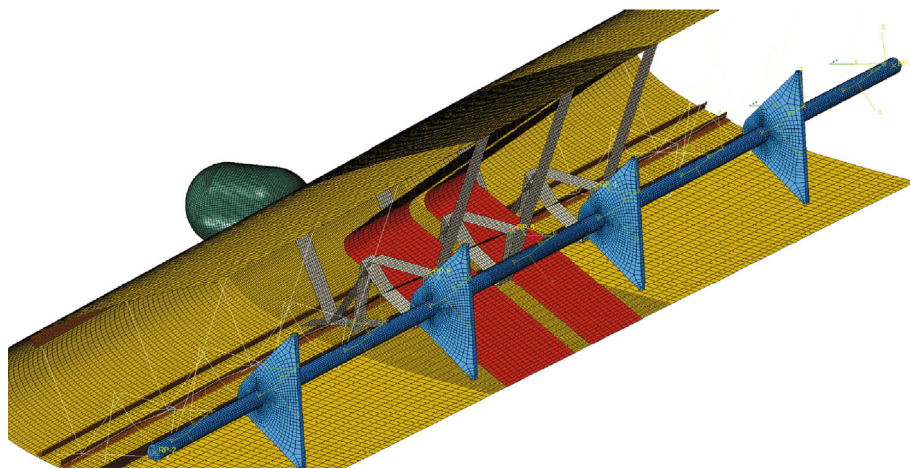
FIGURE 26: Testing facility for the bird impact simulation on the overall LE structure.
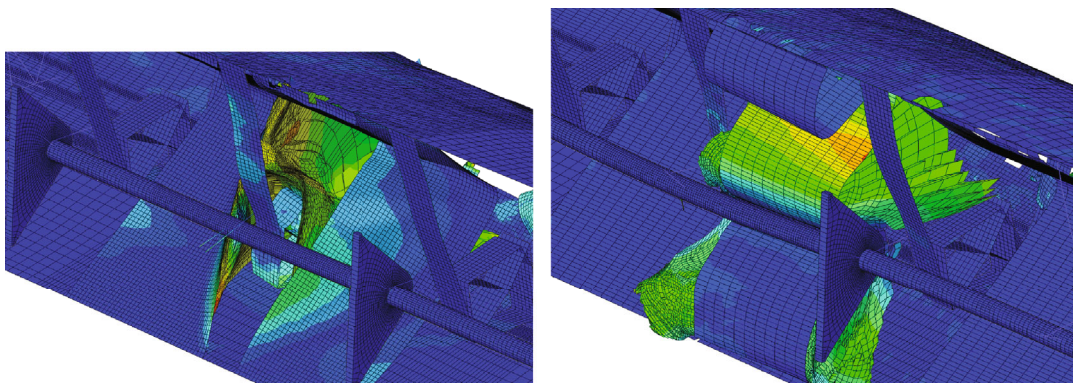
FIGURE 27: Bird strike test: impact on a compliant rib (left) and impact between two compliant ribs (right).

placed between each couple of consecutive compliant ribs and are modelled using 2D elements. The model for the numerical simulation including the splitters and the impacting bird is represented in Figure 26.

Two different analyses are performed. The first analysis considers the bird impacting on a compliant rib, while the other analysis assumes the bird impacting between two compliant ribs.

The two cases are illustrated in Figure 27. In the first scenario, the numerical simulation shows that the bird penetrates the skin structure, the splitters near at the impact region absorbs part of the bird energy and then the compliant rib absorbs the impact energy without fractures. In the second scenario, the skin cannot still absorb the impact energy. The splitter deforms and this time it impacts against the front spar of the wing. The splitter collapses because the bird does
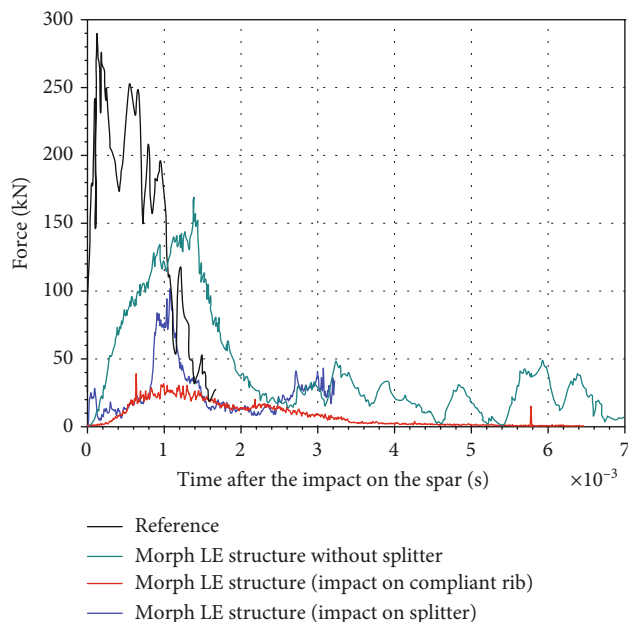
FIGURE 28: Bird strike test: reaction force on the front spar.

not impact in its centre, as instead modelled during the splitter design.

Anyway, the splitter reduces the overall reaction force on the front spar, as depicted in Figure 28. The reduction with respect to the situation without splitters is of the 75% if the impact is on a compliant rib, and it is of the 40% if the impact is between two ribs. Therefore, the introduction of splitters is essential to guarantee the bird impact requirement.

7. Conclusions

This paper describes the advanced design phase of a morphing droop nose device to be installed on a 90 passengers regional aircraft, in the framework of the Clean Sky 2 Airgreen project. The design starts from the preliminary results obtained for the optimal aerodynamic shape and the topology solution of the internal structure.

The detailed design is conducted with the aim to achieve the requested performance, while satisfying all the requirements for the device under analysis. A special effort is devoted to guarantee the structural feasibility of the conceived solution in terms of strength assessment. The structural design phase includes considerations about the accessibility of the device, foreseeing the presence of a removable inspection panel.

Verification on a medium-fidelity model of the complete device is performed, followed by detailed analyses on higher fidelity models of the internal structure. The results confirm the validity of the solution obtained by means of the proposed optimization procedures.

After that, starting from the finite element models, a complete corresponding CAD model is realized. At this phase, the assembly of the various components of the device is modelled in detail, including the actuators and the kinematic chain conceived to accomplish the morphing shape

change. Regarding the actuation system, studies on the required power are conducted, leading to the selection of the suitable actuators, also considering the occupied space for the installation. Moreover, weight estimation is presented.

Finally, other important verifications are reported. A static assessment validates the interaction between the designed device and the structural wing-box. Bird strikes analyses are conducted in various cases to ensure the safety of the leading-edge device according to the certification rules, showing the need for an appropriate support structure to absorb the impact energy.

The results reported here demonstrate the high TRL achieved by the DN morphing project and show how the solution adopted is ready for experimental validation. A 1 : 3 scale test will be conducted by 2020 within the same project on a wind tunnel test model. After this activity, it is possible to imagine a full-scale test of a prototype developed for the final evaluation phase.

Data Availability

All the data supporting the results were shown in the paper and can be applied from the corresponding author.

Conflicts of Interest

The authors declare that there is no conflict of interest regarding the publication of this paper.

Acknowledgments

References

[1] S. Barbarino, O. Bilgen, R. M. Ajaj, M. I. Friswell, and D. J. Inman, "A review of morphing aircraft," *Journal of Intelligent Material Systems and Structures*, vol. 22, no. 9, pp. 823–877, 2011.

[2] A. De Gaspari, L. Riccobene, and S. Ricci, "Design, Manufacturing and Wind Tunnel Test of a Morphing Wing Based on Compliant Structures," in *24th AIAA/AHS Adaptive Structures Conference*, pp. 307–324, Curran Associates, Red Hook, NY, San Diego, California, USA, 2016.

[3] J. Cooper, A. Suleman, S. Ricci et al., "SMorph—Smart Aircraft Morphing Technologies Project," in *51st AIAA/ASME/AS-CE/AHS/ASC Structures, Structural Dynamics, and Materials Conference*, pp. 1–14, Orlando, Florida, 2010.

[4] G. Diodati, A. Concilio, S. Ricci et al., "Estimated performances of an adaptive trailing edge device aimed at reducing fuel consumption on a medium–size aircraft," in *Industrial and Commercial Applications of Smart Structures Technologies 2013*, pp. 1–16, San Diego, CA, USA, 29 March 2013.

[5] A. De Gaspari and S. Ricci, "A Two-Level approach for the optimal design of morphing wings based on compliant structures," *Journal of Intelligent Material Systems and Structures*, vol. 22, no. 10, pp. 1091–1111, 2011.

[6] S. Kota, R. Osborn, G. Ervin, D. Maric, P. Flick, and D. Paul, "Mission Adaptive Compliant Wing: Design, Performance and Flight Test Results," in *50th AIAA/ASME/ASCE/AHS/ASC Structures, Structural Dynamics, and Materials Conference*, Evora, Portugal, 4 May 2009.

[7] A. De Gaspari, A. Gilardelli, S. Ricci, and A. Airoldi, "Design of a Leading Edge Morphing Based on Compliant Structures for a Twin–Prop Regional Aircraft," in *2018 AIAA/AHS Adaptive Structures Conference*, Kissimmee, Florida, 8 Jan 2018.

[8] F. Rea, F. Amoroso, R. Pecora, and F. Moens, "Exploitation of a Multifunctional Twistable Wing Trailing–Edge for Performance Improvement of a Turboprop 90–Seats Regional Aircraft," *Aerospace*, vol. 5, no. 4, 2018.

[9] F. Moens, "Augmented Aircraft Performance with the Use of Morphing Technology for a Turboprop Regional Aircraft Wing," *Biomimetics*, vol. 4, no. 3, 2019.

[10] A. De Gaspari and S. Ricci, "Knowledge-based shape optimization of morphing wing for more efficient aircraft," *International Journal of Aerospace Engineering*, vol. 2015, Article ID 325724, 19 pages, 2015.

[11] M. Drela, "A User's Guide to MSES 3.05," *MIT - Department of Aeronautics and Astronautics*, 2007, http://web.mit.edu/drela/Public/web/mses/mses.pdf.

[12] L. Cambier, S. Heib, and S. Plot, "The OneraelsACFD software: input from research and feedback from industry," *Mechanics & Industry*, vol. 14, no. 3, pp. 159–174, 2013.

[13] A. De Gaspari and F. Moens, "Aerodynamic shape design and validation of an advanced high-lift device for a regional aircraft with morphing droop nose," *International Journal of Aerospace Engineering*, vol. 2019, Article ID 7982168, 21 pages, 2019.

[14] K. Deb, *Multi-Objective Optimization Using Evolutionary Algorithms*, Wiley, 2005.

[15] "Simulia, "Abaqus Analysis User's guide," Simulia Help".

[16] S. Vasista, J. Riemenschneider, B. van de Kamp et al., "Evaluation of a compliant droop-nose morphing wing tip via experimental tests," *Journal of Aircraft*, vol. 54, no. 2, pp. 519–534, 2017.

[17] EASA European Aviation Safety Agency, "Certification Specifications and Acceptable Means of Compliance for Large Aeroplanes CS-25," Amendment 20, 24 August 2017.

[18] "Simulia, "A Strategy for Bird Strike Simulations using Abaqus/Explicit," Simulia Help".

[19] C. Chary, "Development and validation of a bird strike protection system for an enhanced adaptive droop nose," in *Smart Intelligent Aircraft Structures (SARISTU)*, M. Papadopoulos, Ed., pp. 71–83, Springer, Cham, 2016.

Research Article

Static Aeroelastic Characteristics of Morphing Trailing-Edge Wing Using Geometrically Exact Vortex Lattice Method

Sen Mao [ID], **Changchuan Xie** [ID], **Lan Yang** [ID], **and Chao Yang**

School of Aeronautic Science and Engineering, Beihang University, 100191 Beijing, China

Correspondence should be addressed to Changchuan Xie; xiechangc@buaa.edu.cn

A morphing trailing-edge (TE) wing is an important morphing mode in aircraft design. In order to explore the static aeroelastic characteristics of a morphing TE wing, an efficient and feasible method for static aeroelastic analysis has been developed in this paper. A geometrically exact vortex lattice method (VLM) is applied to calculate the aerodynamic forces. Firstly, a typical model of a morphing TE wing is chosen and built which has an active morphing trailing edge driven by a piezoelectric patch. Then, the paper carries out the static aeroelastic analysis of the morphing TE wing and corresponding simulations were carried out. Finally, the analysis results are compared with those of a traditional wing with a rigid trailing edge using the traditional linearized VLM. The results indicate that the geometrically exact VLM can better describe the aerodynamic nonlinearity of a morphing TE wing in consideration of geometrical deformation in aeroelastic analysis. Moreover, out of consideration of the angle of attack, the deflection angle of the trailing edge, among others, the wing system does not show divergence but bifurcation. Consequently, the aeroelastic analysis method proposed in this paper is more applicable to the analysis and design of a morphing TE wing.

1. Introduction

Morphing aircraft can change the shape of air vehicles and vehicle components to adapt to a changing mission environment and achieve the best flight performance in a variety of missions. Compared with other morphing aircraft designs, a morphing TE wing outstandingly improves the aerodynamic characteristics of the aircraft. It also has a remarkable influence on low-speed cruise and on the take-off and landing of aircrafts. There are many structural forms of morphing TE wings such as a traditional morphing TE wing which is a hinged structure driven by a motor and a smart structure TE morphing wing based on smart materials [1]. Each morphing TE wing has its own advantages and disadvantages.

A growing body of research is dedicated to the application of piezoelectric materials to a morphing wing. FlexSys Inc. of USA designed a wing structure that can achieve continuous variable camber, with a trailing-edge deflection of -10°~+10°. The wing based on a piezoelectric ceramic driver serves to achieve high frequency wing rapid deformation [2]. Kansas University has conducted research on a novel pie-

zoelectric actuator to drive tip deformation of microaircraft [3]. Flight tests showed excellent roll control of the piezoelectric actuator for the microaircraft. In the same year, the Canadian National Research Council Institute of Aeronautics developed a flexible curved wing with MFCs [4]. The MFCs were employed to drive the trailing edge of the wing to bend. Moreover, Onur Bilgen from Virginia Tech University (USA) designed a control system for wingtip torsional deformation of microaircraft by virtue of a macrofiber composite (MFC) and tested the driving performance of MFC for glass fiber composite patches [5]. Wind tunnel tests were conducted to study the difference between the trailing-edge control and the MFC driving wing. The results demonstrated that the resistance of the MFC-driven composite wing is lower, and the driving bandwidth is wider. The flight test was successfully carried out then. Afterward, the German Aerospace Center conducted an active torsional rotor research [6] by embedding piezofiber composite actuators with different lay angles in the rotor. Furthermore, a span-wise morphing trailing-edge concept was proposed by Pankonien and Inman in a modular design of 12 alternating active and

passive aileron sections [7]. The active ailerons were driven by macrofiber composites which bent the trailing edge to cause a smooth chord-wise camber change of airfoils. Also, wind tunnel tests at a flow speed of 10 m/s were carried out by virtue of a hardware demonstrator. Results indicated that the developed span-wise morphing trailing edge led to excellent aerodynamic and structural performance. In addition, Ohanian et al. and Kochersberger et al. compared a novel morphing control surface design employing piezoelectric MFC actuators with a servo-actuated system [8–10]. A comprehensive comparison including aerodynamics, size, weight, power, bandwidth, and reliability has been extended to include flight test comparisons. The morphing actuation scheme demonstrated a control bandwidth that was an order of magnitude greater than for the servo-actuated system, but showed a 12% decrease in roll rate when compared to the servo-actuated baseline aircraft. Flight tests are planned to fully prove the benefits of the morphing actuation which achieved 1 million cycles without failure and minimal degradation over a servo-actuated design.

However, there are still deficiencies in these studies. Firstly, the aerodynamic forces in the previous studies are all calculated based on CFD, which can inarguably generate accurate aerodynamic results but not lend itself to structure optimization and control system design of the morphing wing due to its time-consuming nature. Secondly, most previous researches concentrated on the realization of a deformation mechanism without giving equal prominence to the effects of wing deformation on the aerodynamics. At last, in these studies, the aeroelastic characteristics were examined only after the design had been completed, which renders it difficult to remedy potential design flaws. Different from the above research, Li et al. made an investigation into the nonlinear aeroelastic behavior of a composite wing with morphing trailing edge actuated by curved beams [11]. In the analysis, a doublet lattice method was used to calculate unsteady aerodynamic force. Results suggested that wing deformation was correlated with aeroelastic responses of the composite wing. In addition, the aeroelastic method based on VLM is very mature. Stanford and Beran optimized the design of a flapping wing in forward flight with active shape morphing using an inviscid three-dimensional unsteady vortex-lattice method [12]. Xie et al. used a nonplanar VLM to compute the nonplanar aerodynamics of flexible wings with large deformation [13]. The VLM boasts a moderate level of fidelity and a relatively inexpensive cost of computation. However, as a result of the linearization of boundary conditions, the traditional linear VLM loses sight of the influence of geometric deformation on an aerodynamic influence coefficient matrix. This method is not applicable to the aeroelastic analysis of a morphing wing, especially when the aerodynamic shape is changed significantly compared with the initial one. To offset the aforementioned deficiencies, a new aerodynamic calculation method based on nonplanar VLM is proposed herein to serve as a static aeroelastic analysis method for a morphing TE wing. This new method can play a better role in shedding light on the aerodynamic charac-

teristics of the 2D wing with the control surface than the conventional linearized VLM, hereinafter referred to as geometrically exact VLM.

In Section 2, a 2D wing with an active morphing trailing edge driven by a piezoelectric patch was chosen as the research object to analyze its static aeroelastic characteristics. In Section 3, a set of numerical validations are carried out and the analysis results are compared with traditional wings with a rigid trailing edge by the traditional linearized VLM. The results not only theoretically deepen the understanding of the aerodynamic and aeroelastic characteristics of a morphing TE wing, but they also provide the theoretical basis for further research on a comprehensively optimized design of a morphing TE wing.

2. Methodology

2.1. Morphing Piezoelectric Wing Model. The main purpose of this paper is to establish a clear and accurate aeroelastic formulation of the morphing TE wing and shed light on its aeroelastic properties by virtue of the geometrically exact VLM. Thus, a typical and simple model of the morphing TE wing is chosen and analyzed which has an active morphing trailing edge driven by a piezoelectric patch, hereinafter referred to as the morphing piezoelectric wing. In particular, there is no gap between the wing and the active morphing trailing edge, as opposed to traditional wings with a rigid trailing edge. The morphing piezoelectric wing is modeled as a beam, as shown in Figure 1. X-0-Y is a rectangular coordinate system on the ground. x-0-y is the rectangular coordinate system for the rigid part of the wing, while s-0-n is the rectangular coordinate system for the elastic bending part of the wing. The piezoelectric patch covers the trailing edge of the wing which is taken as the active morphing trailing edge, and the length of the trailing edge is denoted as l_2, while the length of the other part of the wing is denoted as l_1. According to the characteristics of the piezoelectric patches, the bending moment M_P is generated to deform the beam when a voltage is added to both ends of the patch. The voltage is denoted as piezoelectric voltage U, and the trailing-edge deflection angle is denoted as β. A torsion spring is installed, of which the stiffness is equivalent to the pitch stiffness K_θ. The angle of attack is α, and the pitch angle is θ. It is generally considered that the wing profile is rigid. And all deformation of the beam is assumed to be caused by piezoelectric torque. The entire wing rotates around the torsion spring under aerodynamic load. This is therefore a simple rigid-elastic coupling dynamics model. Meanwhile, the simulation does not take into account the piezoelectric voltage limit, the installation form of the piezoelectric patches, and the nonlinear factors of the piezoelectric patches.

2.2. Piezoelectric Trailing Edge Deformation. The geometrical deformation of the trailing-edge may be considerable under the action of piezoelectric moments in Figure 1. Therefore, a small deformation assumption is not used when describing wing deformation in this paper. This is a geometric nonlinear problem with large deformation and small strain. The
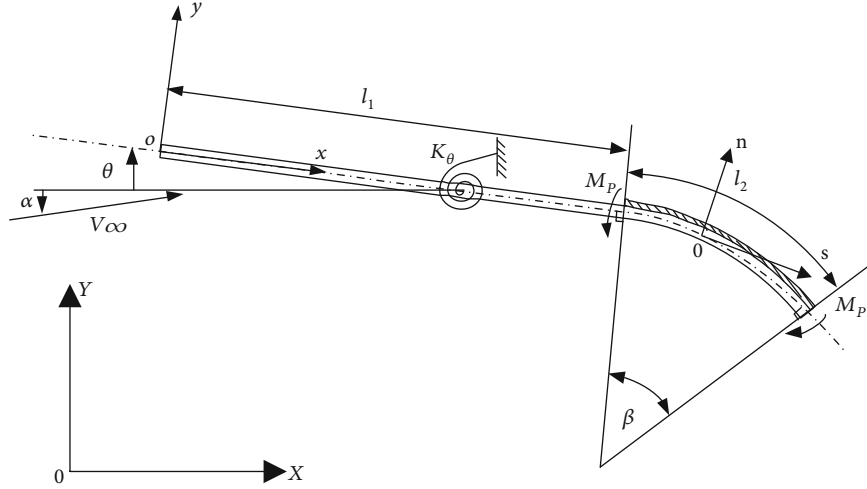
FIGURE 1: The morphing piezoelectric wing model.

bending strain ε in the cross section can be obtained through the linear constitutive equation:

$$\varepsilon = \frac{n}{\rho}, \tag{1}$$

where ρ represents the radius of curvature of the trailing-edge and n represents the distance from the neutral layer.

The upper surface bending strain ε_s is as follows:

$$\varepsilon_s = \frac{H}{2\rho}, \tag{2}$$

where H represents the thickness of the trailing-edge.

The relationship between the bending moment of the beam M_s and the deformation of the beam can be expressed as

$$\frac{1}{\rho} = \frac{M_s}{E_s I_s}, \tag{3}$$

where E_s represents the elastic modulus of the beam and I_s represents the section moment of inertia.

Notably, the piezoelectric constitutive equation can be expressed as [14]:

$$\sigma_{px} = E_p(\varepsilon_{px} - d_{31}E_e), \tag{4}$$

where E_p stands for the elastic modulus of the piezoelectric patch, d_{31} is the piezoelectric constant, E_e stands for the strength of an electric field around the piezoelectric patch, σ_{px} stands for the stress of the piezoelectric patch, and ε_{px} stands for the strain of the piezoelectric patch, respectively. The piezoelectric patches are assumed as very thin, consequently σ_{px} and ε_{px} can be constant. No change occurs to the neutral layer of the beam after the piezoelectric patch is attached to the beam surface. The strain of the piezoelectric

patch along the x direction is equal to the strain of the beam on the upper surface as follows:

$$\varepsilon_{px} = \varepsilon_s. \tag{5}$$

For ease of calculations, it is assumed that the neutral layer of the beam does not change while the thickness of the piezoelectric patch cannot be ignored. Accordingly, the bending moment of the piezoelectric patch can be written as

$$M_p = b \int_{H/2}^{(H/2)+h} \sigma_{px} z\,dz = b \int_{H/2}^{(H/2)+h} E_p\left(d_{31}E_e - \frac{z}{\rho}\right) z\,dz, \tag{6}$$

where h represents the thickness of the piezoelectric patch and M_p represents the bending moment of the piezoelectric patch. M_p and M_s refer to the relationships between internal forces, which can be expressed as

$$M_p = -M_s. \tag{7}$$

Finally, by assembling equations (1), (2), (3), (4), (5), (6) and (7), the trailing-edge deflection angle can be calculated by the following equation:

$$\beta = \frac{1}{1 + (2h/H) + (4h^2/3H^2) + (A_s E_s / 3A_p E_p)} \\ \cdot d_{31} U\left(\frac{1}{H} + \frac{1}{h}\right) \cdot \frac{2l_2}{H}. \tag{8}$$

As to the aerodynamic calculation, the thin-airfoil camberline is divided into n distributed subpanels where the piezoelectric trailing edge is equally divided into n_2 distributed subpanels and the other part is equally divided into n_1 distributed subpanels. It is notable that the trailing

edge deflection angle and piezoelectric voltage are linearly dependent; accordingly, a discrete expression of equation (8) is defined as

$$
K_{\mathrm{p}i} = \begin{cases} 0, & 1 \le i \le n_1, \\ \dfrac{1}{1 + (2h/H) + \left(4h^2/3H^2\right) + \left(A_s E_s/3A_{\mathrm{p}} E_{\mathrm{p}}\right)} \cdot d_{31}\left(\dfrac{1}{H} + \dfrac{1}{h}\right) \cdot \dfrac{2l_2(i - n_1)}{Hn_2}, & n_1 + 1 \le i \le n_1 + n_2. \end{cases} \tag{10}
$$

2.3. Aerodynamic Force Calculation of Morphing Wing.

The present study considers the aerodynamic force of the 2D wing as a thin airfoil with a significantly different configuration, regardless of the actual conditions of its airfoil. The position vector of the camberline can be expressed as a parametric equation as follows:

$$
\beta_i = K_{\mathrm{p}i} U, \tag{9}
$$

where

$$
\mathbf{r} = x(s)\mathbf{e}_X + y(s)\mathbf{e}_Y, \tag{11}
$$

where $\mathbf{e}_X$ and $\mathbf{e}_Y$ are the basis of $X\text{-}0\text{-}Y$.

The expressions of the total aerodynamic lift L and the total aerodynamic moment M are as follows [15]:

$$
\begin{cases} L = qS \displaystyle\int_0^l C_{\mathrm{p}} \dfrac{dx(s)}{ds}\, ds = qS \displaystyle\int_0^l C_{\mathrm{p}} \cos\varphi\, ds, \\[4mm] M = \displaystyle\int_0^l qS C_{\mathrm{p}} \left(\dfrac{d\mathbf{r}}{ds} \times (\mathbf{r} - \mathbf{r}_0)\right) ds = qS \displaystyle\int_0^l C_{\mathrm{p}}\big((x(s) - x_0)\cos\varphi + (y(s) - y_0)\sin\phi\big)\varphi\, ds, \end{cases} \tag{12}
$$

where q represents the dynamic pressure around the wing, S represents the reference wing area, C_{p} represents the aerodynamic pressure coefficient distribution at s, x_0 and y_0 represent the coordinates of the positions of the torsion spring, and φ represents the local downwash angle.

VLM is a numerical method for solving the steady aerodynamic loads of a 2D wing. Herein, the thin-airfoil camberline is divided into n equally distributed subpanels, and the n vortex points are placed at the quarter-chord point of each panel. Accordingly, the aerodynamic force can be written as

$$
\begin{cases} L = \displaystyle\sum_{i=1}^{n} qS C_{\mathrm{p}i} \cos\varphi_i \Delta s_i, \\[4mm] M = \displaystyle\sum_{i=1}^{n} qS C_{\mathrm{p}i} \cdot \big((x_i - x_0)\cos\varphi_i - (y_i - y_0)\sin\varphi_i\big)\Delta s_i, \end{cases} \tag{13}
$$

where $C_{\mathrm{p}i}$ represents the aerodynamic pressure coefficient distribution at the ith panel. Δs_i represents the length of the ith panel, and φ_i represents the local downwash angle. The aerodynamic force obtained by equation (13) is based on the real aerodynamic shape considered as the aerodynamic force obtained by the geometrically exact VLM in this context.

When the traditional linear VLM is used in aeroelastic analysis, the aerodynamic force is independent of the local downwash angle. The aerodynamic solution formula of traditional linear VLM can be simplified by equation (13) as

$$
\begin{cases} L = \displaystyle\sum_{i=1}^{n} qS C_{\mathrm{p}i} \Delta s_i, \\[4mm] M = \displaystyle\sum_{i=1}^{n} qS C_{\mathrm{p}i} \cdot (x_i - x_0)\Delta s_i. \end{cases} \tag{14}
$$

In addition to the difference in the aerodynamic solution formula, the difference between the two VLMs is also reflected in the solution of pressure coefficient distribution.

When the aerodynamic force is calculated by traditional linearized VLM, the aerodynamic influence coefficient matrix is regarded as constant. Besides, the boundary conditions are linearized. Consequently, the aerodynamic forces mentioned above are linear, whose coefficients are constant. The C_{p} can be defined in equation (15) [15] as follows:

$$
\begin{pmatrix} C_{\mathrm{p}1} \\ \vdots \\ C_{\mathrm{p}N} \end{pmatrix} = -\frac{2n}{l} A_0^{-1} \begin{pmatrix} \alpha + \theta + \beta_1 \\ \vdots \\ \alpha + \theta + \beta_n \end{pmatrix}, \tag{15}
$$

where A_0 denotes the aerodynamic influence coefficient matrix before deformation.

Substitute equation (15) into equation (14), and we can obtain

$$\begin{cases} L = -2qSWA_0^{-1}N^T, \\ M = -2qSD_0A_0^{-1}N^T, \end{cases} \tag{16}$$

where $N = [\alpha + \varphi_1, \cdots, \alpha + \varphi_n]$, $\varphi_i = \theta + \beta_i$, $W = [1, \cdots, 1]$, $D_0 = [d_1, \cdots, d_N]$, and d_i denotes the distance from the center of the ith panel to the torsion spring before deformation.

It can be seen from equation (16) that there is a linear relationship between the airfoil pitch angle θ and the aerodynamic moment. So the traditional linearized VLM is very efficient in terms of analyzing the aeroelastic characteristic of the morphing piezoelectric wing. But its accuracy is still inadequate, which is demonstrated in the following two aspects. Firstly, the influence coefficient matrix of the aerodynamic force cannot reflect the influence of the trailing edge control surface. Secondly, the real boundary conditions are not implemented where α and $\sin \alpha$ are considered as equivalent. In order to offset the deficiencies, the geometrically exact VLM is proposed to calculate the aerodynamic forces of morphing wings.

The calculation of the pressure coefficient of the morphing piezoelectric wing by virtue of the geometrically exact VLM is as follows:

$$\begin{pmatrix} C_{p1} \\ \vdots \\ C_{pN} \end{pmatrix} = -\frac{2n}{l} A(U)^{-1} \begin{pmatrix} \sin(\alpha_0 + \theta + \beta_1) \\ \vdots \\ \sin(\alpha_0 + \theta + \beta_N) \end{pmatrix}, \tag{17}$$

where $A(U)$ denotes the influence coefficient matrix of the aerodynamic force which is a matrix function of piezoelectric voltage. This matrix function represents the relationship between wing deformation and influence coefficient matrix.

Substitute equation (17) into equation (13), the aerodynamic lift and moment are shown as

$$\begin{cases} \bar{L} = -2qS\bar{W}A(U)^{-1}(N + \widehat{N})^T, \\ \bar{M} = -2qS\bar{D}A(U)^{-1}(N + \widehat{N})^T, \end{cases} \tag{18}$$

where $\widehat{N} = [\widehat{\varphi}_1, \cdots, \widehat{\varphi}_n]$, $\widehat{\varphi}_i = -(1/6)(\alpha_0 + \varphi_i)^3 + o^3(\alpha_0 + \varphi_i)$, $\bar{W} = [\cos \varphi_1, \cdots, \cos \varphi_n]$, and $\bar{D} = [d_1 \cos \theta, \cdots, d_N \cos \theta]$.

Figure 2 shows the different discrete vortex representations of the morphing wing after deformation using different VLMs. At this phase, the camberline is divided into n subpanels, whose length is Δs_i. In Figure 2(a), the blue line represents the actual aerodynamic surface before deformation. And the red line represents the real aerodynamic surface after deformation. In Figures 2(b) and 2(c), the dots represent the vortex points and the forks represent the control points. The vector $\mathbf{n}_i$ is the normal vector of the ith panel in the aerodynamic surface after deformation which represents the zero normal flow boundary condition. It can be seen from

Figures 2(b) and 2(c) that when the aerodynamic force is calculated by the traditional linear VLM in the presence of deformation of the aerodynamic surface, the positions of the control point and vortex point remain unchanged, and only the boundary condition is changed. When the geometrically exact VLM is employed to calculate the aerodynamic force, the position of the control point and my point will be changed correspondingly with the deformation of the aerodynamic surface. Obviously, it can be seen that the vortex distribution points change significantly when the trailing-edge deflects, so the aerodynamic influence coefficient matrix calculated by VLM cannot be considered as constant.

2.4. Aeroelastic Analysis Using Traditional Linearized VLM. The morphing piezoelectric wing balance equation is defined as follows:

$$M = K_\theta \theta. \tag{19}$$

Based on equations (16) and (19), when the system is in a state of equilibrium, the pitch angle of the airfoil $\theta*$ can be obtained as follows:

$$\theta^* = \frac{-2qSD_0A_0^{-1}(\alpha W^T + UK_P^T)}{K_\theta + 2qSD_0A_0^{-1}W^T}, \tag{20}$$

where $K_P = [K_{p1}, \cdots K_{pN}]$.

The denominator of equation (20) will become zero when the dynamic pressure reaches a certain value, which makes $\theta*$ approach infinity and the 2D wing becomes unstable. The certain dynamic pressure is denoted by divergent dynamic pressure q_{div}. It is a crucial aeroelastic parameter for the wing in that it represents the highest dynamic pressure that the wing can sustain before being destroyed. The q_{div} can be obtained by the following equation using traditional linearized VLM:

$$q_{div} = \frac{K_\theta}{-2SD_0A_0^{-1}W^T}. \tag{21}$$

It can be seen from equation (21) that the divergent dynamic pressure calculated by traditional linearized VLM is proportional to K_θ and is related to the aerodynamic arm D_0. Therefore, increasing the torsional stiffness of the wing or reducing the aerodynamic arm can both improve q_{div}.

The downward deflection of the control surface increases the lift while it produces a negative pitching moment, which makes the 2D wing rotate in the direction of reducing the angle of attack, thereby diminishing the control surface efficiency. The efficiency keeps decreasing with the increase of the dynamic pressure, which even leads to aileron reversal. Aileron reversal is defined as the concurrence of the increase of the trailing edge deflection angle and the decrease of the total lift.

Considering that the airfoil rotated under the aerodynamic load, the lift is given by

$$L_\theta = \frac{L_0 K_\theta - L_0(\partial M/\partial\theta) + M_0(\partial L/\partial\theta)}{K_\theta - (\partial M/\partial\theta)}, \tag{22}$$

(a) Aerodynamic surface before and after deformation

(b) Discrete vortex representation using traditional linear VLM

(c) Discrete vortex representation using geometrically exact VLM
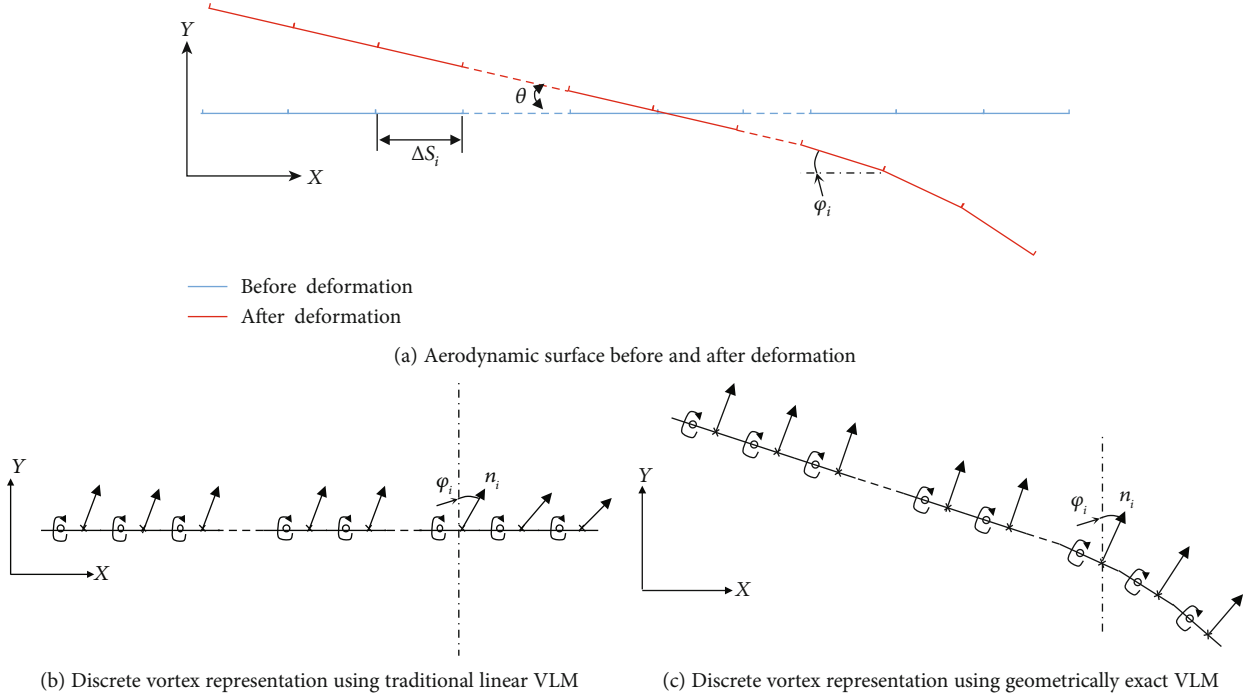
FIGURE 2: The different discrete vortex representations using different VLMs.

where L_0 and M_0 represent the aerodynamic lift and moment prior to aeroelastic deformation which can be obtained by equation (16) when θ is set to zero.

When the lift becomes zero, the control surface fails to work, thus the efficiency of the control surface is reduced to zero. The dynamic pressure in the presence of control reversal is called the control reversal dynamic pressure, denoted by q_R. When the numerator of equation (22) is set as zero, we substitute equations (16) and (21) into equation (22) to obtain q_R, which is written as

$$q_R = \frac{DA_0^{-1}\left(W^T + UK_P^T\right)K_\theta}{2SD_0A_0^{-1}UK_P^TWA_0^{-1}W^T - 2SD_0A_0^{-1}W^TWA_0^{-1}UK_P^T}.$$
(23)

Besides, the efficiency of the control surface is defined as the ratio of the aerodynamic lift after aeroelastic deformation to that before aeroelastic deformation, as in

$$\eta = \frac{L_\theta}{L_0} = 1 + \frac{-2qsWA_0^{-1}W^T}{K + 2qsD_0A_0^{-1}W^T} \frac{D_0A_0^{-1}\left(UK_P^T + W^T\right)}{WA_0^{-1}\left(UK_P^T + W^T\right)}.$$
(24)

2.5. Aeroelastic Analysis Using Geometrically Exact VLM. The morphing piezoelectric wing balance equation using aerodynamic moments in equation (18) is defined as follows:

$$\bar{M} = K_\theta\theta.$$
(25)

It is worth noting that equation (25) is a nonlinear transcendental equation. In fact, equation (25) is an aeroelastic equation, whose nonlinearity appears in the process

of structural and aerodynamic coupling. Although VLM is a linear aerodynamic method, the relationship between aerodynamic moment and pitch angle θ obtained by the geometrically accurate VLM is not linear through the analysis in Section 2.4.

Through the following equations, we can obtain the pitch angle θ of the 2D wing in balance through an iterative solution, as in

$$\theta_{n+1} = \theta_n - \frac{\bar{M}(\theta_n) - K_\theta\theta_n}{(\partial\bar{M}/\partial\theta)|_{\theta=\theta_n} - K_\theta}.$$
(26)

There is some difference in the static aeroelastic stability of the 2D wing between the use of the geometrically exact VLM and traditional linearized VLM. Because unlike equation (19), equation (25) has multiple solutions in some conditions, which warrants analysis of the stability of each solution. According to the energy criterion [16], the 2D wing is in a stable equilibrium state when the variation of elastic potential energy is less than the variation of aerodynamic work in the presence of a slight disturbance. Besides, when the variation of elastic potential energy is equal to the variation of aerodynamic work in the presence of a slight disturbance, the system is in a critical equilibrium state while the corresponding aerodynamic load is a critical load.

Under a slight disturbance of the pitch angle $\delta\theta$, the variation of aerodynamic work can be defined as follows:

$$\Delta W_a = \int_{\theta^*}^{\theta^*+\delta\theta} \bar{M}(\theta)d\theta = \bar{M}(\theta^*)\delta\theta + \frac{\partial\bar{M}}{\partial\theta}\bigg|_{\theta=\theta^*}\theta^*\delta\theta + \frac{1}{2}\frac{\partial\bar{M}}{\partial\theta}\bigg|_{\theta=\theta^*}\delta\theta^2.$$

(27)

And the variation of spring elastic potential energy can be defined as

$$\Delta U = \frac{1}{2} K_\theta \delta\theta^2 + K_\theta \theta^* \delta\theta. \tag{28}$$

When $\Delta U = \Delta W_a$, the system is in neutral equilibrium. Applying equations (27) and (28) to it, the following simplified critical equilibrium state is reached:

$$\left.\frac{\partial \bar{M}}{\partial \theta}\right|_{\theta=\theta^*} = K_\theta. \tag{29}$$

Traditional aeroelastic analysis is based on linear aerodynamic theory. As a result, the critical equilibrium solution of the linear 2D wing system can be obtained as the divergence dynamic pressure. However, when using the geometrically exact VLM, the 2D wing system becomes nonlinear. Thus, it becomes inappropriate to discuss the divergence dynamic pressure of the nonlinear system. Instead, the number and stability of equilibrium solutions should be analyzed. Due to the complexity of solving equation (25), the numerical solution of the static aeroelastic stability of the piezoelectric wing is obtained for theoretical analysis instead of the analytical solution.

There is also some difference between the control surface efficiency of the 2D wing by the geometrically exact VLM and that by the traditional linearized VLM. Unlike the linear solution, the aerodynamic forces are related to the pitch angle θ and the trailing edge deflection angle β. Therefore, it is inappropriate to define control reversal dynamic pressure when aerodynamic lift reaches 0. Instead, the control reversal occurs when the lift decreases with the increase of β, and the corresponding dynamic pressure is called reverse dynamic pressure q_r which can be obtained by the following equation:

$$\left.\frac{\partial \bar{L}}{\partial U}\right|_{\theta=\theta^*} = 0. \tag{30}$$

Also, the control surface efficiency is defined similar to equation (22) as

$$\eta = \frac{\bar{L}}{\bar{L}_0}. \tag{31}$$

In this study, both equations (30) and (31) were solved by the nonlinear equation solution function of the MATLAB R2014a software.

3. Numerical Validation

In this paper, the piezoelectric constant d_{31} is always set to be $3.85 \times 10^{14} V \cdot m/N$ and all the structure parameters are listed in Table 1. The parameters of the piezoelectric patch are determined by real MFC.

In addition, the traditional wing with a rigid trailing edge is introduced to compare with the morphing piezoelectric wing. These two wings have the same chord length of control surface and the same vertical displacement of the trailing edge, as shown in Figure 3. Both the wings are considered to have the equivalent deflection angle, β.

3.1. Aerodynamic Characteristics of the Morphing Piezoelectric Wing. The aerodynamic loads of the morphing piezoelectric wing were calculated by both traditional linearized VLM and geometrically exact VLM. The lift coefficient and the moment coefficient with respect to the angle of attack are plotted in Figure 4. The angles of attack range from 0° to 12°. The torsion spring is set at 35% of chord-wise length and the control surface is 30% of chord. According to equation (8), the trailing edge of the morphing piezoelectric wing is deflected by 3.585 degrees per kilovolt.

It can be seen from Figure 4 that at the same angle of attack, the greater the driving voltage, the greater the aerodynamic force and the smaller the aerodynamic moment. The reason behind this is that a greater driving voltage creates a larger deflection of the trailing edge which leads to a bigger increment of angle of attack at the trailing edge, while the aerodynamic lift increased with the angle of attack. However, it shortens the mean aerodynamic chord of the wing, which makes the trailing edge deflect downward at greater driving voltage, resulting in the decrease of the aerodynamic moment. This conclusion is consistent with both traditional linearized VLM and geometrically exact VLM.

In addition, although the aerodynamic lifts and moments increase with the angle of attack, a slight difference exists between these two VLMs. For one thing, when the angle of attack α ranges from 0° to 6°, the aerodynamic coefficient calculated by the two VLMs are almost the same. In contrast, when α is above 6°, C_l and C_m calculated by the geometrically exact VLM are smaller than those calculated by the traditional linearized VLM. For another, with the increase of α and driving voltage, the differences between the two aerodynamic coefficients become larger, which is mainly attributed to the limitation of the traditional linearized VLM. When the 2D wing has a large angle of attack or a large trailing edge deflection angle, the boundary conditions cannot be linearized and the corresponding aerodynamic influence coefficient matrix cannot be considered as a constant matrix. As a result, the traditional linearized VLM is inapplicable for analyzing the aerodynamic characteristics of the 2D wing in this context. In contrast, the geometrically exact VLM exhibits considerable accuracy in calculating the aerodynamic coefficients at a large angle of attack and the trailing edge deflection angle. Results are consistent with the aerodynamic characteristics of the thin airfoil.

Consequently, a case is set to explore the influence of control surface length on aerodynamic coefficients. With the angle of attack kept as 0° and the equivalent deflection angle ($\beta = 7.17°$) of the different trailing edge unchanged, the starting location of the control surface was changed to calculate the aerodynamic coefficient. The results are shown in Figure 5.

Figure 5 shows that as the starting location of the control surface moves backward, the lift coefficient and moment coefficient caused by the trailing edge deflection decrease, which can be attributed to the lowered effective area of the

TABLE 1: Geometric parameters of the wing and the piezoelectric patch.

	Modulus of elasticity (Gpa)	Length (mm)	Width (mm)	Height (mm)
Rigid part of the wing	—	700	—	—
Elastic bending part of the wing	200	300	36	1.5
Piezoelectric patch	74	300	36	1

- - - Original airfoil

——— Morphing piezoelectric wing

-·-··· Traditional airfoil wing rigid trailing edge
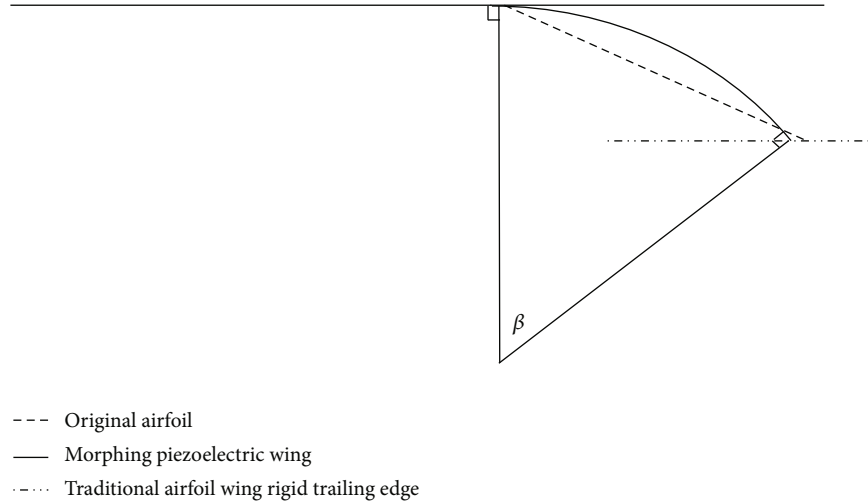
FIGURE 3: Wings with the equivalent deflection angle.

(a) Aerodynamic lift coefficient

(b) Aerodynamic moment coefficient
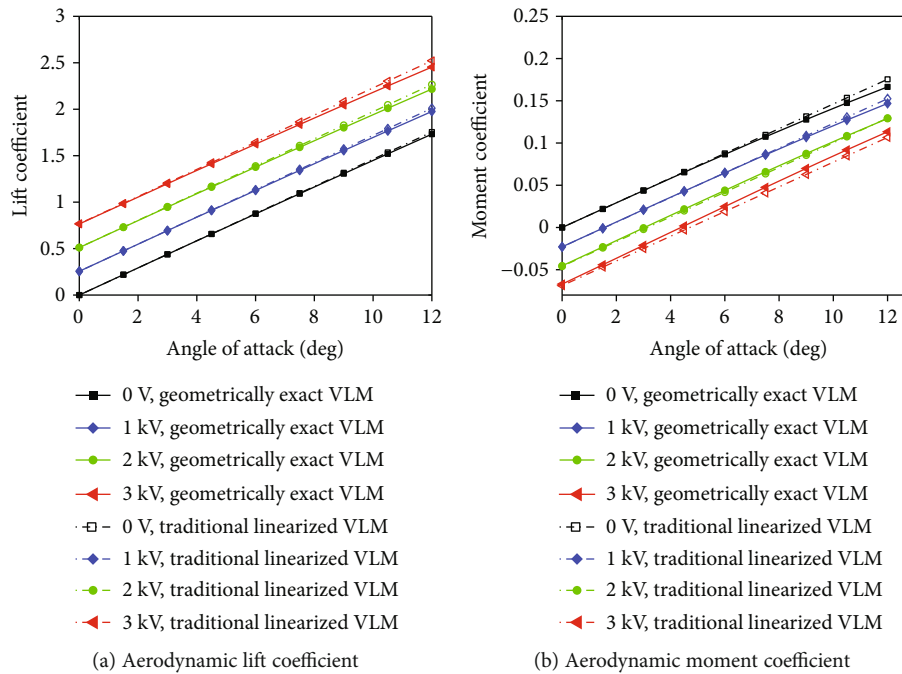
FIGURE 4: Effect of angle of attack and driving voltages on aerodynamic coefficient.

control surface. In addition, both C_l and C_m obtained by the geometrically exact VLM are smaller than those obtained by the traditional linearized VLM, which is consistent with the above conclusion. In Figure 5(a), the C_l of the morphing piezoelectric wing is higher than that of the wing with a rigid trailing edge. According to Figure 5(b), the aerodynamic moment of the morphing piezoelectric wing is higher than that of the traditional wing. Concurrently, the moment peaks when the starting location of control surface is around 70% chord. Besides, the C_m of the traditional wing with a rigid trailing edge airfoil decreases monotonically with the starting location going backward. It can be concluded that the

(a) Aerodynamic lift coefficient

(b) Aerodynamic moment coefficient
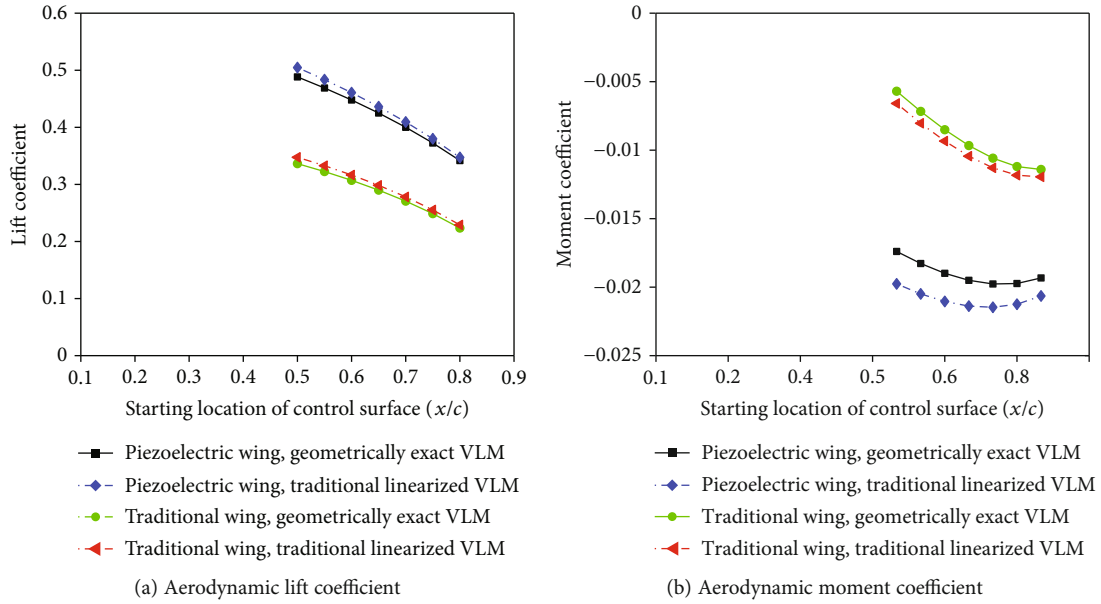
FIGURE 5: Effects of control surface length on aerodynamic coefficient.
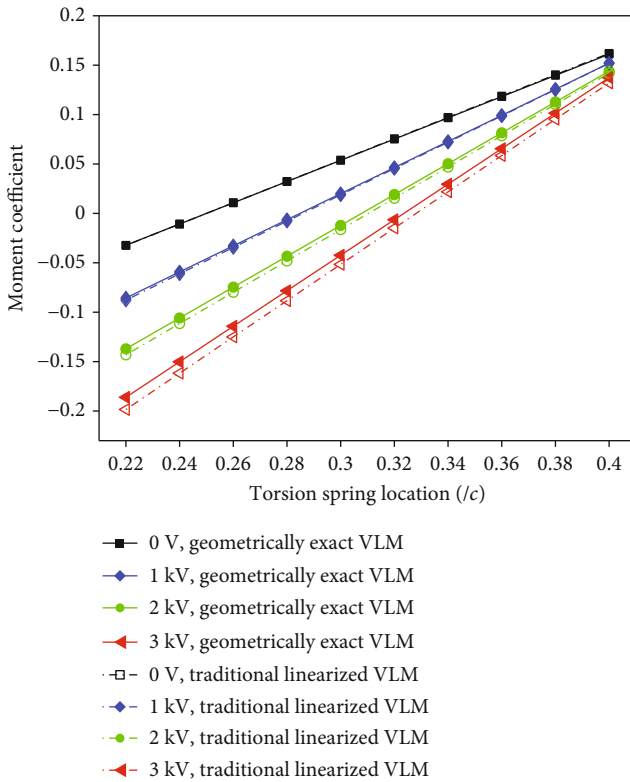
FIGURE 6: Effects of torsion spring location and driving voltages on aerodynamic moment.

morphing piezoelectric wing has a larger lift coefficient and a larger negative pitching moment coefficient than the traditional wing with the same trailing edge deflection.

The chord-wise location of the torsion spring also has an effect on the aerodynamic moment versus piezo actuation.

Another case is planned to research it. In this case, the two VLMs are used to calculate the aerodynamic moment of the morphing piezoelectric wing with different voltage and torsion spring locations at 5° angle of attack. The result is shown in Figure 6.

As Figure 6 illustrates, the aerodynamic moment increases as the torsion spring location moves backwards. Furthermore, the aerodynamic moment obtained by the geometrically exact VLM is larger than that obtained by the traditional linear VLM under the same driving voltages. This is because the geometrically exact VLM can fully consider the influence of the change of the downwash angle and aerodynamic arm caused by the wing deformation on the aerodynamic moment, while the traditional linear VLM ignores this point. It is worth noting that, the aerodynamic moments calculated by the two VLMs are the same at 0 driving voltage and the aerodynamic moments are 0 at the quarter-chord length. This can be interpreted that the camberline of the morphing piezoelectric wing is a straight line at 0 driving voltage whose aerodynamic center is also located at a quarter-chord length.

3.2. Aerodynamic Load Redistribution of Morphing TE Wing. In this section, different wings are considered and their properties are listed in Table 2 in order to investigate the effects of aeroelastic deformation on the changes of aerodynamic loads. The aerodynamic load redistribution is then plotted in Figure 7 and the overall lifts using the traditional linearized VLM or the geometrically exact VLM are listed in Table 3.

As shown in Figure 7(a), the airfoil without a control surface rotates upward under the current aerodynamic load resulting in an increase (3.2°) of the angle of attack. Thus, the overall aerodynamic lifts increase under an aeroelastic effect. Figure 7(b) shows the aerodynamic load distribution of the morphing piezoelectric wing. Due to the deflection of

TABLE 2: Properties of different airfoils.

	l_2 (/c)	l_0 (/c)	K_θ (N·m/rad)	q (Pa)	α (deg)	β (deg)
Airfoil without control surface	—	0.33	10	200	5	—
Morphing piezoelectric wing	0.3	0.33	10	200	5	10
Traditional wing with rigid trailing edge	0.3	0.33	10	200	5	10
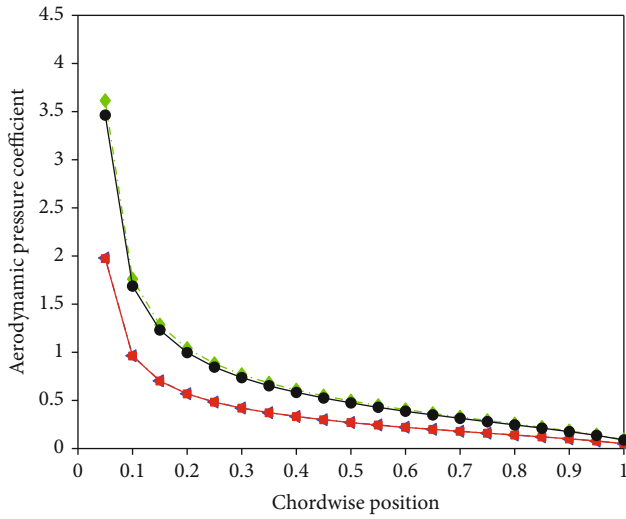
◄ Origin, traditional linearized VLM
◆ Aeroelastic deformation, traditional linearized VLM
■ Origin, geometrically exact VLM
● Aeroelastic deformation, geometrically exact VLM

(a) Traditional wing without control surface
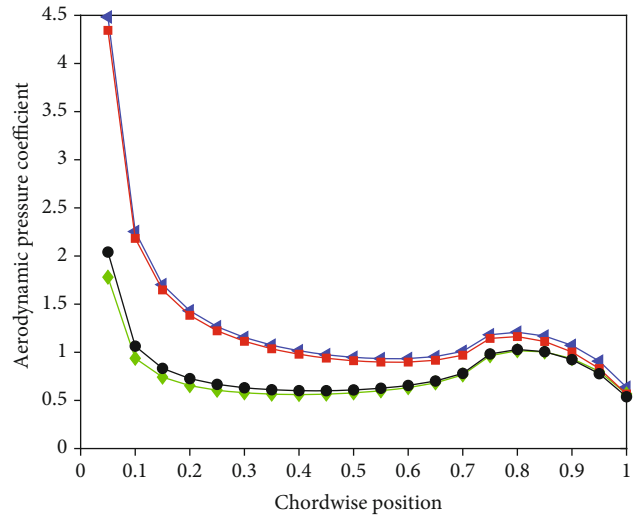
◄ Origin, traditional linearized VLM
◆ Aeroelastic deformation, traditional linearized VLM
■ Origin, geometrically exact VLM
● Aeroelastic deformation, geometrically exact VLM

(b) Morphing piezoelectric wing
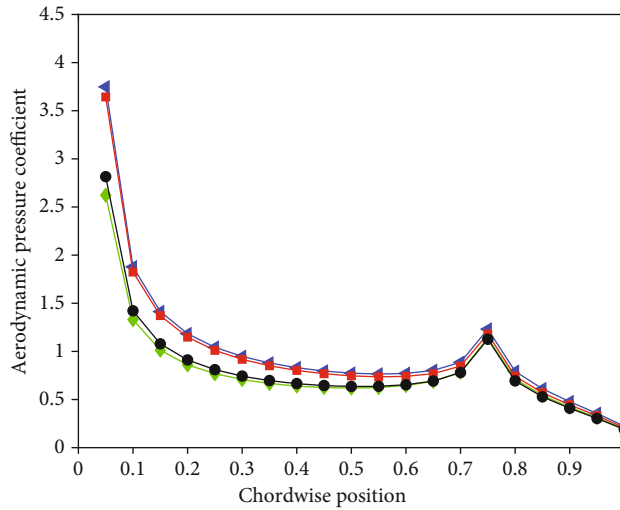
◄ Origin, traditional linearized VLM
◆ Aeroelastic deformation, traditional linearized VLM
■ Origin, geometrically exact VLM
● Aeroelastic deformation, geometrically exact VLM

(c) Traditional wing with rigid trailing edge

FIGURE 7: Aerodynamic load redistribution after aeroelastic deformation.

TABLE 3: Total aerodynamic lift.

	Airfoil without control surface	Morphing piezoelectric wing	Traditional wing with rigid trailing edge
Origin, traditional linearized VLM	3.5793	11.3167	9.9551
Origin, geometrically exact VLM	3.2547	10.8865	9.4613
Aeroelastic deformation, traditional linearized VLM	6.1865	8.5917	7.8819
Aeroelastic deformation, geometrically exact VLM	5.9250	8.9471	8.1935

the trailing edge, the aerodynamic load on the trailing edge is significantly increased. When it comes to the aeroelastic effect, the airfoil rotates downward under aerodynamic load, bringing about a decrease of overall aerodynamic lift. The reason is that when the trailing edge deflected downward, it generated a negative pitching moment which decreased the angle of attack. Figure 7(c) shows the aerodynamic load distribution of the traditional wing with a rigid trailing edge, in which the aerodynamic load sees a sudden change at the start point of the rigid trailing edge. This is because the additional angle of attack is noncontinuous when the trailing edge deflects downward, and the airfoil also rotated downward under aerodynamic load, as in Figure 7(b).

Table 3 indicates that with the same equivalent deflection angle ($\beta = 10°$), the lift coefficient of the morphing piezoelectric wing is higher than that of the traditional wing. Furthermore, aeroelastic deformation is demonstrated to significantly change the lift coefficient. Moreover, at the same trailing edge rotation angle, the negative pitching moment of the morphing piezoelectric wing is larger than that of the traditional wing. As a result, the C_l of the morphing piezoelectric wing declines to a larger extent than that of the traditional wing. Notably, the origin lift calculated by the geometrically exact VLM is 4% lower than the lift calculated by the traditional linearized VLM. This is because the induced velocity in the traditional linearized VLM is larger than that in the geometrically exact VLM. In contrast, the lift calculated by the geometrically exact VLM is larger than the lift calculated by the traditional linearized VLM as a result of aeroelastic deformation when the trailing edge deflected downward. This is because the aeroelastic pitch angle calculated by the geometrically exact VLM is smaller, which leads to a larger angle of attack in this case.

3.3. Static Aeroelastic Stability of Morphing TE Wing. In this section, some cases are set to reflect the influence of the angle of attack, trailing edge deflection angle, trailing edge deflection mode, and torsion axis location on the static aeroelastic stability of the morphing TE wing using the geometrically exact VLM. In this section, the parameters of the morphing piezoelectric wing and the traditional wing with a rigid trailing edge are set as the same as those in Section 3.2. The relationship between dynamic pressure and airfoil pitch angle θ of the piezoelectric morphing wing is obtained under different conditions, which are shown in Figure 8. In addition, q_{div} is the diverging dynamic pressure of the wing in the current state calculated by the traditional linear VLM. The x-axis of Figure 8 is the ratio of dynamic pressure to divergence

dynamic pressure q_{div} using the traditional linearized VLM, and the y-axis is the pitch angle θ. The solid lines represent stable solutions, while the dotted lines represent unstable solutions.

Figure 8(a) shows the equilibrium state of a 2D wing with a 0° angle of attack and a 0° trailing edge deflection angle. The solution of the equilibrium state is achieved by solving the nonlinear transcendental equation, as in equation (25). It can be seen that when the dynamic pressure is less than q_{div}, the equilibrium equation has only one stable solution. This indicates that the 2D wing is in static stability in this situation. Nevertheless, when dynamic pressure is greater than q_{div}, there are three solutions to the equilibrium with the same dynamic pressure: (1) a stable solution with a pitch angle of more than 0°; (2) a stable solution with a pitch angle of less than 0°; and (3) an unstable solution with a pitch angle of 0°. This is a typical static bifurcation of a nonlinear system and is part of pitchfork bifurcation. The bifurcation value is q_{div}. This indicates that the zero solution of the nonlinear 2D wing system is consistent with the linear condition. The final position of the 2D wing depends on the disturbance.

Figures 8(b)–8(d) show the equilibrium states of the 2D wing with varying angles of attack and 0° trailing edge deflection angle. In the case of Figure 8(b), the angle of attack is set as 1°. Figure 8(b) shows that only when the dynamic pressure is less than q_{div} can the system achieve a stable equilibrium solution with a positive pitch angle. When the dynamic pressure exceeds q_{div}, saddle knot bifurcation occurs in the system. In this context, there are three solutions when the original equilibrium solution maintains nonlinear development. There are two new equilibrium solutions with a negative pitch angle. The one with a smaller pitch angle is unstable and is referred to as saddle point, while the other is stable and is referred to as stable knot. In addition, the bifurcation value is 1.115 q_{div}. In the case of Figure 8(c), the angle of attack is set as 5°. Figure 8(c) shares the same topology with Figure 8(b). But its bifurcation value is 1.3563 q_{div}. In the case of Figure 8(d), the angle of attack is set as -1°. Figures 8(d) and 8(b) are mirror images of the x-axis and share the same bifurcation value. It can be concluded that by means of the geometrically exact VLM, the angle of attack has a great impact on the static stability of the 2D wing, which is mainly embodied in three aspects. Firstly, a nonzero angle of attack changes the type of bifurcation diagram of the system. Secondly, the bifurcation value increases along with the increase of the angle of attack. Thirdly, the sign of the angle of attack is independent of the bifurcation value.

(a)

(b)

(c)

(d)

(e)

(f)
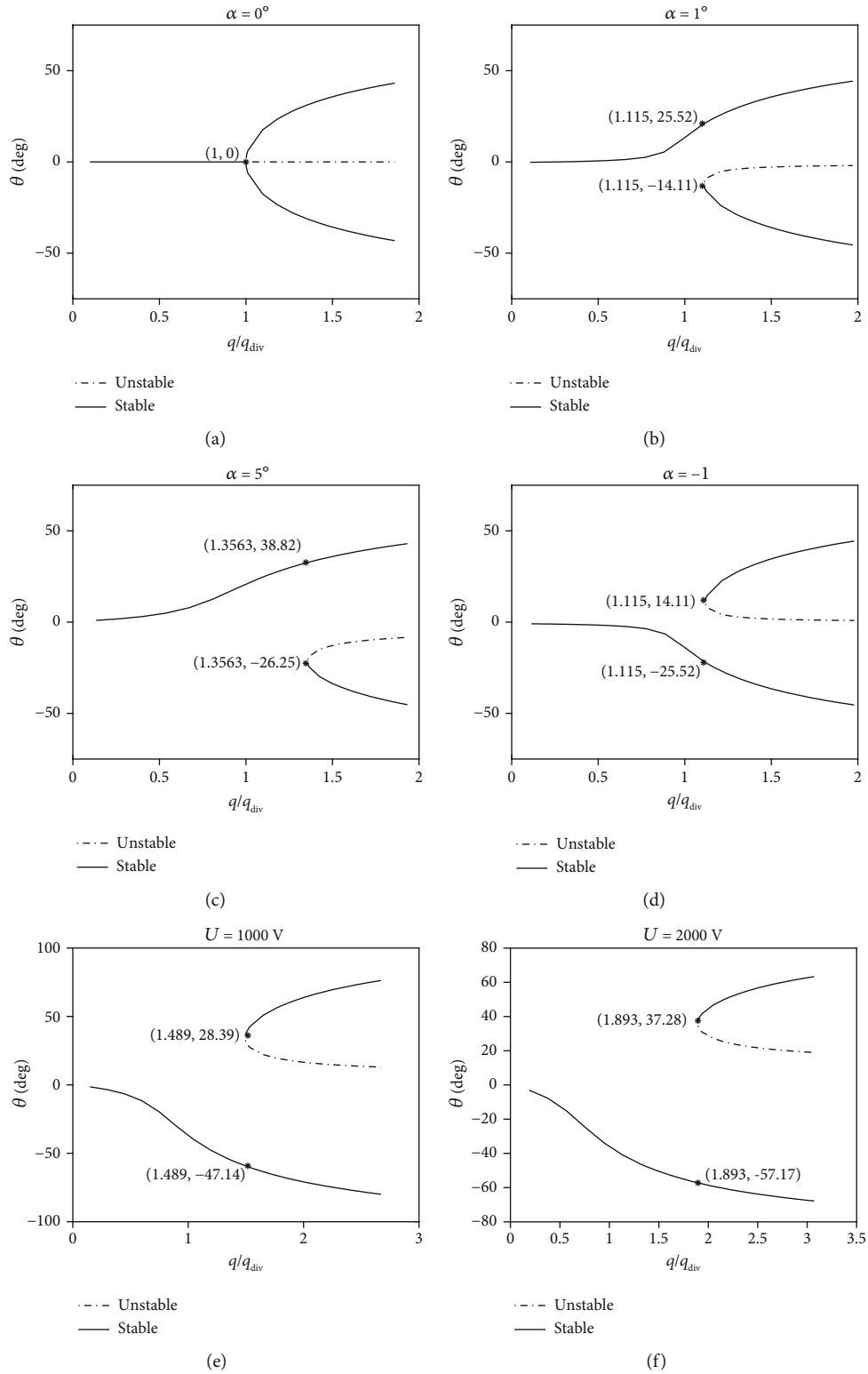
FIGURE 8: Continued.
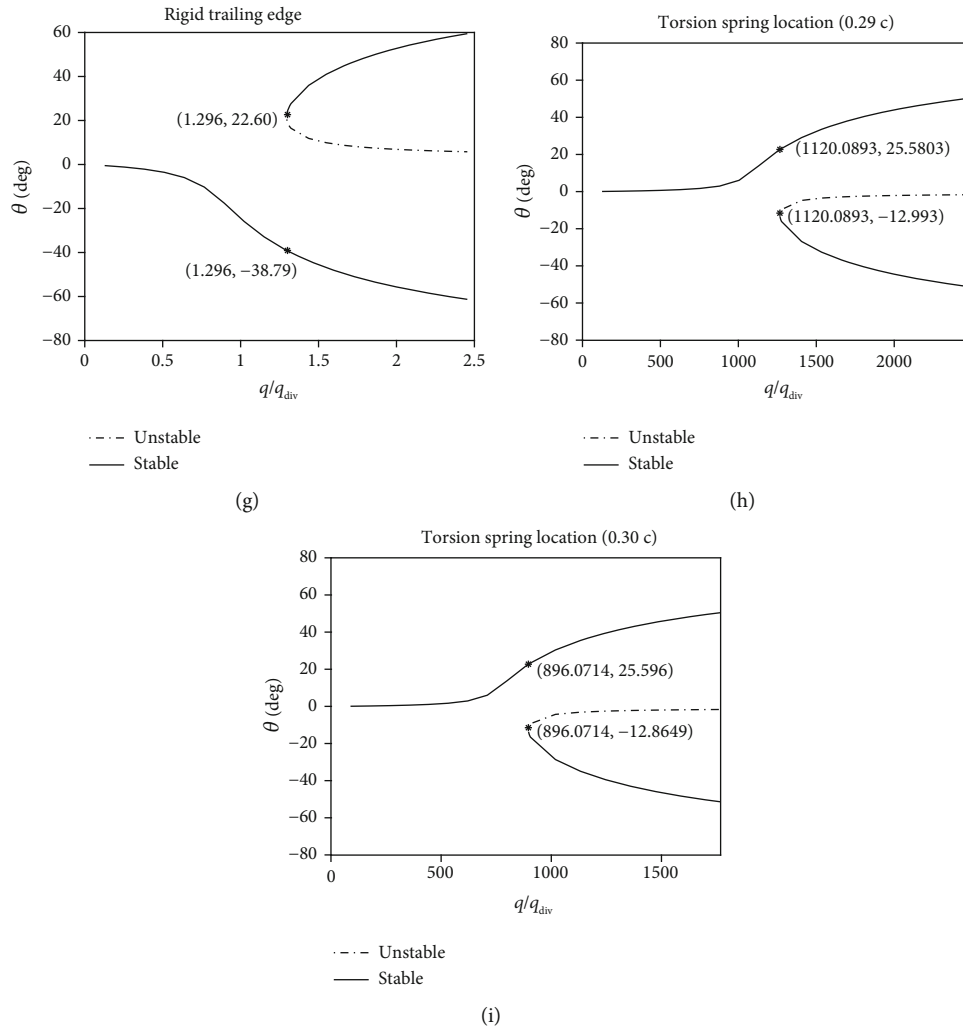
FIGURE 8: Relationship between dynamic pressure and pitch angle θ in equilibrium state using the geometrically exact VLM.

Figure 8(e) shows the equilibrium state of the morphing piezoelectric wing with a 0° angle of attack and a 1000 V piezoelectric voltage which generates a 4.88° trailing edge deflection angle. It can be seen that the topology of the bifurcation diagram is the same as the one with a negative angle of attack. Meanwhile, the bifurcation value is 1.489 q_{div}. Figure 8(f) shows the equilibrium state of the morphing piezoelectric wing with a 0° angle of attack and a 2000 V piezoelectric voltage which generates a 9.76° trailing edge deflection angle. Likewise, the topology of the bifurcation diagram is the same as that of Figure 8(e) but the bifurcation value increases to 1.893 q_{div}. It can be concluded that the bifurcation value increases along with the trailing edge deflection angle. This can be attributed to the fact that the trailing edge deflection downward causes a negative pitching moment on the 2D wing, which is similar to the wing with a negative angle of attack. Figure 8(g) shows the equilibrium state of the traditional wing with a rigid trailing edge with a 0° angle of attack and a 4.88° trailing edge deflection angle. The topology of Figure 8(g) is the same as that of Figure 8(e), but the bifurcation value is reduced to 1.296 q_{div}. It can be concluded that bifurcation value increases along with the trailing edge

deflection angle. Furthermore, the traditional wing with a rigid trailing edge has a smaller bifurcation value than the morphing piezoelectric wing with the same trailing edge deflection angle. This is because the morphing piezoelectric wing generates a larger negative pitching moment than the traditional wing. Similar to the previous conclusion, the morphing piezoelectric wing has a larger equivalent angle of attack which leads to a higher bifurcation value.

Figures 8(h) and 8(i) show the equilibrium states of the morphing piezoelectric wing with a 1° angle of attack and a 1000 V driving voltage at different torsion spring locations, 29% chord length (0.29c), and 30% chord length (0.3c). Figures 8(h) and 8(i) have the same topology of the bifurcation diagram which is similar to Figure 8(b) but with different bifurcation value. The bifurcation value (1120.09 Pa) in Figure 8(h) is larger than that (896.07 Pa) in Figure 8(i). This is because in the case of Figure 8(h), the torsion spring location is closer to the aerodynamic center which leads to a smaller aerodynamic arm. Under the same aerodynamic load, a small aerodynamic arm means a small aerodynamic moment, which makes the system difficult to bifurcate. Therefore, a reasonable arrangement of the torsion axis

(a) Angle of attack vs. control reversal dynamic pressure

(b) Torsion spring stiffness vs. control reversal dynamic pressure

FIGURE 9: Factors related to the control reversal dynamic pressure.

location can significantly improve the bifurcation value by reducing the aerodynamic arm of the wing.

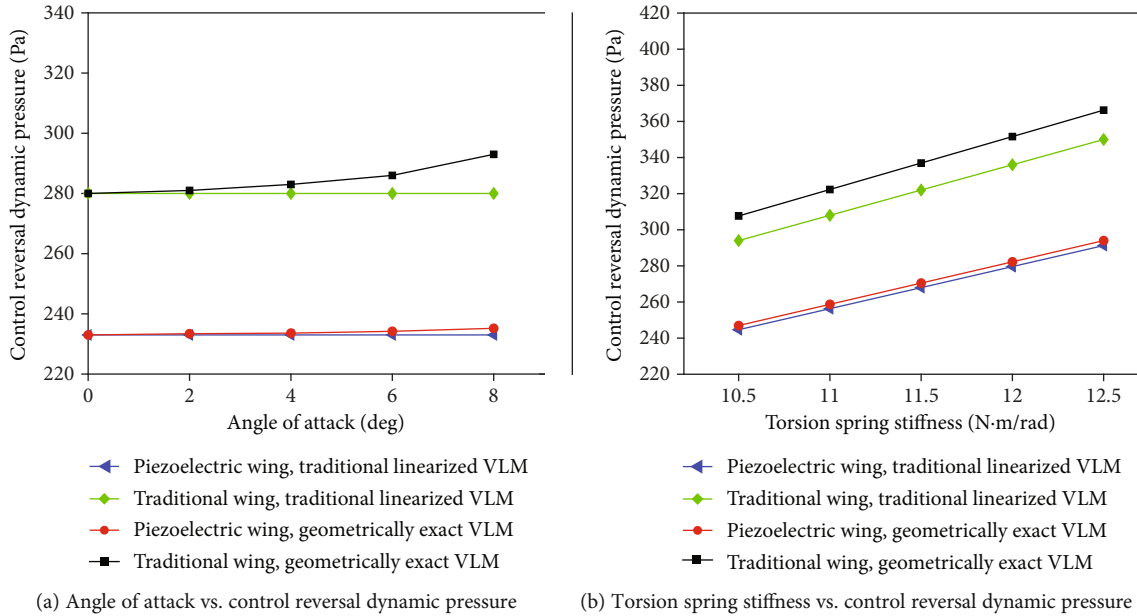In the numerical validation, it can be seen that there is always a solution in equation (25), indicating that there is no divergent dynamic pressure of the 2D wing using the geometrically exact VLM. This can be attributed to the fact that the aerodynamic moments cannot keep increasing with the pitch angle due to the decrease of the aerodynamic arm. But this does not mean that the wing can sustain a gigantic dynamic pressure since the wing has strength constraints and may be destroyed before it reaches equilibrium.

3.4. Control Reversal Dynamic Pressure of Morphing TE Wing. In this section, some cases with different angles of attack and torsion spring stiffness are set to identify the factors related to the control reversal dynamic pressure. The results are given in Figure 8. In this section, the parameters of the morphing piezoelectric wing and the traditional wing with a rigid trailing edge are set the same as those in the Section 3.2.

Figure 9(a) shows the effect of the angle of attack on the control reversal dynamic pressure. In Figure 9(a), it can be seen that the control reversal dynamic pressure calculated by the traditional linearized VLM is not related to the angle of attack, while the control reversal dynamic pressure calculated by the geometrically exact VLM increases with the angle of attack. The q_R of the traditional wing is 21% larger than that of the morphing piezoelectric wing, since the traditional wing has a lower negative pitching moment and a lighter impact on aeroelastic deformation than the morphing piezoelectric wing. Figure 9(b) illustrates that q_R increases along with the increase of the pitch stiffness of the airfoil. This is due to the fact that high pitching stiffness of the airfoil leads to smaller aeroelastic deformation in the same aerodynamic load, which results in higher control reversal dynamic pressure.

4. Conclusion

Morphing trailing-edge wings, which can change their shape during flights, have the potential to improve the aerodynamic characteristics of aircraft, which warrants aeroelastic analysis for the morphing TE wings. Committed to the static aeroelastic characteristics of the morphing TE wings, this paper has developed a static aeroelastic analysis method using the geometrically exact VLM which gives equal prominence to both efficiency and medium accuracy. Firstly, the morphing piezoelectric wing was chosen and analyzed as a typical and simple model for morphing TE wings, and the relationship between piezoelectric voltage and trailing-edge deflection was tested. Then, the paper has established a set of cases for aeroelastic analysis of morphing TE wings using the geometrically exact VLM and shed light on their nonlinear aeroelastic characteristics. Finally, a series of simulations with different aerodynamic conditions were carried out on both the morphing piezoelectric wing and the wing with a rigid trailing edge. This paper has only explored the mechanism of the morphing TE wing without achieving any precise and detailed design. Based on the existing calculation results, some important conclusions can be summarized as follows:

(1) This paper has demonstrated the influence of aerodynamic nonlinearity on the static stability of the 2D wing system using the geometrically exact VLM. The system does not show divergence but bifurcation. Besides, the angle of attack, trailing-edge deflection angle, trailing-edge deflection mode, and torsion axis location all affect the bifurcation value and topology of the bifurcation diagram. Although this conclusion is conditional due to the limitation of the geometrically exact VLM, a general conclusion can be attained

(2) The characteristics of this method are verified by numerical examples. The geometrically exact VLM is more accurate than the traditional linearized VLM in calculating aerodynamic forces of a 2D wing with control surface in aeroelastic analysis. The influences of angle of attack, trailing-edge deflection angle, among others on static aeroelastic characteristics are taken into consideration, which play a significant role in engineering

(3) A morphing wing is inarguably a fluid-solid and control coupling system. As a result, by taking aerodynamic, structure, and control coupling into account, the method used in this paper can serve as an effective basic tool for morphing wing analysis and design optimization owing to its accuracy, adequate calculation, and inheritability of traditional methods

Data Availability

The data used to support the findings of this study are available from the corresponding author upon request.

Conflicts of Interest

The authors declare that there is no conflict of interest regarding the publication of this paper.

References

[1] S. Barbarino, O. Bilgen, R. M. Ajaj, M. I. Friswell, and D. J. Inman, "A review of morphing aircraft," *Journal of Intelligent Material Systems and Structures*, vol. 22, no. 9, pp. 823–877, 2011.

[2] S. Kota, J. A. Hetrick, R. Osborn et al., "Design and application of compliant mechanisms for morphing aircraft structures," in *Smart Structures and Materials 2003: Industrial and Commercial Applications of Smart Structures Technologies*, pp. 24–34, San Diego, CA, USA, 2003.

[3] P. Boschetti, A. Amerio, and E. Cárdenas, "Aerodynamic performance as a function of local twist in an unmanned airplane," in *47th AIAA Aerospace Sciences Meeting including The New Horizons Forum and Aerospace Exposition*, p. 1481, Orlando, FL, USA, 2009.

[4] V. Wickramasinghe, Y. Chen, M. Martinez, F. Wong, and R. Kernaghan, "Design and verification of a smart wing for an extremely-agile micro-air-vehicle," in *50th AIAA/ASME/ASCE/AHS/ASC Structures, Structural Dynamics, and Materials Conference*, p. 2132, Palm Springs, CA, USA, 2009.

[5] O. Bilgen, K. B. Kochersberger, D. J. Inman, and O. J. Ohanian III, "Novel, bidirectional, variable-camber airfoil via macro-fiber composite actuators," *Journal of Aircraft*, vol. 47, no. 1, pp. 303–314, 2010.

[6] H. Monner, J. Riemenschneider, S. Opitz, and M. Schulz, "Development of active twist rotors at the German Aerospace Center (DLR)," in *52nd AIAA/ASME/ASCE/AHS/ASC Structures, Structural Dynamics and Materials Conference*, p. 1824, Denver, CO, USA, 2011.

[7] A. Pankonien and D. J. Inman, "Experimental testing of spanwise morphing trailing edge concept," in *Active and Passive Smart Structures and Integrated Systems 2013*, p. 868815, San Diego, California, USA, 2013.

[8] O. J. Ohanian, C. Hickling, B. Stiltner et al., "Piezoelectric morphing versus servo-actuated MAV control surfaces," in *53rd AIAA/ASME/ASCE/AHS/ASC Structures, Structural Dynamics and Materials Conference*, p. 1512, Honolulu, Hawaii, 2012.

[9] O. J. Ohanian, B. David, S. Taylor et al., "Piezoelectric morphing versus servo-actuated MAV control surfaces, part II: flight testing," in *51st AIAA Aerospace Sciences Meeting including the New Horizons Forum and Aerospace Exposition*, p. 0767, Dallas, TX, USA, 2013.

[10] K. B. Kochersberger, O. J. Ohanian III, T. Probst, and P. A. Gelhausen, "Design and flight test of the generic micro-aerial vehicle (GenMAV) utilizing piezoelectric conformal flight control actuation," *Journal of Intelligent Material Systems and Structures*, vol. 28, no. 19, pp. 2793–2809, 2017.

[11] D. Li, S. Guo, and J. Xiang, "Modeling and nonlinear aeroelastic analysis of a wing with morphing trailing edge," *Proceedings of the Institution of Mechanical Engineers, Part G: Journal of Aerospace Engineering*, vol. 227, no. 4, pp. 619–631, 2013.

[12] B. K. Stanford and P. S. Beran, "Analytical sensitivity analysis of an unsteady vortex-lattice method for flapping-wing optimization," *Journal of Aircraft*, vol. 47, no. 2, pp. 647–662, 2010.

[13] C. Xie, L. Wang, C. Yang, and Y. Liu, "Static aeroelastic analysis of very flexible wings based on non-planar vortex lattice method," *Chinese Journal of Aeronautics*, vol. 26, no. 3, pp. 514–521, 2013.

[14] R. L. Clark, M. R. Flemming, and C. R. Fuller, "Piezoelectric actuators for distributed vibration excitation of thin plates: a comparison between theory and experiment," *Journal of vibration and acoustics*, vol. 115, no. 3, pp. 332–339, 1993.

[15] J. Katz and A. Plotkin, *Low-Speed Aerodynamics, vol. 13*, Cambridge University Press, 2001.

[16] R. E. Melchers and A. T. Beck, *Structural Reliability Analysis and Prediction*, John Wiley & Sons, 2017.

Research Article

Visual Inspection of the Aircraft Surface Using a Teleoperated Reconfigurable Climbing Robot and Enhanced Deep Learning Technique

Balakrishnan Ramalingam [iD],[1] **Vega-Heredia Manuel,**[1,2] **Mohan Rajesh Elara** [iD],[1]
Ayyalusami Vengadesh,[1] **Anirudh Krishna Lakshmanan,**[1,3] **Muhammad Ilyas** [iD],[1,4]
and Tan Jun Yuan James[5]

[1]*Singapore University of Technology and Design, Singapore 487372*
[2]*Department of Engineering and Technology, Universidad de Occidente, Campus Los Mochis, 81223, Mexico*
[3]*Department of Computer Science, Birla Institute of Technology and Science (BITS) Pilani, Pilani Campus, 333031, Vidyavihar, Rajasthan, India*
[4]*Department of Electrical Engineering, UET Lahore, NWL Campus 54890, Pakistan*
[5]*ST Engineering Aerospace, ST Engineering, Singapore 539938*

Correspondence should be addressed to Mohan Rajesh Elara; rajeshelara@sutd.edu.sg

Aircraft surface inspection includes detecting surface defects caused by corrosion and cracks and stains from the oil spill, grease, dirt sediments, etc. In the conventional aircraft surface inspection process, human visual inspection is performed which is time-consuming and inefficient whereas robots with onboard vision systems can inspect the aircraft skin safely, quickly, and accurately. This work proposes an aircraft surface defect and stain detection model using a reconfigurable climbing robot and an enhanced deep learning algorithm. A reconfigurable, teleoperated robot, named as "Kiropter," is designed to capture the aircraft surface images with an onboard RGB camera. An enhanced SSD MobileNet framework is proposed for stain and defect detection from these images. A Self-filtering-based periodic pattern detection filter has been included in the SSD MobileNet deep learning framework to achieve the enhanced detection of the stains and defects on the aircraft skin images. The model has been tested with real aircraft surface images acquired from a Boeing 737 and a compact aircraft's surface using the teleoperated robot. The experimental results prove that the enhanced SSD MobileNet framework achieves improved detection accuracy of aircraft surface defects and stains as compared to the conventional models.

1. Introduction

Aircraft skin inspection is essential under the Corrosion Prevention and Control Program (CPCP) to ensure the aircraft structural integrity [1]. Under CPCP, the aircraft should be kept thoroughly clean of deposits containing contaminating substances such as oil, grease, dirt, and other organic or foreign materials to prevent the aircraft from the potential risk of corrosion, degradation of seals, and plastic components. Furthermore, after scheduled cleaning of the aircraft, it should be thoroughly inspected to identify uncleaned areas

(typically stains) and surface defects. During cleaning, the cleaning agent may build upon these defects, which can increase the damage caused [1, 2].

Human visual inspection is, by far, the most widely used method in aircraft surface inspection [3, 4] as per CPCP. However, the current practice of getting on the aircraft body in order to carry out surface inspection raises safety issues for the inspectors. It is also time-consuming and suffers at times from being ineffective due to inspector fatigue or boredom. Automated aircraft skin inspection systems based on computer vision techniques could allow the inspector to safely,

quickly, and accurately perform the necessary visual inspection [3, 5, 6]. Robotic assistance for inspection of the aircraft skin has been investigated in [4, 7–9]. These systems need a flexible teleoperated robotic platform with different locomotion capabilities to access the aircraft surface and an optimal detection algorithm for automatically detecting stains and defects on the aircraft skin.

Designing a robotic inspection platform with good adherence, mobility, and flexibility is a key challenge. Typically, fixed morphology climbing robots are used for aircraft inspection. They use magnetic devices, vacuum suction cups, or propeller force to adhere and climb the aircraft surface [8, 10–12]. However, these climbing robots face difficulties when accessing confined areas due to their less flexible design [8, 9, 13]. They also find it hard to climb overlapped joints and fuselage, thereby reducing their coverage [9]. Reconfigurable robotic platforms can access confined spaces, rough terrains, and hard to navigate surfaces through dynamically changing their shape and functionality. Recently, the reconfigurable robotic platform has been widely developed and deployed in the various applications including inspection [14, 15], repairs [16], cleaning [17, 18], and space applications [19]. Kwon et al. [20] developed a reconfigurable robot for inspection of in-house pipelines and sewage pipeline inspection. In [14], authors have developed a reconfigurable robot for bridge inspection. Tromino and tetrominoes tiling algorithm-based reconfigurable shape-changing robots have also been developed for floor cleaning [21, 22]. The floor cleaning robot achieve better floor area coverage than fixed morphology robots.

Another constraint for the aircraft visual inspection technique is developing detection algorithm to recognize the stains and defects automatically. In the last decade, various visual inspection algorithms have been applied to the field of aircraft inspection and surface defect detection. These visual inspection algorithms are classified into two types, such as traditional image processing-based visual inspection [5, 23–25] and machine learning techniques [26–31]. Typically, the traditional algorithms use rudimentary characteristics like edges, brightness, histogram, and spectral feature to detect and segment defects [28]. However, these image processing methods work well only in controlled environments and often fail in complex real-world scenarios due to noise and complex backgrounds. Moreover, for various defects, thresholds often used in these algorithms need to be adjusted or it may even be necessary to redesign the algorithms [28]. CNN-based algorithms have been successfully implemented in defect detection and inspection applications including surface crack and defect detection [26–28, 30, 32], solar panel inspection [33], and cleaning inspection [34]. Cha and Choi proposed the use of CNNs [32] and Faster RCNN method [29] for better crack detection in concrete and metal surfaces. The author suggests the use of Faster RCNN, which has a more optimized bounding box for crack localization. Further, the author also proposes an UAV system for tagging and localization of concrete cracks [35, 36].

Typically, the key challenge of deep learning algorithms for this application is the requirement of a large amount of image data and an optimal preprocessing algorithm. Preprocessing plays a vital role in helping the network in recognizing the low-contrast objects and differentiating between objects with similar features, such as dirt, stains, and scratches on the aircraft surface, all at a small cost, which is negligible compared to increasing the complexity of the CNN architecture [26]. Li et al. included the preprocessing algorithm with SSD MobileNet in surface defect detection application. Here, the authors use Gaussian filtering, edge detection, and circle Hough detection algorithms to enhance the edge quality and filter out the noise from the image [26]. In [37], edge information for improving the Faster RCNN detection accuracy in traffic sign detection application was used. The author proved that the edge information has improved the detection accuracy and recall rate of Faster RCNN. Brendel and Bethge developed a CNN model named as BagNets which uses a local image feature to achieve a better detection ratio and good feature sensitivity [38]. In [28], Tao et al. prove that their compact CNNs have achieve better detection in the texture-based trained network than the content image.

In order to overcome the shortcomings mentioned earlier, this paper proposes a reconfigurable suction-based robot named as "Kiropter" for aircraft inspection along with an enhanced SSD MobileNet deep learning framework for recognizing and classifying the stains and defects on the aircraft surface. The reconfigurable robot is capable of accessing confined areas, overlapped joints, and fuselage on the aircraft body by dynamically changing its shape and functionality. The self-filtering-based periodic pattern detection filter is adopted as with the SSD MobileNet deep learning framework to effectively enhance the recognition results in low-contrast stain and defective areas in the aircraft skin image. This article is organized as follows: related work is reported in Section 2. Section 3 describes the robotic architecture and functionality. The enhanced deep learning-based inspection model is described in Section 4. The experimental results are given in Section 5. Finally, conclusions and future work are provided in Section 6.

2. Related Research Work

Very few works on aircraft skin inspection exist in the literature. Few of these works focus on developing a robotic platform for inspection and others focused on the detection algorithm. Siegel and Gunatilake [39] developed an aircraft surface inspection model based on the crown inspection mobile platform (CIMP) which captures images of the aircraft body and employs a computer-aided visual inspection algorithm for recognizing defects on the surface. The visual algorithm comprises of the wavelet-based image enhancement scheme to highlight the cracks and three-layered feedforward neural network consisting of ten inputs, thirty hidden layers, and two outputs to classify the cracks and corrosion. Enhanced remote visual inspection of the aircraft skin based on the CIMP robot system using an improved NN algorithm is proposed by Alberts et al. [40]. Here, the author designs a three-layer network (input, hidden, and output layers) with 169 input node-based NN for differentiating healthy and cracked areas of the aircraft surface. Automated

aircraft visual inspection is reported by Rice et al. [24], where the authors use the depth camera fitted on the roof to scan the aircraft surface. This is followed by a contour fitting algorithm to visualize the defects present on the aircraft. Mumtaz et al. [23] examined three image processing algorithms to differentiate between cracks and scratches on the aircraft skin. The authors tested the neural network, contourlet transform (CT) with a dot product classifier (DPC), and discrete cosine transform (DCT) with DPC and the combination of DCT and CT with DPC. Among the three DCT, CT with DPC combined schemes achieves a higher recognition rate. Jovaňcevíc et al. [5] developed an automated aircraft exterior inspection model for the autonomous mobile collaborative robot (cobot) using 2D image processing methods. The authors use a 5×5 kernel mask to remove the noise and enhance the texture on aircraft surface regions. The Hough transform (HT) and edge detection circle (EDC) algorithms are used to extract the geometrical shapes of objects on the aircraft surface (oxygen bay, radome latch, air inlet vent, engine, and pitot probe), and a CAD model is used to inspect the state change. Shang et al. [41] developed a climbing robot for aircraft wing and fuselage inspection. The developed model was designed for accomplishing the various nondestructive testing including eddy current inspection for surface cracks and subsurface corrosion and thermographic inspection to detect loose rivets. In [9], a snake-arm robot system is developed for aircraft Remote Access Nondestructive Evaluation (RANDE). The robot can reach into tight spaces in aircraft wings and perform crack and defect inspection. Aircraft inspection with the reconfigurable robot and enhanced deep learning scheme is a novel approach and has lots of potential in research.

3. Proposed Method

The functional block diagram of the proposed visual inspection model is shown in Figure 1. It comprises of an inspection robot (Kiropter) and the enhanced inspection algorithm. This section first describes the structure and hardware of the robot followed by the algorithm used for stain and defect detection.

3.1. General Overview. The Kiropter is a semiautonomous teleoperated differential 8W 2D robotic platform as shown in Figure 1. This mobile robot is capable of navigating around the surface of the aircraft by utilizing its reconfigurable nature. It is built on polylactic acid material (PLA) for the structure, acrylic of 5 mm for the base, and thermoplastic polyurethane (TPU) for the electric ducted fan (EDF) holders. The platform is 450 mm long and 200 mm wide and approximately 2.21 kg in total weight. The wheels are made up of soft and high-friction rubber for increasing of the traction on the airplane surface during locomotion. The robot is powered with 11.1 V, 42000 mAh 45 cc LIPO batteries parallelly connected to the units.

3.2. Hardware Architecture. Figure 2 shows the hardware architecture of the Kiropter robot. It comprises of four functional units including the central control unit (CCU), loco-

motive system, EDF system, and vision system. The robot communicates wirelessly and can be controlled through a graphical user interface (GUI). The functional description of each unit is described as follows.

3.3. Central Control Unit. The central control unit (CCU) is powered with an Arduino Mega 2560 microcontroller. It handles the wireless communication interface and generates the required control signals to the locomotion unit and shape changing unit according to the control flow chart as shown in Figure 3.

3.4. Locomotive System. Locomotion of the Kiropter robot has been achieved through three functions including adhesion, rolling, and transformation. Electric turbines are used for adhesion, and servomotors are used for navigation around the surface of the aircraft and for transformation. Electric turbines are controlled from the CCU through the HV75A brushless motor controller. The CCU generates the required PWM signal to the driving unit (HV75A) for adjustment of the turbine speed. For transformation, the servomotor is placed in the central articulation of the robot. It has a torque of 1.5 Nm and is controlled asynchronously through the CCU. Through servomotors, the robot can reconfigure its shape to different angles: 0°, 90° (on orthogonal surfaces), 45°, −5°, and −7° (Figure 4). This enables it to move on difficult surfaces for traversal, specifically between the aircraft wing and the body through the curvature of the aircraft surface. In that way, the robot keeps its wheels in contact with the surface, which is critical for the stability of the platform. The position of the robot can be estimated considering the feedback of the angular position of the servomotors of the wheels and the angular position of the central joint. In addition, a wheel encoder and two inertial measurement unit (IMU) sensors are fixed in the front and rear ends of the robot to estimate the robot position and orientation on the airplane structure. Through wheel encoders and IMU sensor data, the stain position and orientation information has been estimated in the inspection stage.

3.5. Electric Ducted Fan (EDF) System. An EDF is an impeller driven by a brushless motor mounted inside a circular duct. It has a thrust holding 3.5 kg. The EDF receives its power directly from the batteries. The speed of the EDF and the energy used are controlled by changing the pulses from the CCU independently for each EDF using the electronic speed control (ESC) (Figure 5). Through the EDF system, the robot is able to hold on and inspect the curvature and lower surface of the airplanes.

3.6. Vision System. The vision system consists of a WiFi-enabled HD 1080 p camera (HDDB 10AD). The camera is placed 72 mm above the surface of the plane, in the center of the body of the robot. The camera is inclined at an angle α of 30° from the x-y plane of the robot (Figures 6 and 7), so it is estimated that the center of the camera at the height of 72 mm has a range of ≈460 mm on flat surfaces. The opening angle of the camera is 60°. So, the point of vision starts at ≈23 mm from the robot in the x-y plane.
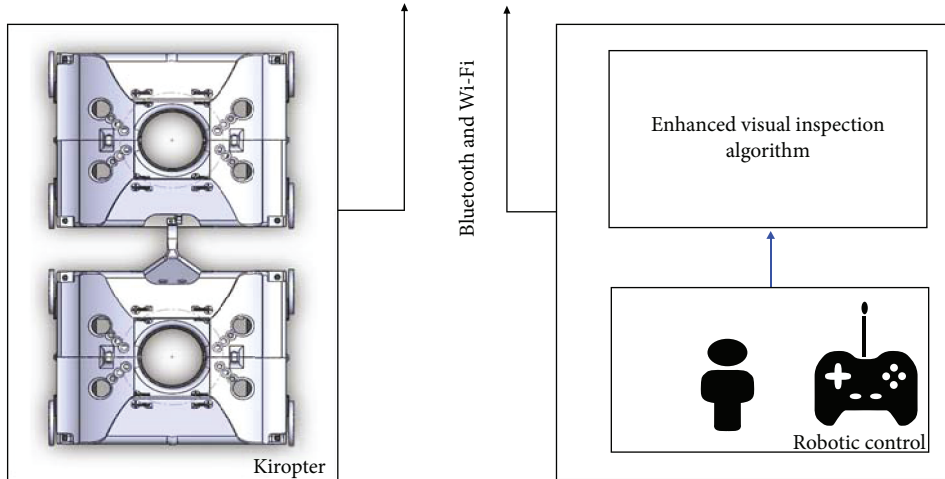
FIGURE 1: Proposed scheme.
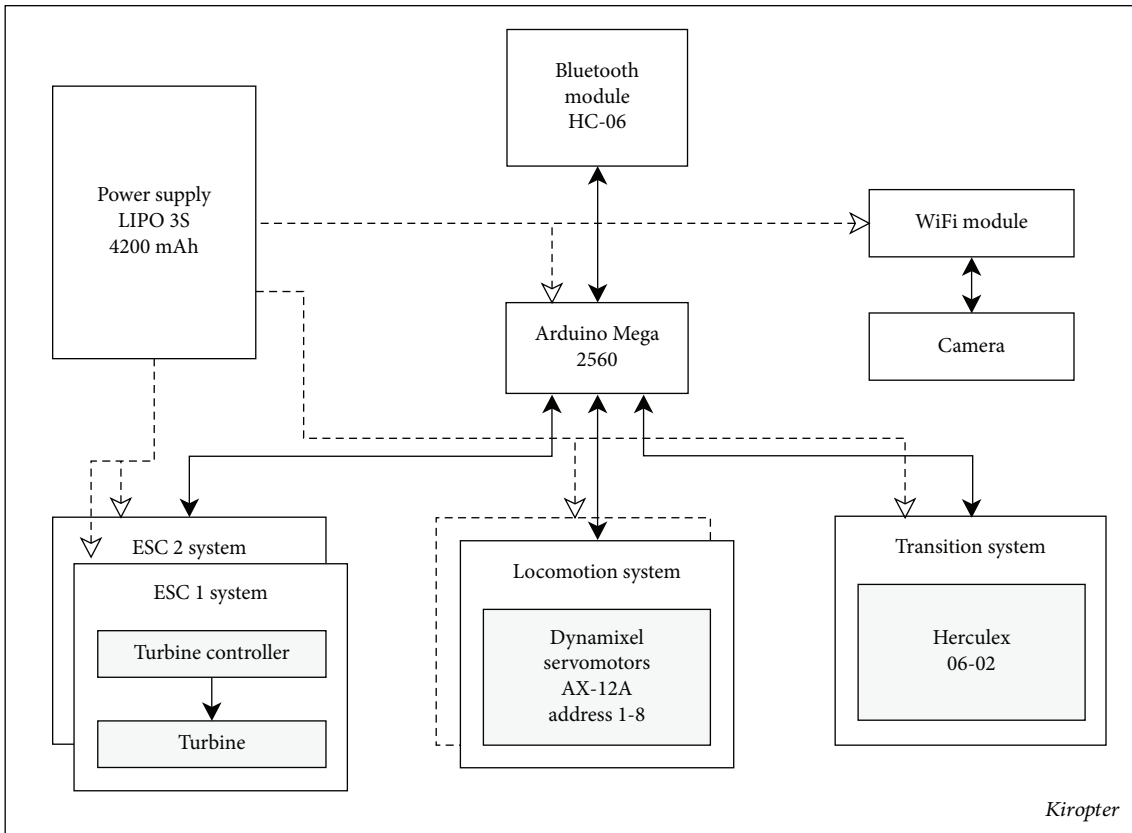
FIGURE 2: Hardware components and communication networks.

4. Enhanced Deep Learning Framework

This section describes the vision-based aircraft surface stain and defect detection based on the enhanced deep learning technique as shown in Figure 8. The framework has two phases which are preprocessing and detection.

4.1. Image Preprocessing. Generally, the backgrounds present in training and test image data can affect the learning and recognition abilities of all detection algorithms [26, 28, 38].

Through preprocessing, the effect of these backgrounds can be reduced, which can enhance the recognition accuracy at a relatively small cost. Preprocessing can also help enhance weak edges and features which the model may otherwise find difficult to learn. In view of these, a self-filtering-based periodic pattern detection filter and Sobel edge detection technique are adopted. The periodic pattern detection filter uses the self-filtering technique to suppress unwanted background patterns present in these images. This is based on
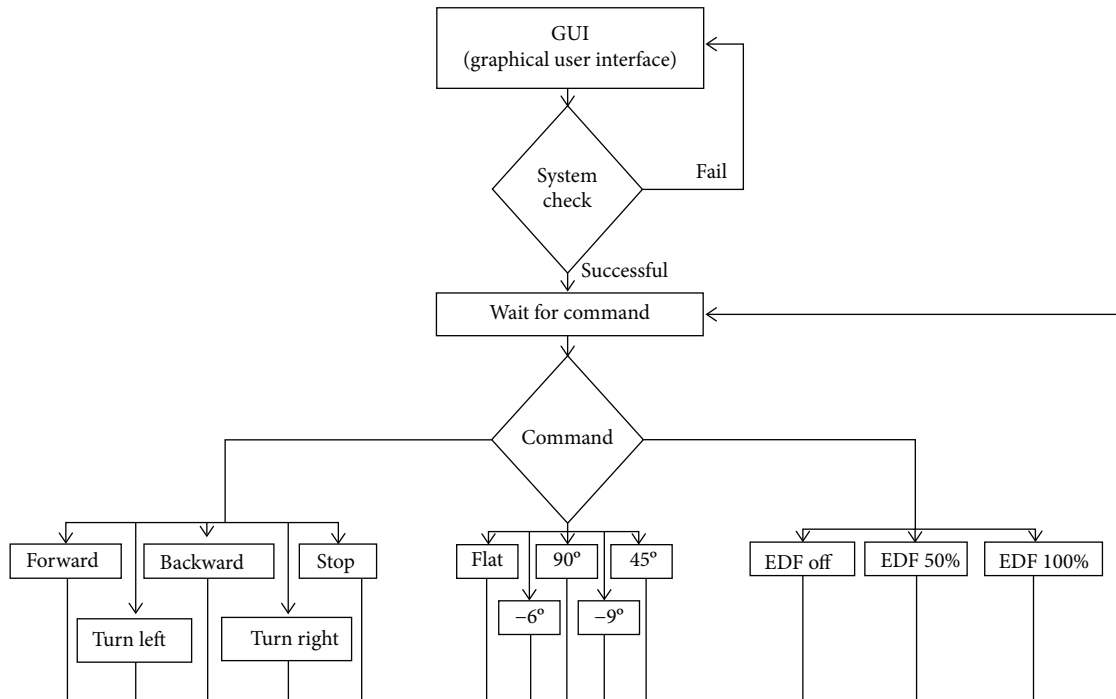
FIGURE 3: Control of the Kiropter flow chart, for three simultaneous commands.
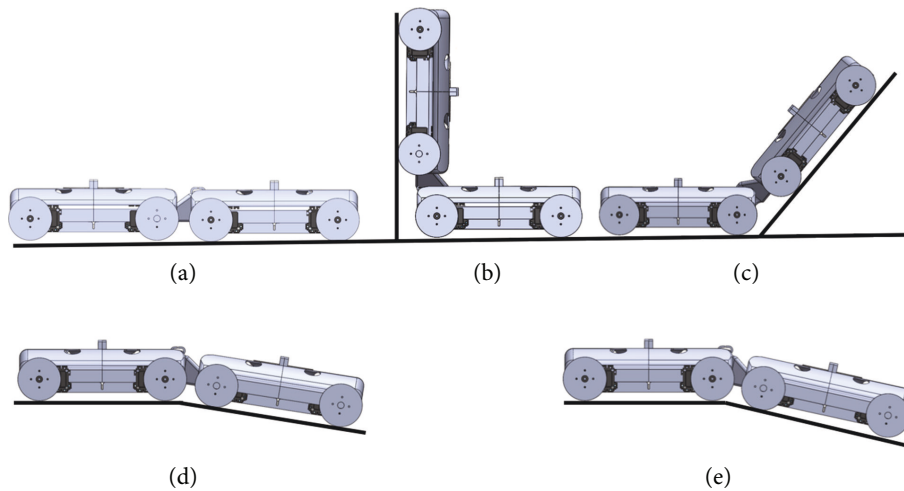
FIGURE 4: Configurations of the Kiropter for different situations: (a) flat, (b) 90° for the transition wing/body, (c) 45° for transition and navigation, (d) −6° for navigation on the 767 and 787 aircrafts, and (e) −9° for navigation on the 737 aircraft.
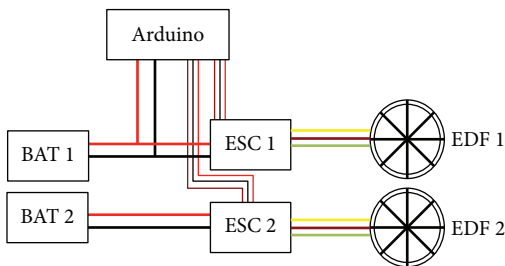
FIGURE 5: EDF connections to the energy and control unit.

the property that in the spatial domain, a periodic pattern on the captured image will have distinct peaks in the frequency domain. The self-filtering techniques automatically change the filter function according to the background of the image. It computes the appropriate filter function through computing the magnitude of the Fourier transformed image. After this, a Sobel edge detector is used to enhance the weak edges present in the image. The algorithm for the preprocessing stage is described in Algorithm 1.

Algorithm 1. Preprocessing algorithm.
    Data: grayscale image $g(x, y)$ (pixel coordinates x, y)
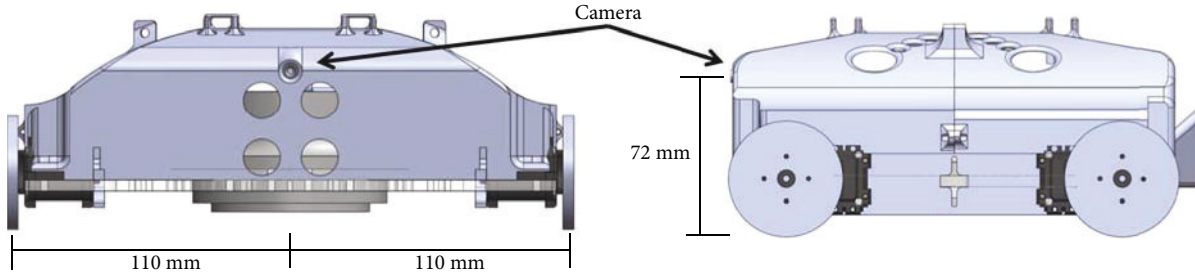
FIGURE 6: Position of the camera in the Kiropter: front and side views.
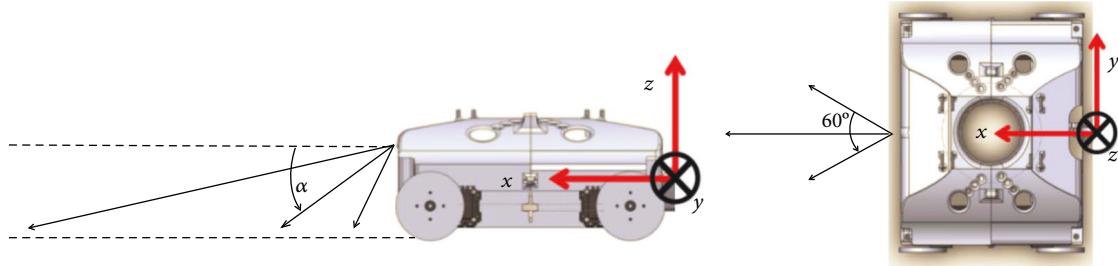
FIGURE 7: Angle of the view of the camera with respect to the inertial system of the robot.
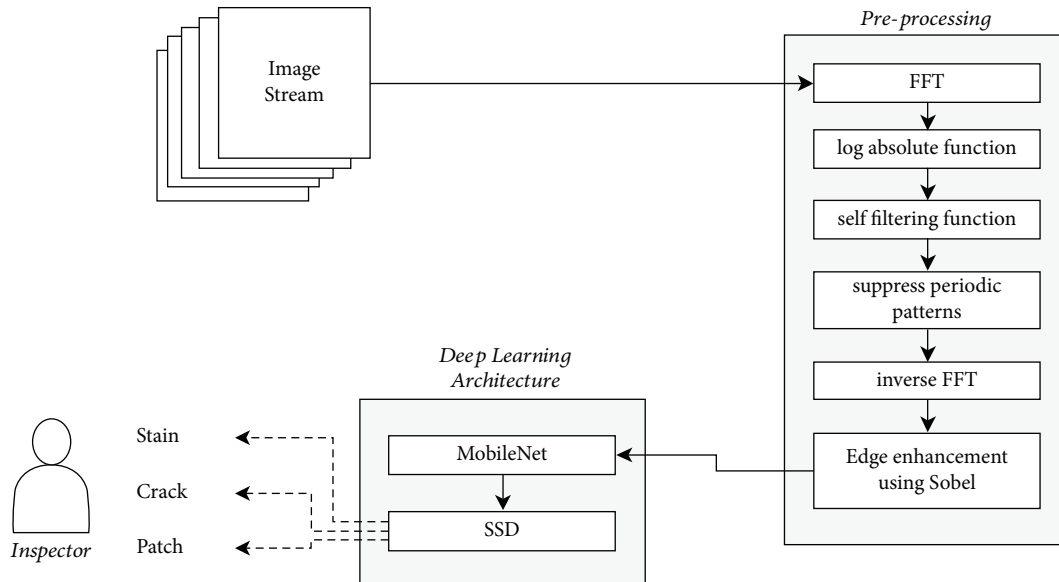
FIGURE 8: Enhanced deep learning scheme.

Result: $g'(x, y)$

Step 1: transform the image to a frequency domain (coordinates u, v) using 2D FFT then apply the FFT shift

$$
\begin{aligned}
F(u, v) &= \sum_{m=0}^{m-1} \sum_{n=0}^{n-1} g(x, y) \times e^{-i \times 2\pi \times ((u \times x/m) + (v \times y/n))} F'(u, v) \\
&= f(F(u, v)).
\end{aligned}
\tag{1}
$$

Step 2: apply the log absolute function on the Fourier transformed source image $F(u, v)$ to generate the amplitude

image $A(u, v)$

$$
A(u, v) = \log\left(\left|F'(u, v)\right|\right).
\tag{2}
$$

Step 3: compute the self-filtering function w_{max} from the amplitude image $A(u, v)$

$$
w_{max} = \max\left[\max\left[A(u, v)\right]\right].
\tag{3}
$$

Step 4: suppress the periodic patterns in the frequency

image using self-filtering function $w_{\max}$

$$F'(u, v) = \begin{cases} 0, & \text{if}\, A(u, v) > w_{\max}, \\ F'(u, v), & \text{otherwise.} \end{cases} \quad (4)$$

Step 5: transform the filtered image $F'(u, v)$ to the image space using inverse Fourier transform

$$g'(x, y) = \frac{1}{m \times n} \sum_{m=0}^{m-1} \sum_{n=0}^{n-1} f\left[F'(u, v)\right] \times e^{-i \times 2\pi \times ((u \times x/m) + (v+y/n))}. \quad (5)$$

Step 6: edge enhancement has been performed in this step. Due to the strong filtering effect on the prior stage, the edges of the stains and defects are slightly blurred which may affect the detection accuracy of the algorithm. Hence, the Sobel filter is adopted to enhance the edges of the defect and stain regions on the periodic pattern suppressed image.

4.2. SSD MobileNet Detection Network. SSD MobileNet is an object detection framework which is trained to detect and classify the defects and stains on the captured image. Here, MobileNet v2 is the base network utilized to extract the high-level feature from the images for classification and detection and SSD is a detection model which uses Mobile-Net feature map outputs and convolution layers of different sizes to classify and detect bounding boxes through regression. Connection of MobileNet and SSD is shown in Figure 9.

4.2.1. MobileNet V2 Architecture. MobileNet v2 [42] is a lightweight feature extractor that can be widely used for real-time detection applications and low-power-embedded systems. Figure 10 shows the functional block diagram of the MobileNet v2 architecture. MobileNet v2 uses residual units with bottleneck architecture for convolution module connection. The MobileNet v2 architecture comprises of three convolution layers including a 1×17 expansion layer, 3×3 depth-wise convolution layer, and 1×1 projection layer. Here, the expansion layer is employed to expand (default expansion factor is 6) the number of the channel in the data before going to depth-wise convolution, the next layer is a depth-wise convolution layer which filters the input, and the last layer is a projection layer which reduces the number of the channel by a factor of 6. It pretty much does the opposite of the expansion layer. Habitually, each convolution layer has batch normalization function and ReLU6 activation function. However, the output of the projection layer does not have an activation function applied to it.

4.2.2. SSD Architecture. SSD [43] is an object localizer which uses the output (feature map) from the final few layers of the feature extractor (MobileNet v2) to predict the location of different objects. SSD passes the input feature map through a series of convolution layers of varying sizes, which decrease in scale through the network. These layers allow it to detect objects of varying sizes. Each convolution layer also produces a fixed set of predictions, which contributes to a lower computation cost. Also, unlike traditional localizers, SSD chooses

the bounding box for each prediction from a fixed pool of sizes, which drastically reduces the computation time. This enables the SSD architecture to be used in real-time detection systems. The output of this network is location and confidence of a prediction. While training, the SSD architecture computes the total loss L at the end of each step as a combination of regression loss L_{location} between the predicted and actual locations and confidence loss of predicted class $L_{\text{confidence}}$ (equation (6)). α is a hyperparameter that balances the influence of the location loss on the total loss. This loss is optimized through the root mean squared loss optimization algorithm [44]. The RMS algorithm at any time t uses the gradient of loss g_t and velocity v_t to update the weight w^{RMS} (equation (7)). Here, β and η are hyperparameters for momentum calculation and E is a small value close to zero to prevent division by zero error.

$$L = \frac{1}{N}\left(L_{\text{confidence}} + \alpha L_{\text{location}}\right), \quad (6)$$

$$v_t = \beta v_{t-1} + (1 - \beta) g_t^2,$$
$$\Delta w^{\text{RMS}} = \frac{-\eta}{\sqrt{v_t + \varepsilon}} \times g_t, \quad (7)$$
$$w_{t+1}^{\text{RMS}} = w_t^{\text{RMS}} + \Delta w^{\text{RMS}}.$$

5. Experiments and Analysis

This section describes the experimental results of the proposed scheme. The experiment has been performed in two phases. The first phase validates the Kiropter robot performance on different aircraft surfaces and captures the aircraft surface for visual inspection. The second phase involves validation of the detection algorithm with the captured aircraft skin images. These images of defects and stains are captured by operating the robot using a semiautonomous mode. In the semiautonomous mode, the navigation control of the robot is performed manually through teleportation. However, during the semiautonomous mode, the robot avoids the windows and the nose of the plane automatically by using an inductive sensor and also performs the shape change automatically when it moves on the fuselage area.

5.1. Kiropter Robot Tests. The performance of the Kiropter robot was tested in two environments at the RoAR laboratory and ITE, Singapore. In the RoAR laboratory, the platform was tested on the curved aircraft skin, vertical flat, and glass surfaces. In the Institute of Technical Education (ITE) College, Singapore, the Kiropter robot was tested with an actual aircraft, specifically on Boeing 737 and combat aircraft models. These results are shown in Figure 11.

During the inspection, the robot was controlled through a GUI using Bluetooth communication. Through the GUI, the robot was paused in each stage (where stains and defects were visible) for a few seconds to capture the surface picture with better quality. The captured images are instantaneously sent to the remote inspection console and are also recorded in parallel in a 32 GB SD card present in the robot. The trial is performed in different regions of the aircraft surface
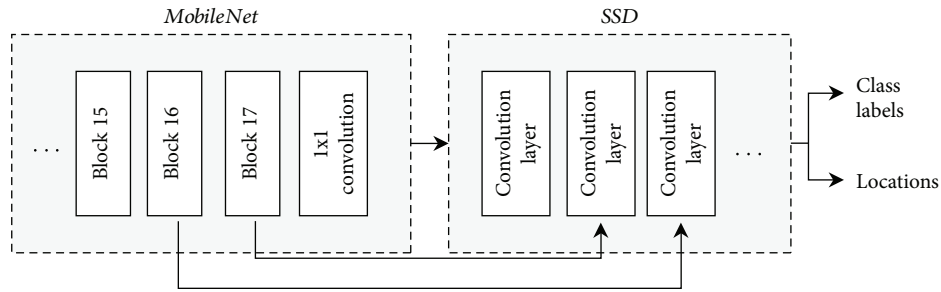
Figure 9: SSD MobileNet.
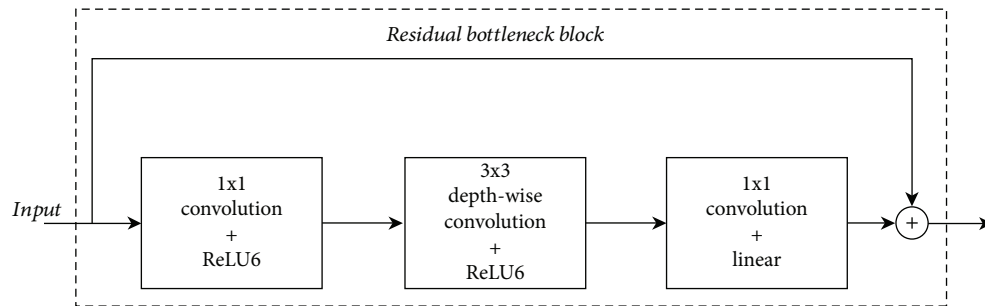
Figure 10: MobileNet.
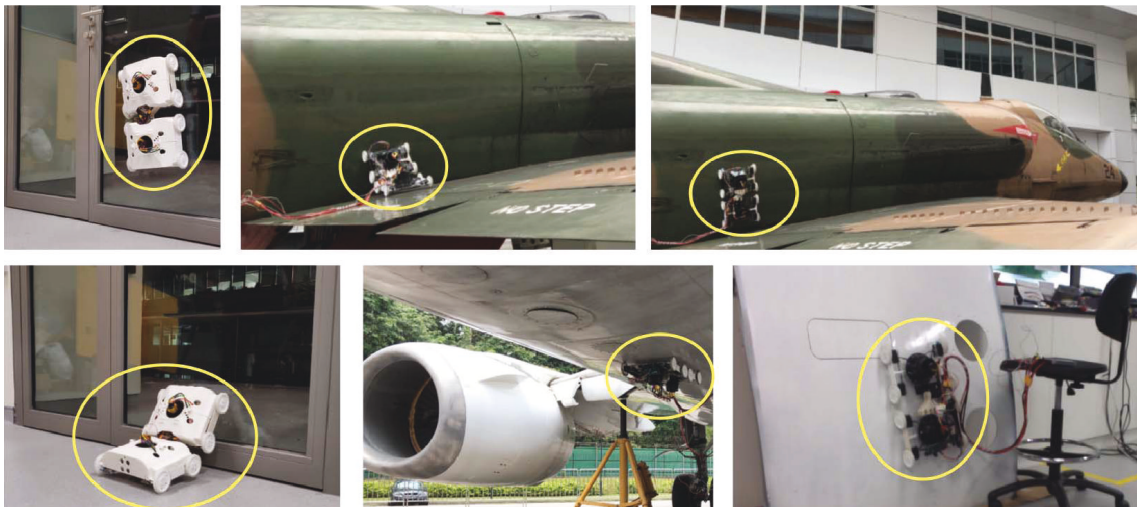
Figure 11: Kiropter robot in operation. The robot has been highlighted using yellow circles.

including the fuselage section, wings, and bottom of the air-craft surface. Figure 12 shows some of the defect and stain images captured by the Kiropter. These captured images have been used to train and test the detection algorithm.

5.2. Results of the Detection Network

5.2.1. Dataset Preparation.
The effectiveness of the detection algorithm has been tested manually with Kiropter captured aircraft skin images. This dataset contains about 2200 images from 15 different aircrafts located in ITE, Singapore. The images are balanced across the two classes—stains (mainly from oil and liquid spills) and defects (which include cracks, scratches, and patches). Each image is resized to a 640×480 resolution. Then, to improve the CNN learning rate and prevent overfitting, data expansion is applied to the captured images. Data expansion involves applying geometrical transformations such as rotation, scaling, and flipping. These images were then preprocessed and then labeled manually.

Standard performance metrics such as accuracy, precision, recall, miss rate, and F_1 scores are used to evaluate the model. The dataset is split into 10 sections for performing the K-fold (here K being 10) cross-validation process. In this process, 9 of these 10 splits are used for training and the remaining is used to evaluate the model. This process is
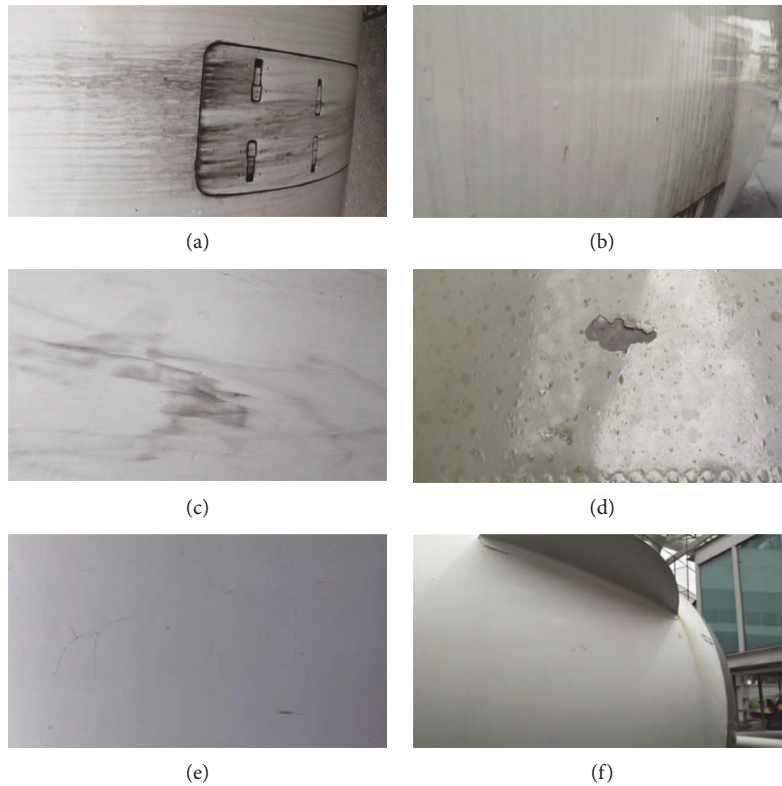
FIGURE 12: Captured defect and stain images. (a–c) have stains and (d–f) have defects.

repeated 10 times. *K*-fold cross-validation is used to remove any bias which could appear due to the particular split of training and testing data used. The performance metrics reported in this paper are the mean over these 10 runs. The images reported are from the model with the highest accuracy. The model was trained using the TensorFlow framework on Ubuntu 16.04 with the following hardware configuration Intel Xeon E5-1600 V4 CPU, 64 GB RAM and an NVIDIA Quadro P4000 GPU with 12 GB video memory.

5.2.2. Detection Results. Figures 13 and 14 show the detection results of the proposed algorithm. Here, stain regions are marked as a green rectangular box and defects are marked by a blue rectangular box. The experimental results show that the detection algorithm can able to detect most of the stains and defects in the captured skin image. Table 1 shows the number of detections of each class. There are 140 images from each class for validation of results. There are some cases where neither a stain nor defect is detected. The statistical results, shown in Table 2, indicate that the algorithm detected the defects with an average of 97% confidence level and stains are detected with an average of 94% confidence level. On the workstation used for training, the SSD MobileNet model takes 32 ms for one inference and the preprocessing takes 19 ms, which is a total time of 51 ms. On Jetson Nano, the SSD MobileNet scheme takes about 73 ms per image for a prediction. The enhanced scheme takes about 129 ms, which implies that 56 ms is required for the preprocessing algorithm to enhance the accuracy.

5.2.3. Comparison Analysis with the Standard Detection Network. The performance of the algorithm has been compared with standard SSD MobileNet (without a preprocessing stage) in terms of the abovementioned performance metrics. Both networks are trained for the same number of steps. Both stain detection and defect detection performance increases when preprocessing is used. In some cases, certain false classifications are avoided when preprocessing is used. This is evident in cases where defects and stains look similar but the difference is enhanced due to preprocessing. Few of these cases are shown in Figure 15. In most cases, the confidence with which the network predicts a certain class is increased for the case of enhanced images. This is because stains and defects can have similar features in most cases but the differences are enhanced when preprocessing is performed. Examples of this case are shown in Figure 16. In cases where the stain is faint, enhanced SSD MobileNet performs better than the standard network, which is shown in Figure 17. This can be attributed to the fact that preprocessing the images exposes subtle features and reduces unwanted background information, which makes it easier for the CNN architecture to identify.

5.2.4. Comparison with Other Aircraft Skin Inspection Schemes. This section describes the comparative analysis of the proposed algorithm with the existing aircraft surface inspection algorithm. The comparison has been performed based on the detection accuracy of each model. Table 3 shows the detection accuracy of various aircraft skin inspection algorithms based on the conventional method and deep
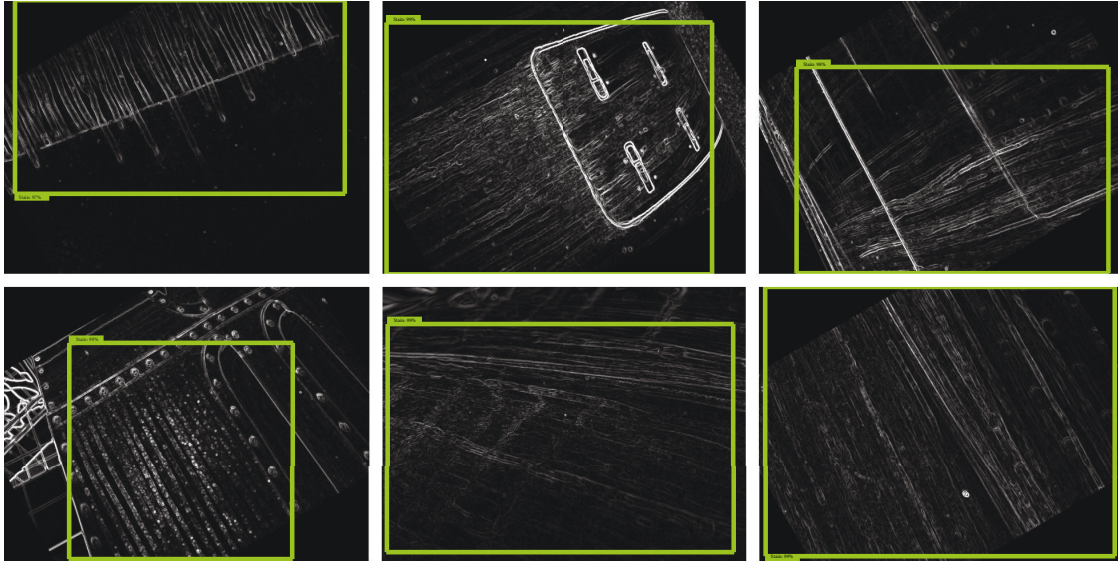
FIGURE 13: Stain detection results.
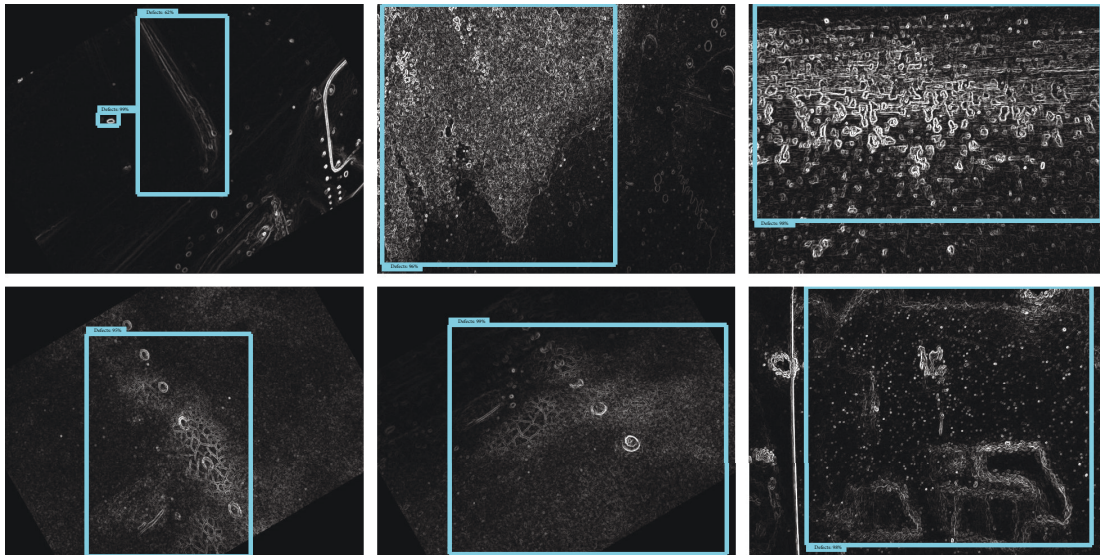
FIGURE 14: Defect detection results.

TABLE 1: True and false detections. There are 140 images from each class.

| Class (no.) | Predictions | | | |
| | SSD MobileNet | | Enhanced SSD MobileNet | |
	Stain	Defect	Stain	Defect
Stain (140)	106	22	130	4
Defect (140)	30	94	6	128

learning scheme. The result indicates that the proposed scheme achieves better accuracy than the Malekzadeh et al. [27] defect inspection scheme and the Siegel and Gunatilake [45] scheme. Moreover, all these works are only focused on defect detection. Since none of these works report stain detection, it is hard to actually compare the performance of the proposed scheme and the reported schemes.

5.2.5. Comparison with Other Defect Detection Schemes. The effectiveness of the proposed algorithm is further analyzed with the deep learning framework and DAGM 2007 defect image dataset. This DAGM 2007 dataset contains stain, crack, and pitted surfaces which are captured with different lighting conditions, in which the network achieved 93.2% accuracy.

Table 4 shows the detection accuracy of different schemes with the present scheme. Here, SSD MobileNet and the compact CNN scheme are used as a texture-based CNN scheme and AlexNet CNN and Faster RCNN are employed based on the content image dataset. From this table, it can be inferred that our detection algorithm has a strong detection

TABLE 2: Detection results.

Metric	SSD MobileNet		Enhanced SSD MobileNet	
	Stain	Defect	Stain	Defect
Accuracy	79.4		96.2	
Precision	82.8	75.8	97.0	95.4
Recall	77.9	81	95.5	96.8
F_1	80.3	78.3	96.3	96.1
Miss rate	8.6	11.4	4.2	7.1
Run time (Jetson Nano)	73 ms		129 ms	
Run time (workstation)	32 ms		51 ms	
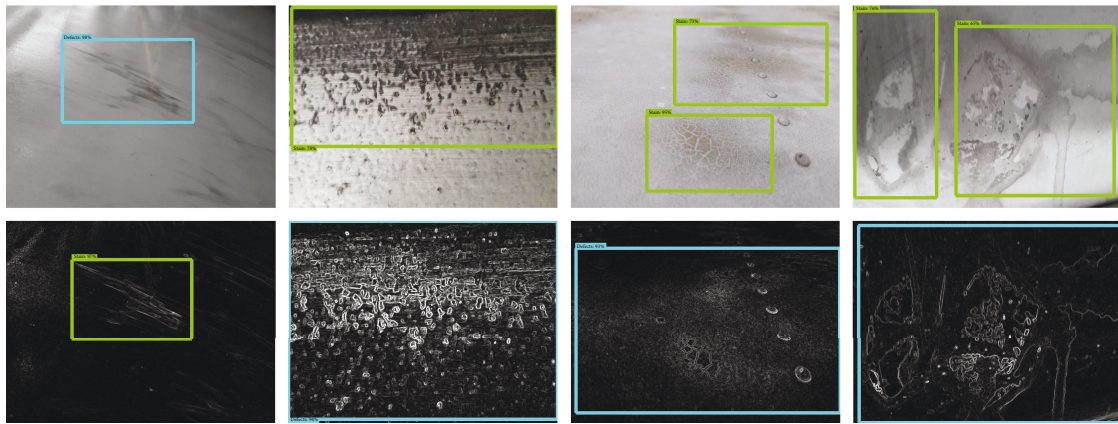
FIGURE 15: Comparison with SSD MobileNet based on false detection.
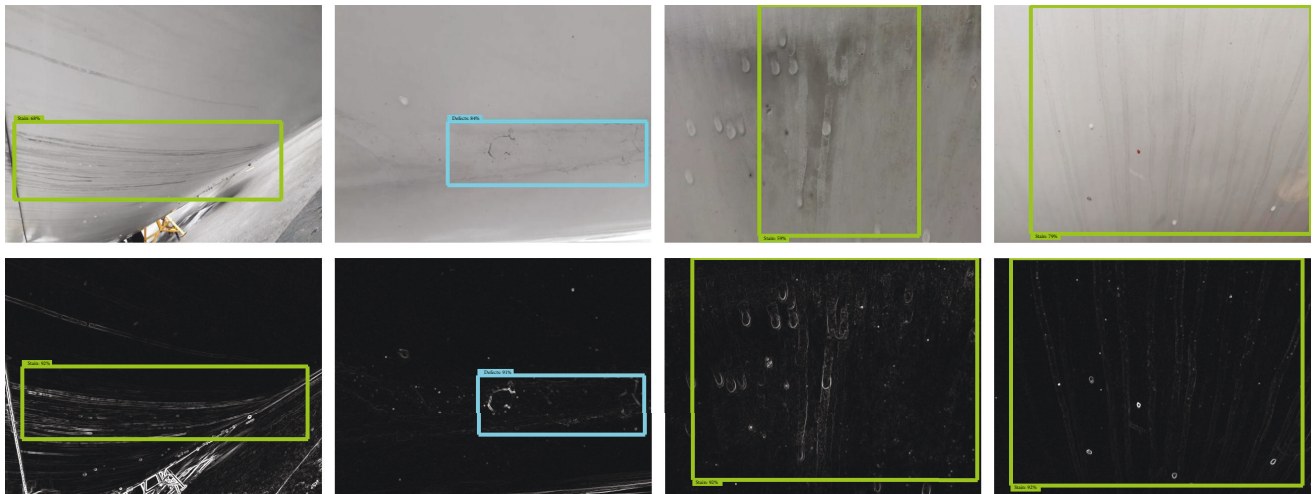
FIGURE 16: Comparison with SSD MobileNet based on prediction confidence.

capability on defective images with textured backgrounds and can adopt various defect detection applications. This is specifically true for detecting low-contrast objects such defects and stains. In contrast with traditional methods including AlexNet CNN and Faster RCNN, our method achieves better defect classification accuracy. However, since these networks are trained using different datasets for different applications, the performance cannot be accurately compared. Faster RCNN generally performs better than SSD MobileNet in object detection applications. The dispar-

ity in the table can be due to a difference in the number of different types of defects present in each dataset, as well as the preprocessing methods used. The proposed approach also groups all defects into one class, compared to the individual classes in some of the compared datasets, which can lead to better detection results.

5.3. Advantages and Limitations. Generally, UAV-based inspection has a lot of advantages over robot-based inspection due to its high mobility [35, 36, 46]. However, robot-
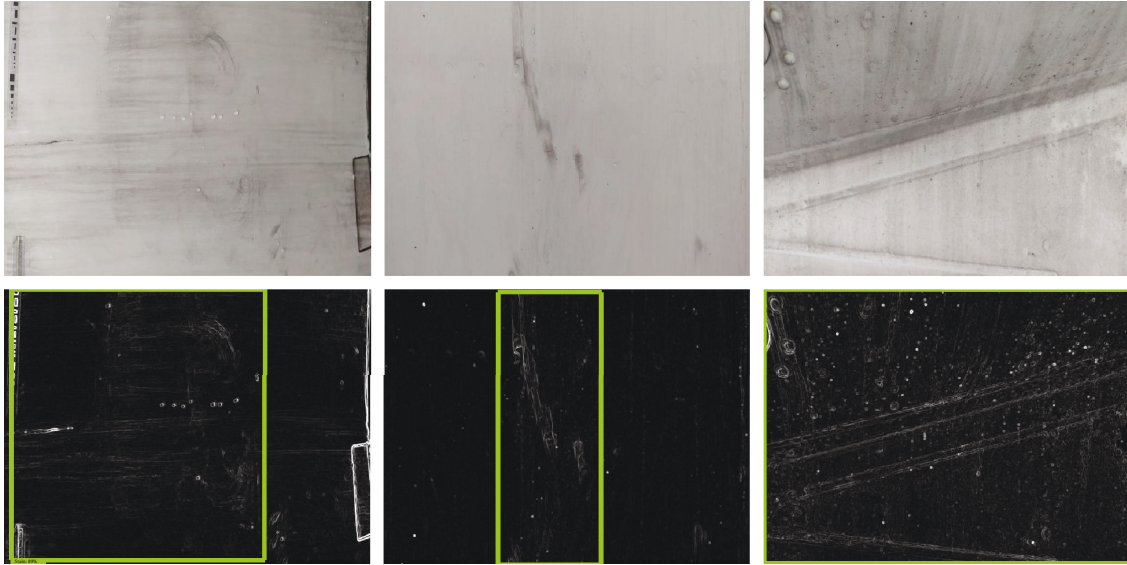
FIGURE 17: Comparison with SSD MobileNet based on miss detection.

TABLE 3: Comparison with aircraft inspection schemes.

Algorithm and inspection module	Class	Accuracy
ANN for the CIMP robot [45]	Crack and corrosion	83.5 (avg.)
Contourlet transform [23]	Crack and scratch	70
VGG Net [27]	Defect detection	87.62
AlexNet [27]	Defect detection	84.73
Enhanced SSD MobileNet	Stain and defect	96.2

TABLE 4: Comparison with other defect detection schemes.

Algorithm	Class	Accuracy	Application
AlexNet CNN [30]	Crack	90	Cracks on concrete surfaces
SSD MobileNet [26]	Surface defect detection	95	Surface defect detection
Compact CNN [28]	Damaged spots, dust, and scratches	86.82	Metallic surface defect detection
8-layer CNN in the UAV [36]	Crack	96.6	Cracks on concrete surfaces
Faster RCNN [29]	Crack, corrosion, and delamination	84.7	Metal surface inspection
Enhanced SSD MobileNet	Stain and defect	96.2	Aircraft inspection

based inspection is able to provide a close-up image of the defect or stain compared to UAVs. Also, due to a standard distance between the platform and the surface, the chance of missing a detection due to variable focus or vibration is lesser, compared to UAV-based models [35, 36]. This is shown in Table 4, where the authors report a loss of detection performance when CNN is used in the UAV due to vibration issue. Furthermore, the proposed robotic architecture can be extended to include automated cleaning systems, which can operate to clean the detected stains while also inspecting the surface for defects. The energy consumption is also reduced because the robot does not use an EDF on the upper part of the fuselage. The robot avoids areas of the airplane such as the nose, windows, and antennas, where the plane has sensitive sensors and materials that can be easily dam-

aged by the robot. Also, the robot is designed for larger aircrafts and is not suitable for small airplanes.

SSD MobileNet is a lightweight scheme which can perform real-time detection with the tradeoff of accuracy. Faster RCNN has better detection results but is larger and takes longer time to run. The enhancement of images through preprocessing increases the accuracy of the proposed model, while still being able to perform inference in real time.

6. Conclusion

This work proposed the aircraft surface inspection using an indigenously developed reconfigurable climbing robot (Kiropter) and enhanced visual inspection algorithm. An

enhanced SSD MobileNet-based deep learning framework is proposed for detecting stains and defects on the aircraft surface. In the preprocessing stage, a self-filtering-based periodic pattern detection filter was included in the SSD MobileNet deep learning framework to reduce the unwanted background information and enhance the defect and stain features. The feasibility of the proposed method was verified with parts of the aircraft skin in the RoAR lab and real aircrafts in ITE Aerospace, Singapore. The experimental results proved that the developed climbing robot can successfully move around the complex regions of the aircraft including the fuselage and confined area and capture the defect and stain regions. Further, the efficiency of the detection algorithm was verified with the captured image and its results are compared with conventional SSD MobileNet and existing defect detection algorithms. The statistical results show that the proposed enhanced SSD MobileNet framework achieves improved detection accuracy (96.2%) of aircraft surface defects (with an average of 97% confidence level) and stains (with a 94% confidence level). In contrast with conventional SSD MobileNet and other defect detection algorithms, the proposed scheme achieves better detection accuracy which is due to the removal of most of the unwanted background data. In our future work, we plan to test the robot with various aircrafts and also plan to increase the number of defected classification classes like corrosion, scratch, and pitted surface. We also plan to develop algorithms to localize these detected regions. Furthermore, the evaluation of seriousness of defects can be automated as well.

Data Availability

The data used to support the findings of this study are available from the corresponding author upon request.

Conflicts of Interest

The authors declare that there is no conflict of interest regarding the publication of this paper.

Supplementary Materials

Sample video of the robot Kiropter, for the demonstrative purposes. *(Supplementary Materials)*

References

[1] Civil Aviation Safety Authority Australia, *Airworthiness Bulletin*, 2019, January 2019, https://www.casa.gov.au/files/awb-indexpdf.

[2] J. Komorowski, D. Forsyth, D. Simpson, and R. Gould, "Probability of detection of corrosion in aircraft structures," in *RTO AVT workshop–airframe inspection reliability under field/depot conditions*, vol. 10, Brussels, Belgium, May 1998.

[3] P. Gunatilake, M. Siegel, A. G. Jordan, and G. W. Podnar, "Image enhancement and understanding for remote visual inspection of aircraft surface," in *Proc. SPIE 2945, Nondestructive Evaluation of Aging Aircraft, Airports, and Aerospace Hardware*, Scottsdale, AZ, USA, November 1996.

[4] M. Siegel and P. Gunatilake, "Remote enhanced visual inspection of aircraft by a mobile robot," in *Proc. of the 1998 IEEE Workshop on Emerging Technologies, Intelligent Measurement and Virtual Systems for Instrumentation and Measurement (ETIMVIS98)*, pp. 49–58, St. Paul, MN, USA, 1998.

[5] I. Jovančević, S. Larnier, J.-J. Orteu, and T. Sentenac, "Automated exterior inspection of an aircraft with a pan-tilt-zoom camera mounted on a mobile robot," *Journal of Electronic Imaging*, vol. 24, no. 6, article 061110, 2015.

[6] P. Gunatilake, M. Siegel, A. G. Jordan, and G. W. Podnar, "Image understanding algorithms for remote visual inspection of aircraft surfaces," in *Proc. SPIE 3029, Machine Vision Applications in Industrial Inspection V*, pp. 2–14, San Jose, CA, USA, April 1997.

[7] M. Siegel, P. Gunatilake, and G. Podnar, "Robotic assistants for aircraft inspectors," *IEEE Instrumentation & Measurement Magazine*, vol. 1, no. 1, pp. 16–30, 1998.

[8] B. Chu, K. Jung, C.-S. Han, and D. Hong, "A survey of climbing robots: locomotion and adhesion," *International Journal of Precision Engineering and Manufacturing*, vol. 11, no. 4, pp. 633–647, 2010.

[9] A. F. R. Laboratory, *Robotic arm tool poised to save costly inspection time*, International Journal of Precision Engineering and Manufacturing, December 2018, https://www.afspc.af.mil/News/Article-Display/Article/1088209/robotic-arm-tool-poised-to-save-costly-inspection-time/.

[10] X. Zhiwei, C. Muhua, and G. Qingji, "The structure and defects recognition algorithm of an aircraft surface defects inspection robot," in *2009 International Conference on Information and Automation*, pp. 740–745, Zhuhai, Macau, China, June 2009.

[11] C. Menon, M. Murphy, and M. Sitti, "Gecko inspired surface climbing robots," in *2004 IEEE International Conference on Robotics and Biomimetics*, pp. 431–436, Shenyang, China, August 2004.

[12] R. Lal Tummala, R. Mukherjee, Ning Xi et al., "Climbing the walls [robots]," *IEEE Robotics and Automation Magazine*, vol. 9, no. 4, pp. 10–19, 2002.

[13] S. Nansai and R. E. Mohan, "A survey of wall climbing robots: recent advances and challenges," *Robotics*, vol. 5, no. 3, p. 14, 2016.

[14] J. Yuan, X. Wu, Y. Kang, and A. Ben, "Research on reconfigurable robot technology for cable maintenance of cable-stayed bridges in-service," in *2010 International Conference on Mechanic Automation and Control Engineering*, pp. 1019–1022, Wuhan, China, June 2010.

[15] A. C. C. de Sousa, D. M. Viana, and C. M. C. e Cavalcante Koike, "Sensors in reconfigurable modular robot for pipeline inspection: design and tests of a prototype," in *2014 Joint Conference on Robotics: SBR-LARS Robotics Symposium and Robocontrol*, pp. 7–12, Sao Carlos, Brazil, October 2014.

[16] M. R. Jahanshahi, W.-M. Shen, T. G. Mondal, M. Abdelbarr, S. F. Masri, and U. A. Qidwai, "Reconfigurable swarm robots for structural health monitoring: a brief review," *International Journal of Intelligent Robotics and Applications*, vol. 1, no. 3, pp. 287–305, 2017.

[17] V. Prabakaran, M. R. Elara, T. Pathmakumar, and S. Nansai, "htetro: A tetris inspired shape shifting floor cleaning robot," in *2017 IEEE International Conference on Robotics and Automation (ICRA)*, pp. 6105–6112, Singapore, Singapore, May-June 2017.

[18] M. Ilyas, S. Yuyao, R. E. Mohan, M. Devarassu, and M. Kalimuthu, "Design of sTetro: a modular, reconfigurable, and autonomous staircase cleaning robot," *Journal of Sensors*, vol. 2018, Article ID 8190802, 16 pages, 2018.

[19] M. Yim, K. Roufas, D. Duff, Y. Zhang, C. Eldershaw, and S. Homans, "Modular reconfigurable robots in space applications," *Autonomous Robots*, vol. 14, no. 2/3, pp. 225–237, 2003.

[20] Y.-S. Kwon, E.-J. Jung, H. Lim, and B.-J. Yi, "Design of a reconfigurable indoor pipeline inspection robot," in *2007 International Conference on Control, Automation and Systems*, pp. 712–716, Seoul, South Korea, October 2007.

[21] A. Le, V. Prabakaran, V. Sivanantham, and R. Mohan, "Modified a-star algorithm for efficient coverage path planning in tetris inspired self-reconfigurable robot with integrated laser sensor," *Sensors*, vol. 18, no. 8, p. 2585, 2018.

[22] A. Le, M. Arunmozhi, P. Veerajagadheswar et al., "Complete path planning for a tetris-inspired self-reconfigurable robot by the genetic algorithm of the traveling salesman problem," *Electronics*, vol. 7, no. 12, p. 344, 2018.

[23] R. Mumtaz, M. Mumtaz, A. B. Mansoor, and H. Masood, "Computer aided visual inspection of aircraft surfaces," *International Journal of Image Processing*, vol. 6, no. 1, pp. 38–53, 2012.

[24] M. Rice, L. Li, G. Ying et al., *Automating the visual inspection of aircraft*, https://oar.a-star.edu.sg/jspui/handle/123456789/2336.

[25] A. Ortiz, F. Bonnin-Pascual, E. Garcia-Fidalgo, and J. Company-Corcoles, "Vision-based corrosion detection assisted by a micro-aerial vehicle in a vessel inspection application," *Sensors*, vol. 16, no. 12, article 2118, 2016.

[26] Y. Li, H. Huang, Q. Xie, L. Yao, and Q. Chen, "Research on a surface defect detection algorithm based on MobileNet-SSD," *Applied Sciences*, vol. 8, no. 9, article 1678, 2018.

[27] T. Malekzadeh, M. Abdollahzadeh, H. Nejati, and N.-M. Cheung, "Aircraft fuselage defect detection using deep neural networks," http://arxiv.org/abs/1712.09213.

[28] X. Tao, D. Zhang, W. Ma, X. Liu, and D. Xu, "Automatic metallic surface defect detection and recognition with convolutional neural networks," *Applied Sciences*, vol. 8, no. 9, article 1575, 2018.

[29] Y.-J. Cha, W. Choi, G. Suh, S. Mahmoudkhani, and O. Büyüköztürk, "Autonomous structural visual inspection using region-based deep learning for detecting multiple damage types," *Computer-Aided Civil and Infrastructure Engineering*, vol. 33, no. 9, pp. 731–747, 2018.

[30] B. Kim and S. Cho, "Automated vision-based detection of cracks on concrete surfaces using a deep learning technique," *Sensors*, vol. 18, no. 10, article 3452, 2018.

[31] R. Zhang, Z. Wang, and Y. Zhang, "Astronaut visual tracking of flying assistant robot in space station based on deep learning and probabilistic model," *International Journal of Aerospace Engineering*, vol. 2018, Article ID 6357185, 17 pages, 2018.

[32] Y.-J. Cha and W. Choi, "Vision-based concrete crack detection using a convolutional neural network," in *Dynamics of Civil Structures, Volume 2*, Conference Proceedings of the Society for Experimental Mechanics Series, J. Caicedo and S. Pakzad, Eds., pp. 71–73, Springer International Publishing, Cham, 2017.

[33] S. Deitsch, V. Christlein, S. Berger et al., "Automatic classification of defective photovoltaic module cells in electroluminescence images," CoRR abs/1807.02894. http://arxiv.org/abs/1807.02894.

[34] B. Ramalingam, A. Lakshmanan, M. Ilyas, A. le, and M. Elara, "Cascaded machine-learning technique for debris classification in floor-cleaning robot application," *Applied Sciences*, vol. 8, no. 12, article 2649.

[35] D. Kang and Y.-J. Cha, "Damage detection with an autonomous uav using deep learning," in *Proc. SPIE 10598, Sensors and Smart Structures Technologies for Civil, Mechanical, and Aerospace Systems 2018*, Denver, Colorado, USA, March 2018.

[36] D. Kang and Y.-J. Cha, "Autonomous UAVs for structural health monitoring using deep learning and an ultrasonic beacon system with geo-tagging," *Computer-Aided Civil and Infrastructure Engineering*, vol. 33, no. 10, pp. 885–902, 2018.

[37] R. Qian, Q. Liu, Y. Yue, F. Coenen, and B. Zhang, "Road surface traffic sign detection with hybrid region proposal and fast r-cnn," in *2016 12th International Conference on Natural Computation, Fuzzy Systems and Knowledge Discovery (ICNC-FSKD)*, pp. 555–559, Changsha, China, August 2016.

[38] W. Brendel and M. Bethge, "Approximating CNNs with bag-of-local-features models works surprisingly well on ImageNet," *International conference on learning representations*, 2019, https://openreview.net/forum?id=SkfMWhAqYQ.

[39] M. Siegel and P. Gunatilake, *Robotic Enhanced Visual Inspection of Aircraft Skin*, p. 530, 1999, http://www.academia.edu/download/6154878/10.1.1.172.9886.pdf.

[40] W. M. K. C. J. P. C. J. Alberts, C. W. Carroll, and M. W. Siegel, *Automated inspection of aircraft*, December 2018, http://www.tc.faa.gov/its/worldpac/techrpt/ar97-69.pdf.

[41] J. Shang, T. Sattar, S. Chen, and B. Bridge, "Design of a climbing robot for inspecting aircraft wings and fuselage," *Industrial Robot: An International Journal*, vol. 34, no. 6, pp. 495–502, 2007.

[42] A. G. Howard, M. Zhu, B. Chen et al., "MobileNets: efficient convolutional neural networks for mobile vision applications," http://arxiv.org/abs/1704.04861.

[43] W. Liu, D. Anguelov, D. Erhan et al., "SSD: single shot multibox detector," in *Computer Vision – ECCV 2016. ECCV 2016*, B. Leibe, J. Matas, N. Sebe, and M. Welling, Eds., vol. 9905 of Lecture Notes in Computer Science, pp. 21–37, Springer, Cham, 2016.

[44] T. Tieleman and G. Hinton, *Lecture 6.5-rmsprop, coursera: neural networks for machine learning* University of Toronto, Technical Report.

[45] M. Siegel and P. Gunatilake, "Enhanced remote visual inspection of aircraft skin," in *Proc. Intelligent NDE Sciences for Aging and Futuristic Aircraft Workshop*, pp. 101–112, Citeseer, 1997.

[46] H. Shakhatreh, A. H. Sawalmeh, A. al-Fuqaha et al., "Unmanned Aerial Vehicles (UAVs): a survey on civil applications and key research challenges," *IEEE Access*, vol. 7, pp. 48572–48634, 2019.

Research Article

Robust Integral Terminal Sliding Mode Control for Quadrotor UAV with External Disturbances

Moussa Labbadi and **Mohamed Cherkaoui**

Engineering for Smart and Sustainable Systems Research Center, Mohammadia School of Engineers,
Mohammed V University in Rabat, Morocco

Correspondence should be addressed to Moussa Labbadi; moussalabbadi@research.emi.ac.ma

The purpose of this paper is to solve the problem of controlling of the quadrotor exposed to external constant disturbances. The quadrotor system is partitioned into two parts: the attitude subsystem and the position subsystem. A new robust integral terminal sliding mode control law (RITSMC) is designed for stabilizing the inner loop and the quick tracking of the right desired values of the Euler angles. To estimate the disturbance displayed on the z-axis and to control the altitude position subsystem, an adaptive backstepping technique is proposed, while the horizontal position subsystem is controlled using the backstepping approach. The stability of the quadrotor subsystems is guaranteed by the Lyapunov theory. The effectiveness of the proposed methods is clearly comprehended through the obtained results of the various simulations effectuated on MATLAB/Simulink, and a comparison with another technique is presented.

1. Introduction

1.1. Background and Motivation. Over the last decade, the robotic field has attracted great attention from researchers, in particular, the unmanned aerial vehicle (UAV). The quadrotor is a type of drone, which consists of four rotors. This last has a simple mechanical structure. The quadrotor can land vertically and take off. The quadrotor has been used in many applications such as military missions, journalism, disaster management, archaeology, geographical monitoring, taxi services, search/rescue missions, environmental protection, performing missions in oceans or other planets, mailing and delivery, and other miscellaneous applications [1, 2]. Therefore, the quadrotor is a strongly coupled and highly nonlinear system. The quadrotor is an underactuated system, because the six DOF ($x, y, z, \phi, \theta,$ and ψ) should be regulated by the four controls.

In order to control the quadrotor in a closed loop, many techniques have been designed such as the backstepping control, fuzzy logic based on intelligent control, sliding mode control, adaptive control approaches, neural network method, intelligent fuzzy logic control, model predictive

control [3], hybrid finite-time control [4], proportional derivative sliding mode control [5], nonlinear PID controller [6], and adaptive fractional order sliding mode control [7].

1.2. Literature Review. In Reference [8], nonlinear control techniques are designed for the quadrotor's position and attitude. The attitude loop uses the regular sliding mode controller. The backstepping technique is combined with a sliding mode control to design robust controllers for the outer loop and the yaw angle. In order to estimate the quadrotor UAV fault, an observer is developed. In Reference [9], a second-order sliding mode control technique is developed to control an underactuated quadrotor UAV. In order to select the best coefficient of this proposed controller, the Hurwitz analysis is used. The control approach allows converging the state variables to their reference values and ensuring the stability of the quadrotor system. In Reference [10], a global fast terminal sliding mode control technique is developed for a quadrotor UAV. The controller allows solving the chattering problem, stabilizing the vehicle, and converging all state variables to zero. In Reference [11], a nonsingular fast terminal SMC technique has been established for the stabilization and
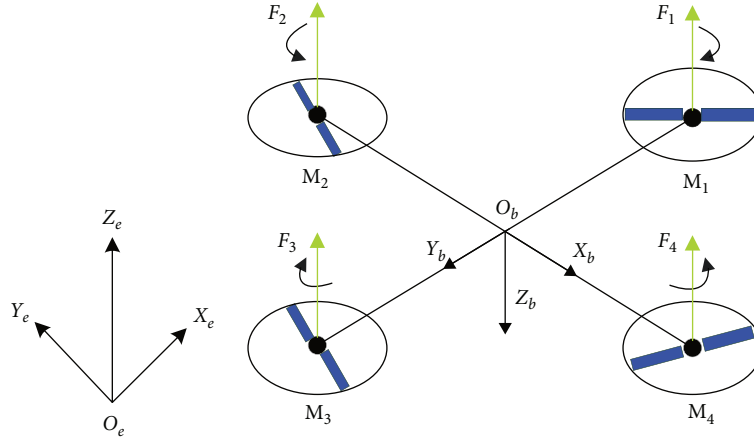
Figure 1: The quadrotor UAV with four rotors.

control of uncertain and nonlinear dynamical systems based on a disturbance observer. In Reference [12], an adaptive control method based on the sliding mode technique is developed for tracking control and for the stability of an uncertain quadrotor. The quadrotor unknown parameters are estimated at any moment. The proposed control laws guarantee the stability of the quadrotor system and recommend that the state variables converge to their origin values in finite time. A combination of sliding mode control and integral backstepping techniques is presented in Reference [13]. The control strategy allows tracking of the flight trajectory in the presence of the disturbances and stabilizing of the attitude of the UAV. In Reference [14], a nonsingular fast terminal sliding mode (NFTSM) method is designed to obtain the good performance of the quadrotor attitude. The tracking errors of the quadrotor are converged to zero through this controller. In the study by Reference [15], a fast terminal SMC approach is proposed for the tracking control problem of a nonlinear mass-spring system in the presence of noise, exterior disturbance, and parametric uncertainty. The proposed controller is confirmed via both experimental and simulation results. In Reference [16], a high-order sliding mode observer is combined with a nonsingular modified super-twisting algorithm to propose a solution for the trajectory-tracking problem of unmanned aerial systems (UAS). The proposed approach techniques offer an estimation for the translational velocities of the quadrotor and improve the robust performance ability of the UAV system against external disturbances. In Reference [17], an adaptive super-twisting based on the terminal sliding mode technique is applied on the fourth-order systems. The experimental results of the proposed control scheme are presented. In Reference [18], a terminal sliding mode controller for the yaw and altitude subsystems is designed. A sliding mode technique is developed to control the quadrotor underactuated subsystem. In Reference [19], two nonlinear control techniques (backstepping and sliding mode controllers) are suggested to solve the tracking trajectory problem in the presence of relatively high perturbations, problems of the quadrotor system affected by input delays, parametric uncertainties, unmolded uncertainties, and time-varying state and external disturbances; a robust nominal control-

ler and a robust compensator are proposed in Reference [20] to solve the process.

1.3. Contribution. In this paper, a robust integral terminal sliding mode control method is proposed for a quadrotor attitude. Then, an integral terminal sliding mode surface is used for the attitude of the quadrotor to ensure tracking errors converge to zero in short finite time. The RITSMC scheme is designed based on the Lyapunov theory. However, an adaptive backstepping is designed to estimate the unknown external disturbance acting in the z-axis and to control the altitude subsystem. The backstepping technique is used to control the horizontal position of the quadrotor in the presence of external perturbations. The contribution of this paper is given by the following points:

(i) A novel hybrid control structure of the quadrotor system subject to underactuated, kinematics-dynamics couplings, and external disturbances is proposed

(ii) An RITSMC is proposed for the quadrotor attitude to eliminate singularities without adding any constraints compared to TSMC and to reduce the chattering effect in the conventional SMC

(iii) An AB control approach commands the altitude of the quadrotor and estimates the disturbances at any moment simultaneously

1.4. Paper Organization. The rest of the paper is structured as follows: the formulation of the quadrotor system is given in Section 2. The new RITSMC and the adaptive backstepping techniques are presented in Section 3. The numerical simulation results are prepared in Section 4. Finally, the conclusions are exposed in Section 5.

2. The System Modeling

The quadrotor is equipped with four rotors as shown in Figure 1. The body-fixed (O_b, X_b, Y_b, and Z_b) and earth-fixed (O_e, X_e, Y_e, and Z_e) frames are defined. The absolute position of the quadrotor is defined by the vector $\xi =$

$[x, y, z]^T$. The vector $\eta = [\phi, \theta, \psi]^T$ represents the Euler angles. The angular and linear velocities of the quadrotor are defined by the vectors $\Omega = [p, q, r]^T$ and $V = [u, v, w]^T$, respectively.

In this context, the formalism of Newton-Euler is used to obtain the quadrotor model [19, 21, 22]:

$$\begin{cases} \dot{\xi} = V, \\ m\dot{V} = R F e_3 - mge_3 - k_i \quad (i = 1, 2, 3), \\ \dot{R} = RS(\Omega), \\ J\dot{\Omega} = -\Omega \times J \Omega + M_c - M_a + M_b. \end{cases} \tag{1}$$

R is the rotation matrix

$$R = \begin{bmatrix} C_\theta C_\psi & S_\phi S_\theta C_\psi - C_\phi S_\psi & C_\phi S_\theta C_\psi + S_\phi S_\psi \\ C_\theta S_\psi & S_\phi C_\theta S_\psi + C_\phi S_\psi & C_\phi S_\theta S_\psi - S_\phi C_\psi \\ -S_\theta & C_\phi C_\theta & C_\phi C_\theta \end{bmatrix}. \tag{2}$$

The coordinate transformation is given by the rotation matrix:

$$T = \begin{bmatrix} 1 & 0 & -S_\theta \\ 0 & C_\phi & S_\phi C_\theta \\ 0 & -S_\phi & C_\phi C_\theta \end{bmatrix}. \tag{3}$$

We use $C(.)$ to cos $(.)$ and $S(.)$ to sin $(.)$. m represents the total mass of the quadrotor, $I_{3\times3}$ is a density matrix, and $J = \text{diag} \ (I_x, I_y, I_z)$ denotes the matrix moment of the inertia. F is the total thrust; this expression is given by $F = F_1 + F_2 + F_3 + F_4$ where $F_i = b\Omega_i^2$, Ω_i is the angular speed and b is a parameter that depends on the air density and blade geometry. $S = [p, q, r]^T$ denotes a skew-symmetric matrix. M_a, M_c, and M_a are the resultant of the aerodynamic friction torque, the resultant of the gyroscopic effect torque, and the torque developed by the four rotors of the quadrotor, respectively. These expressions can be given, respectively, as follows:

$$M_a = \text{diad} \left(k_4 \dot{\phi}^2, k_5 \dot{\theta}^2, k_6 \dot{\psi}^2 \right), \tag{4}$$

where k_4, k_5, and k_6 represent the friction aerodynamics parameters.

$$M_c = \sum_{i=0}^{4} \Omega \times J_r \left[0, 0, (-1)^{i+1} \Omega_i \right]^T. \tag{5}$$

J_r denotes the rotor inertia.

$$M_b = \begin{bmatrix} l(F_3 - F_1) \\ l(F_4 - F_2) \\ d(-\Omega_1 + \Omega_2 - \Omega_3 + \Omega_4) \end{bmatrix}, \tag{6}$$

d is the drag coefficient and l is the distance between a propel-

ler and the center of the quadrotor. The complete quadrotor dynamics in the presence of external disturbances referred to in [22] is as

$$\begin{cases} \ddot{\phi} = \dot{\theta}\dot{\psi}\dfrac{I_y - I_z}{I_x} - \dot{\theta}\dfrac{J_r}{I_x}\Omega_r - \dfrac{k_4}{I_x}\dot{\phi}^2 + \dfrac{1}{I_x}U_2 + d_\phi, \\[2mm] \ddot{\theta} = \dot{\phi}\dot{\psi}\dfrac{I_z - I_x}{I_y} + \dot{\phi}\dfrac{J_r}{I_y}\Omega_r - \dfrac{k_5}{I_y}\dot{\theta}^2 + \dfrac{1}{I_y}U_3 + d_\theta, \\[2mm] \ddot{\psi} = \dot{\phi}\dot{\theta}\dfrac{I_x - I_y}{I_z} - \dfrac{k_6}{I_z}\dot{\psi}^2 + \dfrac{1}{I_z}U_4 + d_\psi, \\[2mm] \ddot{x} = \dfrac{1}{m}\left(\left(C_\phi S_\theta C_\psi + S_\phi S_\psi \right) U_1 + d_x \right) - \dfrac{k_1}{m}\dot{x}, \\[2mm] \ddot{y} = \dfrac{1}{m}\left(\left(C_\phi S_\theta S_\psi - S_\phi C_\psi \right) U_1 + d_y \right) - \dfrac{k_2}{m}\dot{y}, \\[2mm] \ddot{z} = \dfrac{1}{m}\left(C_\phi C_\theta U_1 + d_z \right) - g - \dfrac{k_3}{m}\dot{z}. \end{cases} \tag{7}$$

The relationship between the quadrotor inputs and the propeller speeds of the quadrotor can be written as follows [22]:

$$\begin{bmatrix} U_1 \\ U_2 \\ U_3 \\ U_4 \end{bmatrix} = \begin{bmatrix} b & b & b & b \\ -lb & 0 & lb & 0 \\ 0 & -lb & 0 & lb \\ -d & +d & -d & d \end{bmatrix} \begin{bmatrix} \Omega_1^2 \\ \Omega_2^2 \\ \Omega_3^2 \\ \Omega_4^2 \end{bmatrix}. \tag{8}$$

The dynamic model of the quadrotor position subsystem has three outputs (z, x, and y) and one control input U_1. In order to solve the underactuated problem, three virtual control (v_1, v_2, and v_3) inputs using adaptive backstepping and the backstepping technique are designed. The virtual control inputs are given as follows:

$$\begin{bmatrix} v_1 \\ v_2 \\ v_3 \end{bmatrix} = \begin{bmatrix} \dfrac{U_1}{m}\left(C_\phi S_\theta C_\psi + S_\phi S_\psi \right) \\[2mm] \dfrac{U_1}{m}\left(C_\phi S_\theta S_\psi - S_\phi C_\psi \right) \\[2mm] \dfrac{U_1}{m}\left(C_\phi C_\theta \right) - g \end{bmatrix}. \tag{9}$$

Therefore, the desired roll, pitch, and yaw angles (ϕ_d, θ_d) and the total thrust U_1 can be obtained as follows:

$$\begin{cases} U_1 = m\sqrt{v_1^2 + v_2^2 + (v_3 + g)^2}, \\[2mm] \phi_d = \arctan \left[S_{\theta d} \left(\dfrac{v_1 C_{\psi d} - v_2 S_{\psi d}}{v_3 + g} \right) \right], \\[2mm] \theta_d = \arctan \left(\dfrac{v_1 C_{\psi d} + v_2 S_{\psi d}}{(v_3 + g)} \right). \end{cases} \tag{10}$$
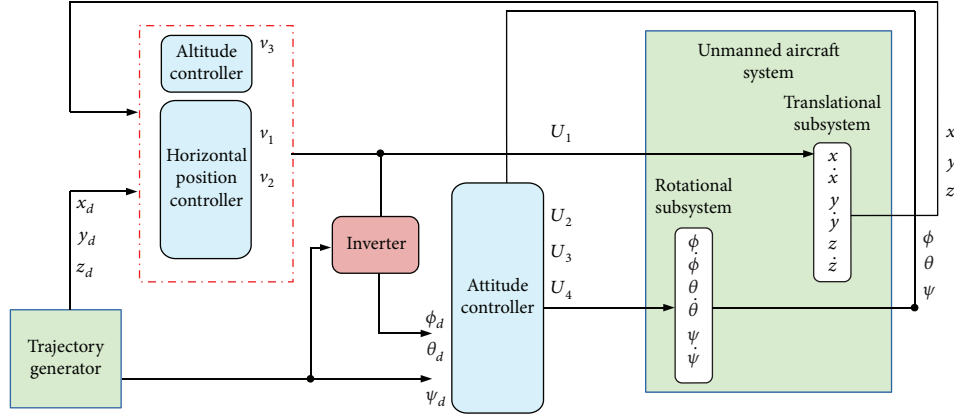
FIGURE 2: The control general structure for the quadrotor UAV.

3. Controller Design and Stability Analysis

This section presents the robust nonlinear controller for the quadrotor UAV in the presence of external perturbations. The proposed control of the quadrotor is divided into the inner loop and the outer loop. For the outer loop, an adaptive backstepping (AB) controller for the altitude subsystem is designed. The AB method ensures the tracking of the desired altitude z_d and an accurate estimation of the unknown perturbation d_z acting on the altitude subsystem. The backstepping technique is used to obtain the virtual control (v_1, v_2). For the inner loop, a new robust integral terminal sliding mode control (RITSMC) is proposed. The attitude controller generates the rolling, pitching, and yawing torques to control the orientation of the quadrotor in the presence of external disturbances. Finally, the proposed control strategy solves the trajectory problem in short finite time with accuracy of the system performance. The general proposed control scheme is shown in Figure 2.

3.1. Adaptive Backstepping Control for Altitude Subsystem.
Define tracking error of the altitude subsystem as

$$e_{z1} = z - z_d. \tag{11}$$

Consider the Lyapunov candidate function:

$$V_{z1} = \frac{1}{2}e_{z1}^2. \tag{12}$$

Taking the time derivative of equation (12)

$$\dot{V}_{z1} = e_{z1}\dot{e}_{z1} = e_{z1}(\dot{z} - \dot{z}_d). \tag{13}$$

The virtual control law is

$$\alpha_z = -c_{z1}e_{z1} + \dot{z}_d, \tag{14}$$

where $c_{z1} > 0$ is a positive constant.
Define the tracking error of step 2 as

$$e_{z2} = \dot{z} - \alpha_z. \tag{15}$$

The virtual control and adaptive law of the altitude subsystem are given by equation (16) and equation (17), respectively:

$$v_3 = -\left(e_{z1} + c_{z1}(e_{z2} - cz1e_{z1}) + c_{z2}e_{z2} + \frac{k_3}{m}\dot{z} - \ddot{z}_d + \hat{d}_z\right), \tag{16}$$

$$\dot{\hat{d}}_z = \gamma_z e_{z2}, \tag{17}$$

where c_{z2} and γ_z are the positive parameters and $\hat{d}_z$ denotes the estimate of d_z.

Proof. The Lyapunov function is considered as follows:

$$V_{z2} = \frac{1}{2}e_{z1}^2 + \frac{1}{2}e_{z2}^2 + \frac{1}{2\gamma_z}\tilde{d}_z^2. \tag{18}$$

The time derivative of V_{z2} is given as

$$\begin{aligned}
\dot{V}_{z2} &= e_{z1}\dot{e}_{z1} + e_{z2}\dot{e}_{z2} + \frac{1}{\gamma_z}\dot{\hat{d}}_z\tilde{d}_z \\
&= e_{z1}(e_{z2} - c_{z1}e_{z1}) + e_{z2}(\ddot{z} + c_{z1}\dot{e}_{z1} - \ddot{z}_d) - \frac{1}{\gamma_z}\dot{\hat{d}}_z\tilde{d}_z \\
&= -c_{z1}e_{z1}^2 + e_{z2}\left[-\frac{k_3}{m}\dot{z} + v_3 + c_{z1}(e_{z2} - c_{z1}e_{z1}) - \ddot{z}_d\right] \\
&\quad + e_{z2}\hat{d}_z + d_z\left(e_{z2} - \frac{\dot{\hat{d}}_z}{\gamma_z}\right).
\end{aligned} \tag{19}$$

Considering the control law equation (16) and adaptive law equation (17), we get

$$\dot{V}_{z2} = -c_{z1}e_{z1}^2 - c_{z2}e_{z2}^2 \leq 0. \tag{20}$$

3.2. Backstepping Control for Horizontal Position Subsystem.
In this part, the backstepping technique is used to control the horizontal position of a quadrotor.
Introduce the tracking errors of the x and y positions:

$$\begin{aligned}
e_{x1} &= x - x_d, \\
e_{y1} &= y - y_d.
\end{aligned} \tag{21}$$

Define the Lyapunov candidate function as

$$V_{x1} = \frac{1}{2}e_{x1}{}^2,\tag{22}$$

$$V_{y1} = \frac{1}{2}e_{y1}{}^2.\tag{23}$$

The time derivatives of equations (23) and (24) are given by

$$\dot{V}_{x1} = e_{x1}\dot{e}_{x1} = e_{x1}(\dot{x} - \dot{x}_d),\tag{24}$$

$$\dot{V}_{y1} = e_{y1}\dot{e}_{y1} = e_{y1}(\dot{y} - \dot{y}_d).\tag{25}$$

From equation (25), the virtual control laws are

$$\begin{aligned}\alpha_x &= -c_{x1}e_{x1} + \dot{x}_d,\\ \alpha_y &= -c_{y1}e_{y1} + \dot{y}_d,\end{aligned}\tag{26}$$

where $c_{x1}, c_{y1} > 0$ are the positive constants.

Consider the tracking errors of step 2 are given as

$$\begin{aligned}e_{x2} &= \dot{x} - \alpha_x,\\ e_{y2} &= \dot{y} - \alpha_y.\end{aligned}\tag{27}$$

The virtual control laws of the horizontal subsystems are given by

$$\begin{aligned}v_1 &= -\left(e_{x1} + c_{x1}(e_{x2} - c_{x1}\,e_{x1}) + c_{x2}e_{x2} + \frac{k_1}{m}\dot{x} - \ddot{x}_d + d_x\right),\\ v_2 &= -\left(e_{y1} + c_{y1}(e_{y2} - c_{y1}\,e_{y1}) + c_{y2}e_{y2} + \frac{k_2}{m}\dot{y} - \ddot{y}_d + d_y\right).\end{aligned}\tag{28}$$

Proof. Using the same, procedure presented in the subsection 3.1 demonstrate the stability of horizontal subsystem.

3.3. Robust Integral Terminal Sliding Mode Control Laws for Attitude Subsystem. In order to solve the chattering phenomenon and to eliminate the singularity in a TSMC, a robust nonlinear controller based on the integral terminal sliding mode technique is designed for the quadrotor attitude.

Introduce the tracking errors and its derivative, respectively, of the attitude subsystem:

$$\begin{cases}e_\phi = \phi - \phi_d,\\ e_\theta = \theta - \theta_d,\\ e_\psi = \psi - \psi_d,\\ \dot{e}_\phi = \dot{\phi} - \dot{\phi}_d,\\ \dot{e}_\theta = \dot{\theta} - \dot{\theta}_d,\\ \dot{e}_\psi = \dot{\psi} - \dot{\psi}_d.\end{cases}\tag{29}$$

Consider the ITSM surface function as of the quadrotor attitude as [23, 24]

$$\begin{cases}s_\phi = \dot{e}_\phi + \int\left(\alpha_\phi\dot{e}_\phi{}^{(q_\phi/p_\phi)} + \beta_\phi e_\phi{}^{(q_\phi/(2p_\phi - q_\phi))}\right)dt,\\ s_\theta = \dot{e}_\theta + \int\left(\alpha_\theta\dot{e}_\theta{}^{(q_\theta/p_\theta)} + \beta_\theta e_\theta{}^{(q_\theta/(2p_\theta - q_\theta))}\right)dt,\\ s_\psi = \dot{e}_\psi + \int\left(\alpha_\psi\dot{e}_\psi{}^{(q_\psi/p_\psi)} + \beta_\psi e_\psi{}^{(q_\psi/(2p_\psi - q_\psi))}\right)dt,\end{cases}\tag{30}$$

where $\alpha_i(i = \phi, \theta, \psi)$ and $\beta_i(i = \phi, \theta, \psi)$ are the positive constants and $p_i(i = \phi, \theta, \psi)$ and $q_i(i = \phi, \theta, \psi)$ the positive integers with $p_i > q_i$.

The surface dynamics are given by

$$\begin{cases}\dot{s}_\phi = \ddot{e}_\phi + \alpha_\phi\dot{e}_\phi{}^{(q_\phi/p_\phi)} + \beta_\phi e_\phi{}^{(q_\phi/(2p_\phi - q_\phi))},\\ \dot{s}_\theta = \ddot{e}_\theta + \alpha_\theta\dot{e}_\theta{}^{(q_\theta/p_\theta)} + \beta_\theta e_\theta{}^{(q_\theta/(2p_\theta - q_\theta))},\\ \dot{s}_\psi = \ddot{e}_\psi + \alpha_\psi\dot{e}_\psi{}^{(q_\psi/p_\psi)} + \beta_\psi e_\psi{}^{(q_\psi/(2p_\psi - q_\psi))}.\end{cases}\tag{31}$$

Using the exponential reaching laws, we get

$$\begin{cases}\dot{s}_\phi = -\lambda_\phi s_\phi - k_\phi\,\text{sign}\,(s_\phi),\\ \dot{s}_\theta = -\lambda_\theta s_\theta - k_\theta\,\text{sign}\,(s_\theta),\\ \dot{s}_\psi = -\lambda_\psi s_\psi - k_\psi\,\text{sign}\,(s_\psi).\end{cases}\tag{32}$$

From equation (31) and equation (32), the control laws of the attitude subsystem are given as

$$\begin{aligned}U_2 &= I_x\left[-\left(\dot{\theta}\dot{\psi}\frac{I_y - I_z}{I_x} - \dot{\theta}\frac{J_r}{I_x}\Omega_r - \frac{k_4}{I_x}\dot{\phi}^2\right) - d_\phi - \lambda_\phi s_\phi\right.\\ &\quad \left. - k_\phi\,\text{sign}\,(s_\phi) + \ddot{\phi}_d - \alpha_\phi\dot{e}_\phi{}^{(q_\phi/p_\phi)} - \beta_\phi e_\phi{}^{(q_\phi/(2p_\phi - q_\phi))}\right],\\ U_3 &= I_y\left[-\left(\dot{\phi}\dot{\psi}\frac{I_z - I_x}{I_y} + \dot{\phi}\frac{J_r}{I_y}\Omega_r - \frac{k_5}{I_y}\dot{\theta}^2\right) - d_\theta - \lambda_\theta s_\theta\right.\\ &\quad \left. - k_\theta\,\text{sign}\,(s_\theta) + \ddot{\theta}_d - \alpha_\theta\dot{e}_\theta{}^{(q_\theta/p_\theta)} - \beta_\theta e_\theta{}^{(q_\theta/(2p_\theta - q_\theta))}\right],\\ U_4 &= I_z\left[-\left(\dot{\phi}\dot{\theta}\frac{I_x - I_y}{I_z} - \frac{k_6}{I_z}\dot{\psi}^2\right) - d_\psi - \lambda_\psi s_\psi\right.\\ &\quad \left. - k_\psi\,\text{sign}\,(s_\psi) + \ddot{\psi}_d - \alpha_\psi\dot{e}_\psi{}^{(q_\psi/p_\psi)} - \beta_\psi e_\psi{}^{(q_\psi/(2p_\psi - q_\psi))}\right].\end{aligned}\tag{33}$$

Proof. In order to demonstrate the stability of the attitude subsystem, the Lyapunov candidate function of the roll subsystem is given as follows:

$$V_\phi = \frac{1}{2}s_\phi^2.\tag{34}$$

Table 1: Quadrotor parameters.

Parameter	Value	Parameter	Value
g $(\mathrm{m/s}^2)$	9.81	k_2 (N/m/s)	$5.567e\text{-}4$
m (kg)	0.486	k_3 (N/m/s)	$6.354e\text{-}5$
I_x $(\mathrm{kg \cdot m}^2)$	$3.827e\text{-}3$	k_4 (N/m/s)	$5.567e\text{-}4$
I_y $(\mathrm{kg \cdot m}^2)$	$3.827e\text{-}3$	k_5 (N/m/s)	$5.567e\text{-}4$
I_z $(\mathrm{kg \cdot m}^2)$	$7.656e\text{-}3$	k_6 (N/m/s)	$6.354e\text{-}5$
J_r $(\mathrm{kg \cdot m}^2)$	$2.838e\text{-}5$	b $(\mathrm{N \cdot s}^2)$	$2.984e\text{-}3$
k_1 (N/m/s)	$5.567e\text{-}4$	d $(\mathrm{N \cdot m/s}^2)$	$3.232e\text{-}2$

Table 2: The reference trajectories of the position and yaw angle.

Variables	Value	Time (s)
	[0.6, 0.6, 0.6] m	0
	[0.3, 0.6, 0.6] m	10
$[x_d, y_d, z_d]$	[0.3, 0.3, 0.6] m	20
	[0.6, 0.6, 0.6] m	30
	[0.6, 0.6, 0.6] m	40
	[0.6, 0.6, 0.6] m	50
$[\psi_d]$	[0.5] rad	0
$[\psi_d]$	[0.0] rad	50

The time derivative of V_ϕ is

$$
\begin{aligned}
\dot{V}_\phi &= s_\phi \dot{s}_\phi = s_\phi \left(\ddot{\phi} - \ddot{\phi}_d + \alpha_\phi \dot{e}_\phi^{(q_\phi/p_\phi)} + \beta_\phi e_\phi^{(q_\phi/(2p_\phi - q_\phi))} \right) \\
&= s_\phi \left(\dot{\theta}\dot{\psi} \frac{I_y - I_z}{I_x} - \dot{\theta}\frac{J_r}{I_x}\Omega_r - \frac{k_4}{I_x}\dot{\phi}^2 + \frac{1}{I_x}U_2 \right. \\
&\quad \left. + d_\phi - \ddot{\phi}_d + \alpha_\phi \dot{e}_\phi^{(q_\phi/p_\phi)} + \beta_\phi e_\phi^{(q_\phi/(2p_\phi - q_\phi))} \right) \\
&= s_\phi \left(\dot{\theta}\dot{\psi}\frac{I_y - I_z}{I_x} - \dot{\theta}\frac{J_r}{I_x}\Omega_r - \frac{k_4}{I_x}\dot{\phi}^2 \right. \\
&\quad + \left[-\left(\dot{\theta}\dot{\psi}\frac{I_y - I_z}{I_x} - \dot{\theta}\frac{J_r}{I_x}\Omega_r - \frac{k_4}{I_x}\dot{\phi}^2 \right) - d_\phi - \lambda_\phi s_\phi \right. \\
&\quad \left. - k_\phi \operatorname{sign}(s_\phi) + \ddot{\phi}_d - \alpha_\phi \dot{e}_\phi^{(q_\phi/p_\phi)} - \beta_\phi e_\phi^{(q_\phi/(2p_\phi - q_\phi))} \right] \\
&\quad \left. + d_\phi - \ddot{\phi}_d + \alpha_\phi \dot{e}_\phi^{(q_\phi/p_\phi)} + \beta_\phi e_\phi^{(q_\phi/(2p_\phi - q_\phi))} \right) \\
&= s_\phi \left(-\lambda_\phi s_\phi - k_\phi \operatorname{sign}(s_\phi) \right) = -\lambda_\phi s_\phi^2 - k_\phi |s_\phi| \le 0.
\end{aligned}
\tag{35}
$$

Table 3: Control system parameters.

Parameter	Value	Parameter	Value
c_{x1}	1.68	c_{x2}	2.34
c_{y1}	1	c_{y2}	2.25
c_{z1}	6.40	c_{z2}	20
α_i	59.78	β_i	974.57
p_i	54	q_i	52
λ_i	2	k_i	10.66

4. Simulation Results

To validate the performances of the proposed controllers, numerical simulations will be presented in this section. The parameters of the quadrotor used in the simulation are selected in Table 1. The initial attitude and position of the quadrotor are chosen as [0, 0, 0] rad and [0, 0, 0] m. The desired trajectory of the yaw angle and the position is given in Table 2. The external disturbances used in the simulation are given as follows: $d_x = 1$ N at $t = 5$ s; $d_\phi = 1$ rad/s^2 at $t = 10$ s; $d_y = 1$ N at $t = 15$ s; $d_\theta = 1$ rad/s^2 at $t = 20$ s; $d_z = 1$ N at $t = 25$ s; and $d_\psi = 1$ rad/s^2 at $t = 30$ s. Besides, the parameters of the proposed controller are listed in Table 3.

Remark 1. In order to achieve a smooth and quick tracking performance, the design parameters of the proposed AB-RITSMC, B-SMC, and SMC techniques have been tuned by using a toolbox optimization method in MATLAB/Simulink (see, e.g., [25]).

Furthermore, In order to highlight the superiority of the proposed control laws, comparisons with the backstepping sliding mode control and the first-order sliding mode control technique are done.

The simulation results are shown in Figures 3–8. The desired and actual tracking positions x, y, and z are shown in Figure 3, where the proposed control strategy that drives the quadrotor to track the desired flight trajectory more rapidly and more accurately can be seen, then the classic sliding mode control method and the backstepping sliding mode controller. The constant disturbances are added in the position subsystem at $t = 5$. It appears that the proposed control approach has managed to effectively hold the quadrotor's position in finite time contrary to the SMC and B-SMC; the same behaviour can be observed at $t = 15$ for the y position and at $t = 25$ for the z position of the quadrotor system. Furthermore, trajectory attitudes ϕ, θ, and ψ are shown in Figure 4. It can be seen that the quadrotor attitude tracks the desired angles in short finite time. The attitude sliding variables (s_ϕ, s_θ, and s_ψ) are shown in Figure 6; the convergence to zero in finite time of the sliding surfaces can be observed. The trajectory-tracking errors of the position are depicted in Figure 5. The estimate force acting in direction z is shown in Figure 8. In order to demonstrate the superiority of the proposed control strategy, the quadrotor trajectory path performance in 3-D space is shown in Figure 7. Clearly, it can be seen that the proposed control strategy can accurately track the square trajectory in the presence of external disturbances. The proposed control approach obtains better performance compared to the conventional SMC and B-SMC methods in terms of disturbance rejection and trajectory tracking.
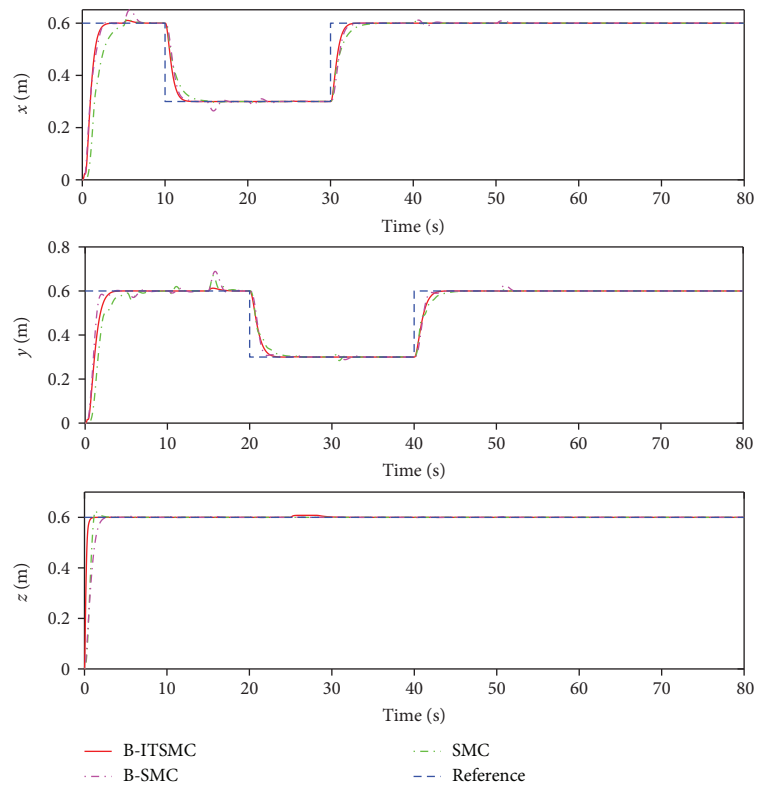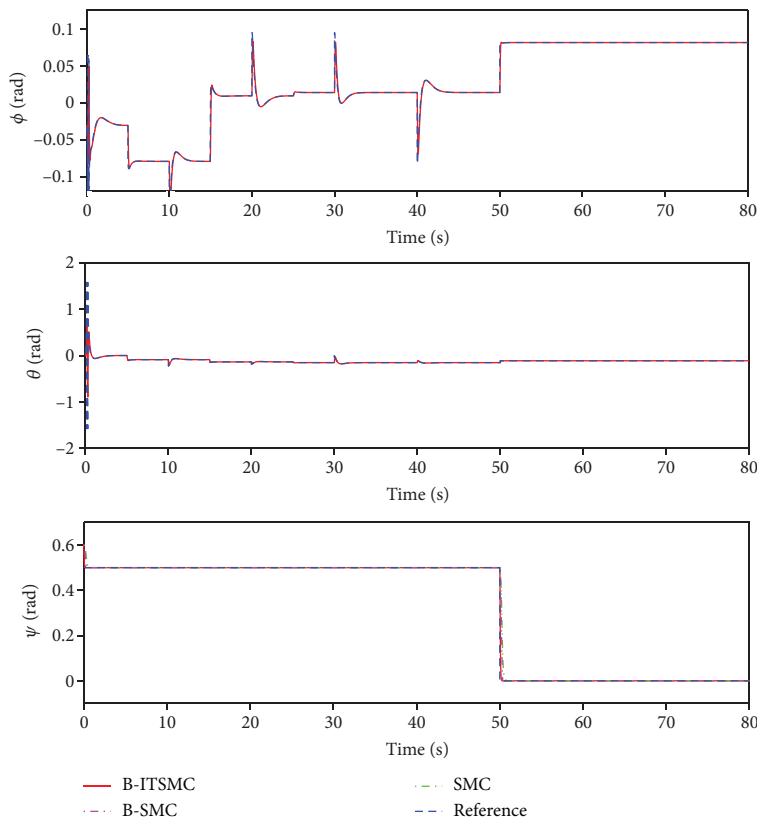
Figure 3: Response of quadrotor position.

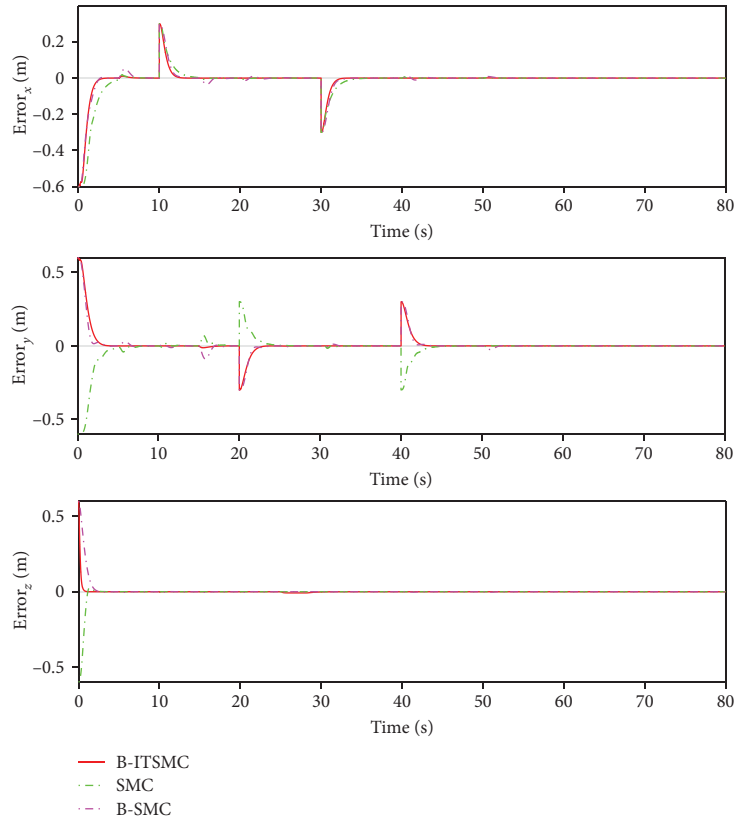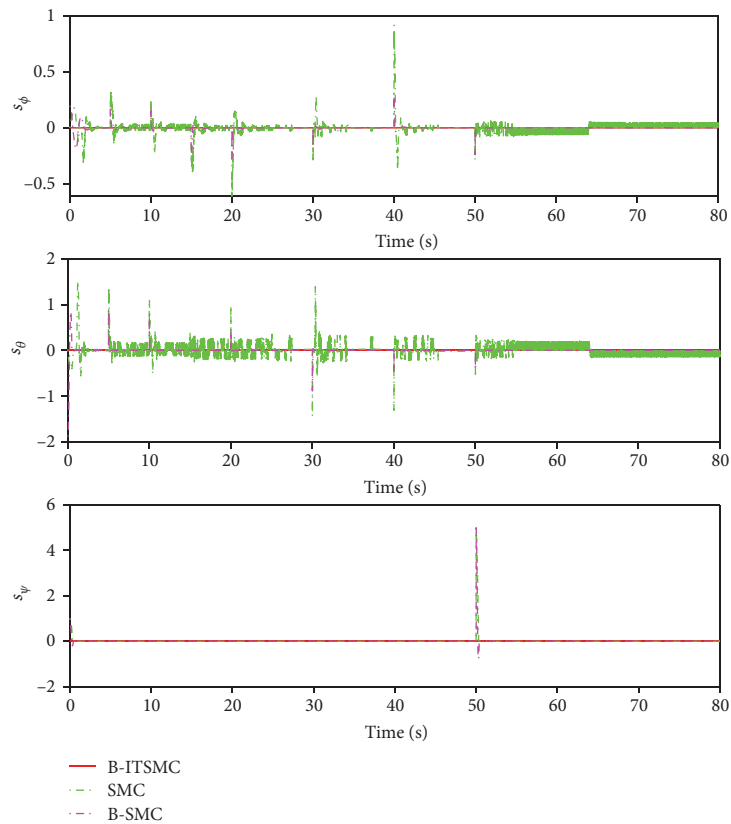Figure 4: Response of quadrotor attitude.

Figure 5: Position errors.

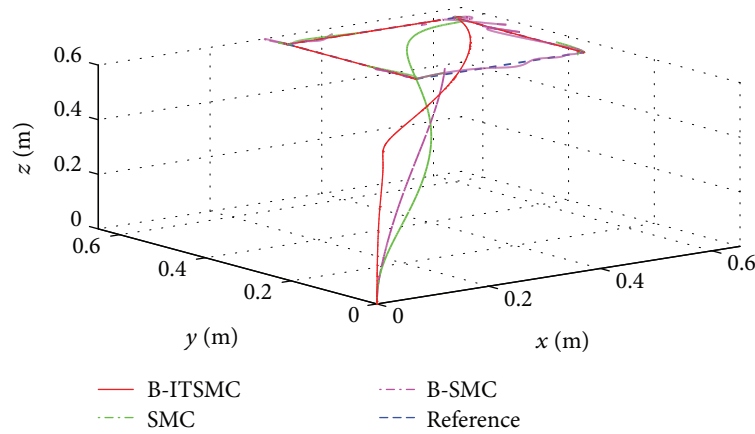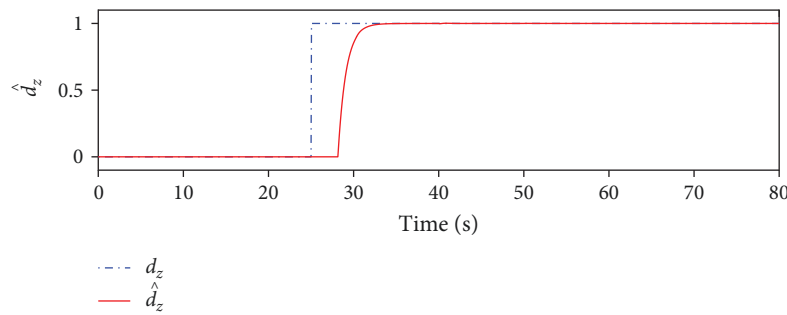Figure 6: Tracking errors (s_ϕ, s_θ, and s_ψ), B-ITSMC.

FIGURE 7: Flight trajectory tracking, B-RITSMC.

FIGURE 8: The estimate of the d_z parameter.

5. Conclusions

In this study, we have examined the problem of the flight trajectory-tracking phenomenon of the quadrotor with disturbances. The proposed control scheme is made up of three different parts: control of an altitude, a horizontal position, and an attitude subsystem. Firstly, the altitude subsystem is addressed based on adaptive backstepping. Also, the backstepping technique is designed to control the positions x and y of a quadrotor. The control objectives of this loop are (i) obtaining the desired roll and pitch angles, (ii) tracking the desired flight trajectory in finite time, and (iii) generating the total thrust. Secondly, a new robust integral terminal sliding mode controller has been constructed to stabilize the attitude subsystem. The objectives of the RITSMC control scheme are

(i) tracking the desired angles

(ii) stabilizing the quadrotor attitude

(iii) generating the rolling, pitching, and yawing torques

In addition, the proposed controller achieves the fast and accurate tracking of the quadrotor trajectory. Finally, simulation results have demonstrated that the proposed controller is able to improve control performance of the quadrotor UAV system in the presence of external disturbances. The proposed control strategy has shown the effectiveness and superiority of the classical sliding mode control strategy and backstepping sliding mode control technique.

The following points will be addressed in the future work:

(i) Taking into account the motor dynamics of the quadrotor

(ii) Inclusion of a fault detection in the actuators and sensors

(iii) Use of adaptive RITSMC approach in the improvement of the quadrotor control system

Data Availability

No new data were created during the study.

Conflicts of Interest

The authors declare that they have no conflicts of interest.

References

[1] M. Hassanalian and A. Abdelkefi, "Classifications, applications, and design challenges of drones: a review," *Progress in Aerospace Science*, vol. 91, pp. 99–131, 2017.

[2] A. Mairaj, A. I. Baba, and A. Y. Javaid, "Application specific drone simulators: recent advances and challenges," *Simulation Modelling Practice and Theory*, vol. 94, pp. 100–117, 2019.

[3] H. Mo and G. Farid, "Nonlinear and adaptive intelligent control techniques for quadrotor UAV - a survey," *Asian Journal of Control*, vol. 21, no. 2, pp. 989–1008, 2018.

[4] N. Wang, Q. Deng, G. Xie, and X. Pan, "Hybrid finite-time trajectory tracking control of a quadrotor," *ISA Transactions*, vol. 90, pp. 278–286, 2019.

[5] Z. Li, X. Ma, and Y. Li, "Robust tracking control strategy for a quadrotor using RPD-SMC and RISE," *Neurocomputing*, vol. 331, pp. 312–322, 2019.

[6] A. A. Najm and I. K. Ibraheem, "Nonlinear PID controller design for a 6-DOF UAV quadrotor system," *Engineering Science and Technology, an International Journal*, 2019.

[7] M. Vahdanipour and M. Khodabandeh, "Adaptive fractional order sliding mode control for a quadrotor with a varying load," *Aerospace Science and Technology*, vol. 86, pp. 737–747, 2019.

[8] F. Chen, R. Jiang, K. Zhang, B. Jiang, and G. Tao, "Robust backstepping sliding-mode control and observer-based fault estimation for a quadrotor UAV," *IEEE Transactions on Industrial Electronics*, vol. 63, no. 8, pp. 5044–5056, 2016.

[9] E. H. Zheng, J. J. Xiong, and J. L. Luo, "Second order sliding mode control for a quadrotor UAV," *ISA Transactions*, vol. 53, no. 4, pp. 1350–1356, 2014.

[10] J. J. Xiong and G. B. Zhang, "Global fast dynamic terminal sliding mode control for a quadrotor UAV," *ISA Transactions*, vol. 66, pp. 233–240, 2017.

[11] S. Mobayen and F. Tchier, "Nonsingular fast terminal sliding-mode stabilizer for a class of uncertain nonlinear systems based on disturbance observer," *Scientia Iranica*, vol. 24, no. 3, pp. 1410–1418, 2017.

[12] O. Mofid and S. Mobayen, "Adaptive sliding mode control for finite-time stability of quad-rotor UAVs with parametric uncertainties," *ISA Transactions*, vol. 72, pp. 1–14, 2018.

[13] Z. Jia, J. Yu, Y. Mei, Y. Chen, Y. Shen, and X. Ai, "Integral backstepping sliding mode control for quadrotor helicopter under external uncertain disturbances," *Aerospace Science and Technology*, vol. 68, pp. 299–307, 2017.

[14] C. C. Hua, K. Wang, J. N. Chen, and X. You, "Tracking differentiator and extended state observer-based nonsingular fast terminal sliding mode attitude control for a quadrotor," *Nonlinear Dynamics*, vol. 94, no. 1, pp. 343–354, 2018.

[15] S. Amirkhani, S. Mobayen, N. Iliaee, O. Boubaker, and S. H. Hosseinnia, "Fast terminal sliding mode tracking control of nonlinear uncertain mass–spring system with experimental verifications," *International Journal of Advanced Robotic Systems*, vol. 16, no. 1, 2019.

[16] F. Muñoz, E. S. Espinoza, I. González-Hernández, S. Salazar, and R. Lozano, "Robust trajectory tracking for unmanned aircraft systems using a nonsingular terminal modified super-twisting sliding mode controller," *Journal of Intelligent & Robotic Systems*, vol. 93, no. 1-2, pp. 55–72, 2019.

[17] D. Ashtiani Haghighi and S. Mobayen, "Design of an adaptive super-twisting decoupled terminal sliding mode control scheme for a class of fourth-order systems," *ISA Transactions*, vol. 75, pp. 216–225, 2018.

[18] J. J. Xiong and E. H. Zheng, "Position and attitude tracking control for a quadrotor UAV," *ISA Transactions*, vol. 53, no. 3, pp. 725–731, 2014.

[19] S. Bouabdallah and R. Siegwart, "Backstepping and sliding-mode techniques applied to an indoor micro quadrotor," in *Proceedings of the 2005 IEEE International Conference on Robotics and Automation*, pp. 2247–2252, Barcelona, Spain, April 2005.

[20] H. Liu, J. Xi, and Y. Zhong, "Robust attitude stabilization for nonlinear quadrotor systems with uncertainties and delays," *IEEE Transactions on Industrial Electronics*, vol. 64, no. 7, pp. 5585–5594, 2017.

[21] M. Labbadi, M. Cherkaoui, Y. El Houm, and M. Guisser, "A comparative analysis of control strategies for stabilizing a quadrotor," in *Information Systems and Technologies to Support Learning. EMENA-ISTL 2018. Smart Innovation, Systems and Technologies*, Á. Rocha and M. Serrhini, Eds., vol. 111 of Smart Innovation, Systems and Technologies, Springer, Cham, 2019.

[22] M. Labbadi, M. Cherkaoui, Y. El Houm, and M. Guisser, "Modeling and robust integral sliding mode control for a quadrotor unmanned aerial vehicle," in *2018 6th International Renewable and Sustainable Energy Conference (IRSEC)*, pp. 1–6, Rabat, Morocco, December 2018.

[23] R. Zhang, L. Dong, and C. Sun, "Adaptive nonsingular terminal sliding mode control design for near space hypersonic vehicles," *IEEE/CAA Journal of Automatica Sinica*, vol. 1, no. 2, pp. 155–161, 2014.

[24] A. Riani, T. Madani, A. Benallegue, and K. Djouani, "Adaptive integral terminal sliding mode control for upper-limb rehabilitation exoskeleton," *Control Engineering Practice*, vol. 75, pp. 108–117, 2018.

[25] F. P. Freire, N. A. Martins, and F. Splendor, "A simple optimization method for tuning the gains of PID controllers for the autopilot of Cessna 182 aircraft using model-in-the-loop platform," *Journal of Control, Automation and Electrical Systems*, vol. 29, no. 4, pp. 441–450, 2018.